Radial projection statistics: a different angle on tilings

Dissertation zur Erlangung des akademischen Grades eines
Doktors der Mathematik (Dr. math.)

vorgelegt von

Tobias Jakobi
(aus Lübbecke)

Fakultät für Mathematik
Universität Bielefeld

29. März 2017

1. Berichterstatter: Prof. Dr. Michael Baake
2. Berichterstatter: Prof. Dr. Friedrich Götze

Gedruckt auf alterungsbeständigem Papier °°ISO 9706.

Contents

Introduction

When looking at physical structures, the natural question about the internal order (of molecules, atoms, molecule clusters) arises. How to quantify order in a good way is still largely unknown.

Consider a mathematical model such that the positions of the components inside the structure are represented as a locally finite point set in $\mathbb{R}^d$. We are primarily interested in the cases $d = 2$ or $d = 3$. Let us denote the elements of the point set as *vertices*. One could now describe the order by looking at each vertex and measure the Euclidean distance to all other vertices in the set. This would yield a very complicated object, and comparing two such objects does not appear to be feasible in general. Also, this approach would be somewhat naive and does not correspond to any measurement one can easily do with a physical apparatus. However, there exist methods like *diffraction* (see [28, 19] and [5, Ch. 9] for an introduction) that give a lot of information about the input set. Some properties which can be analysed by diffraction are translational repetitions and symmetries of the set. Since the advent of material analysis, diffraction has become somewhat like a standard tool in physics to detect order in a certain material. Also the mathematical theory behind it was advanced tremendously in the last years, furthermore getting a large boost in 2011, when Dan Shechtman was awarded the Nobel Prize in Chemistry for his discovery of quasicrystals.

Still, diffraction has its limits, as there are different point sets which produce the same diffraction image. Hence, the inverse problem, the deduction of the input from the pattern, is not always possible, or at least not without additional information.

Here, we present another approach, which shares some similarities with the diffraction method, but avoids Fourier-based methods and instead works in the direct space where the point set lives.

We want to point out, that compared to the usual dissertation in mathematics, this thesis puts a strong emphasis on numerical computations. For this reason, many concepts are explained in an algorithmic fashion, always with the later software implementation in mind. Whenever possible, we try to establish a rigorous basis to rule out errors, provide consistency checks and to show that the algorithms are indeed working how they are supposed to. Still, many results only admit a heuristic explanation at present.

Consequently, we go for a more informal and discursive representation of the results. All the results should merely be understood as the beginning of a further development, where even the core definitions, i.e. what we denote as radial projection statistics, are still subject to changes. It might still take more time and a better understanding of the general setting to refine and finalise the definitions. This is one reason why we decided to give a broad overview, instead of going into depth for one particular problem.

Outline of the thesis

In Chapter 1 we describe the radial projection method in general together with the two extremal cases, being the integer lattice $\mathbb{Z}^2$ and vertices distributed according to a Poisson process. We also briefly discuss a potential generalisation to higher dimensions. Then, in Chapter 2, the aperiodic tilings which were used as input for the method are presented, together with the numerical approximation of the corresponding limit distributions. Next, in Chapter 3, we focus on the difficulties of constructing large patches of a given tiling, so it can serve as source for a good approximation of the radial projection. Here the problems encountered differ depending on whether the tiling can be produced from a model set description, or by an inflation procedure. In Chapter 4, we proceed by explaining how the condition to be a visible vertex for a given tiling can be sometimes *refined* into much simpler statements about the algebraic properties of that vertex. The Chapter 5 explores the effects of randomisation on a given tiling, where we are interested in the dependency between core features of the limit distribution and the parameters used for the randomisation. Moreover, in Chapter 6 we take a look at the limit distribution when considering second-order instead of first-order spacings. Finally, in Chapter 7, we briefly touch upon the property of arithmetic visibility in some interesting number fields. This is sort of an extension to what we discussed in Chapter 4, but it is not that closely tied to the radial projection as the other chapters are.

Acknowledgements

First and foremost, I thank my supervisors Prof. Dr. Michael Baake and Prof. Dr. Friedrich Götze for recommending the topic of the thesis to me and providing both guidance and encouragement. Their office door was always open whenever I got stuck with a problem or did not know how or in which direction to proceed. Special thanks goes to all former and present members of our working group. By name and in alphabetic order these are Enrico Paolo Bugarin, Dirk Frettlöh, Franz Gähler, Christian Huck, Chrizaldy Neil Mañibo, Markus Moll, Johan Nilsson, Eden Delight Provido, Dan Rust, Timo Spindeler, Venta Terauds and Peter Zeiner.

I also want to thank Uwe Grimm for his expertise on writing `PostScript` and `Mathematica` code, Holger Kösters for all matters involving probability theory, and Johannes Roth for helpful discussions about model sets with high-dimensional internal space.

In addition, I thank the German Research Foundation (DFG) for the financial support within the CRC 701.

Finally, I want to express my gratitude to both my parents Brigitte and Wolfgang and my sister Lisa-Kristin for their emotional support and for always gently pushing me forward.

CHAPTER 1

The radial projection method

As we have mentioned in the introduction, we want to construct a method to measure order in a point set, but without changing the domain of the input. We call this the *radial projection method* (RPM), since its key ingredient is a suitable reduction of the information coming from the point set, here implemented by mapping a vertex to its angular component relative to some reference frame.

1.1. Introducing the RPM

We restrict ourselves to dimension $d = 2$. A possible generalisation to higher dimensions will be discussed in Section 1.4 at the end of this chapter.

Procedure 1.1

We start with a locally finite point set $S \subseteq \mathbb{R}^2$ and begin by selecting a reference point $x_0 \in \mathbb{R}^2$. Elements from the set S will be denoted as *vertices*, since most of the time S is produced from a tiling of the plane, where we just collect all vertices of the tiles.

For simplicity we also impose two additional conditions onto x_0.

(1) The reference point is an element of the set, i.e. $x_0 \in S$.
(2) The set S is highly symmetric with respect to x_0. See e.g. Fig. 2.5 with the red vertex as x_0 on page 16.

Now, S is thinned out by removing invisible vertices. These are the vertices that are not observable from the reference point x_0, meaning that a straight line from x_0 to the point, p say, is already blocked by some other point p_0 of the set,

$$\exists\, p_0 \in S \quad \exists\, t \in (0,1) \ : \ p_0 = x_0 + t \cdot (p - x_0)\ . \tag{1.1}$$

Denote the new set of *visible vertices* by V.

$$V \ := \ \{x \in S \ : \ x \text{ is visible from } x_0\} \ = \ S \setminus \{x \in S \ : \ x \text{ satisfies Eq. (1.1)}\}$$

Now, fix a parameter $R > 0$ and consider the closed disc $D_R(x_0)$ of radius R around x_0,

$$D_R(x_0) \ = \ D_R \ = \ \{x \in \mathbb{R}^2 \ : \ \|x - x_0\| \leqslant R\}\ .$$

By an appropriate translation in $\mathbb{R}^2$, we can always map x_0 to the origin. Therefore, without loss of generality, we may assume $x_0 = (0,0)$. Let $V_R := V \cap D_R$. Since S is locally finite, then so is V and we have

$$n \ := \ |V_R| < \infty\ .$$

We proceed by projecting each $x \in V_R$ from the reference point radially onto the boundary of the disc. If we write the vertex in polar coordinates

$$x \;=\; r \cdot \exp(i\varphi) \quad \text{with} \quad 0 \leqslant r \leqslant R \,,$$

this amounts to mapping x to the corresponding angle $\varphi \in [0, 2\pi)$. This produces a set of angles which we then sort in ascending order,

$$\Phi_R \;:=\; \{\varphi_1, \ldots, \varphi_n\} \;.$$

In fact, we have $\varphi_i < \varphi_{i+1}$ for all i since the reduction to visible vertices ensures that the projected vertices are distinct. The mapping from visible vertices to their angles is therefore one-to-one.
The mean distance between consecutive elements from Φ_R is given by

$$d_{\mathsf{mean}} \;=\; \frac{1}{n-1} \sum_{i=1}^{n-1} (\varphi_{i+1} - \varphi_i) \;=\; \frac{\varphi_n - \varphi_1}{n-1} \;,$$

where we can assume $\varphi_1 \approx 0$ and $\varphi_n \approx 2\pi$. Hence, by applying a rescaling with the factor $c_R := \frac{n-1}{2\pi} \approx d_{\mathsf{mean}}^{-1}$, the mean distance becomes one,

$$\overline{\Phi}_R \;:=\; \{\overline{\varphi}_1, \ldots, \overline{\varphi}_n\} \quad \text{with} \quad \overline{\varphi}_i := c_R \cdot \varphi_i \;. \tag{1.2}$$

Our objects of interest are the distances after rescaling. For this, let

$$d_i \;:=\; \overline{\varphi}_{i+1} - \overline{\varphi}_i$$

and denote the d_i as *radial spacings* or simply *spacings* for the set S at x_0 with radius R. We want to know how the d_i behave statistically. To examine this, we define the discrete probability measure on $\mathbb{R}_+$

$$\nu_R \;:=\; \frac{1}{n-1} \sum_{i=1}^{n-1} \delta_{d_i}$$

encoding the distribution of spacings for a given R. Here, δ_x is the *Dirac measure* at the position x.
In the physics literature, this object is often denoted as the discrete spacing distribution. The choice to consider neighbouring angles is motivated by the concept of *two-point correlations* which is prominent when looking at interacting particle systems. Some investigation into the distribution of second-order spacings, where we ask how much d_i depends on d_{i+1}, follows in Chapter 6.
We are now interested in whether there exists a limit measure ν on the positive real line $\mathbb{R}_+$, i.e.

$$\lim_{R \to \infty} \nu_R \;=\; \nu \;, \tag{1.3}$$

in the sense of weak convergence of measures.

Definition 1.2
If ν in Eq. 1.3 exists, we call it the *radial projection measure* of the point set S, relative to $x_0 \in S$.

Remark 1.3
Under the assumption that ν exists, the rescaling that we applied ensures that the input set S is mapped to a probability measure, i.e. $\nu(\mathbb{R}_+) = 1$. Obviously, this is also true for all the discrete measures ν_R.
We hope that the radial projection measure encodes enough information about the order of the input S, so that we can compare measures for different point sets and make comparative statements about the underlying sets. In this sense, the procedure is meant to be a real-space alternative or addition to the diffraction of points sets. There, we also have to consider the "inverse problem", i.e. determining the point set of a a given diffraction pattern.

Remark 1.4
The fundamental reduction of information in Procedure 1.1 is done by the map

$$x \; = \; r \cdot \exp(i\varphi) \quad \longmapsto \quad \varphi \; .$$

If we write $x = (a, b) \in \mathbb{R}^2$, then the corresponding angle can also be computed via

$$\varphi \; = \; \arctan(b/a) \; ,$$

assuming that $a \neq 0$. Hence, the reduction is actually a two-stage process, consisting of taking the slope of the x and then applying a non-linear transformation, here the arctan, to it.
In Chapter 6 we are going to see some effects of this non-linearity. In particular, we like to point out, that everything in following chapters could also be done using the slope, instead of the angle of the vertex.

Remark 1.5
Deriving an analytic description for ν given an arbitrary set S is a daunting task and, even with nice sets, presently appears to be an almost hopeless endeavour. Our primary focus therefore lies in creating good numerical approximations of such limit distributions in the form of histograms, see also Procedure 2.9 in the next chapter, with a fine resolution.
The rescaling step of the angles described in Procedure 1.1 therefore also enables us to easily compare the ν_R for different radii R. For the Figs. 1.1, 1.2 and all the subsequent graphs in Chapter 2, this means that we measure in units of the mean distance on the x-axis.

Before attempting to apply this method to some interesting point sets, we begin with some *reference point sets* as limiting cases of a potential classification.

1.2. Total order – the integer lattice $\mathbb{Z}^2$

The point set $\mathbb{Z}^2$ is the most natural candidate to start investigating the radial projection procedure. The choice of reference point can be done in two ways, either picking a $x_0 \in \mathbb{Z}^2$ where the choice does not matter because of translation symmetry, or picking a $x_0 \notin \mathbb{Z}^2$. In the latter case, we can further differentiate between a non-generic x_0 and a generic one, i.e. a point where all vertices are visible from. The generic case was studied in [39] in a slightly different context. Here, we concentrate on $x_0 := (0, 0)$. Let $x \in \mathbb{Z}^2$ be another vertex, and consider the ray $\vec{r}$ connecting x_0 with x. Then $\vec{r}$ is spanned by x', i.e.

$$\vec{r} \cap \mathbb{Z}^2 \;=\; \{\lambda \cdot x' \;:\; \lambda \in \mathbb{N}_0\}\;,$$

where x' is the primitive, in the lattice vector sense, version of x. This simple geometric argument then reveals that visibility of a vertex $x = (a, b)$ is characterised by the property that its Cartesian coordinates are coprime (see also [9, 44]), i.e. we have $|\gcd(a, b)| = 1$. We denote this property as a *local* visibility test, since the determination of visibility only relies on local information, which are just the coordinates of the vertices here.

Remark 1.6
It has long been known [16] that the visible lattice points are intimately related to the *Farey fractions*

$$\mathcal{F}_Q \;=\; \{a/q : 1 \leqslant a \leqslant q \leqslant Q,\ \gcd(a, q) = 1\}\,,$$

here of order Q. Sorted in ascending order, $\mathcal{F}_Q$ is also called a Farey series, even though it technically is a finite sequence with $m := |\mathcal{F}_Q|$ elements,

$$\mathcal{F}_Q \;=\; \{f_1, \ldots, f_m\} \subset (0, 1], \quad f_1 = Q^{-1},\ f_m = 1\;.$$

Such sequences are interesting since certain uniformity conditions are tied to one of the most important problems in mathematics. The growth statement

$$\forall\, \epsilon > 0\;:\; \sum_{i=1}^{m} \left| f_i - \frac{i}{m} \right| = \mathcal{O}(Q^{1/2+\epsilon})$$

is equivalent to the Riemann hypothesis [37]. Another property worth noting is the closed description of succesive fractions, which admits enumeration formulas that make an analytic approach possible.

Remark 1.7 (Thm. 28, 30 in [27])
Let $f_0 = a_0/q_0$ and $f_1 = a_1/q_1$ be two fractions from $\mathcal{F}_Q$, then f_0 and f_1 are successive elements iff

$$a_1 q_0 - a_0 q_1 = 1 \quad \wedge \quad q_0 + q_1 > Q$$

holds.

Let us state an important result on the radial spacing distribution of $\mathbb{Z}^2$.

Theorem 1.8 (Cor. 0.4 in [10])
Let $S := \mathbb{Z}^2$ be our input set with reference point $x_0 := (0, 0)$. Then, the limit distribution ν from Eq. (1.3) exists and is an absolutely continuous measure

with the following density function,

$$g(t) = \begin{cases} 0, & 0 < t < \frac{3}{\pi^2}, \\ \frac{6}{\pi^2 t^2} \cdot \log \frac{\pi^2 t}{3}, & \frac{3}{\pi^2} < t < \frac{12}{\pi^2}, \\ \frac{12}{\pi^2 t^2} \cdot \log \left(2 \cdot \left(1 + \sqrt{1 - \frac{12}{\pi^2 t}} \right)^{-1} \right), & t > \frac{12}{\pi^2} \; . \end{cases} \tag{1.4}$$

In particular, the density is a continuous and piecewise smooth function.

We are going to see that the pronounced gap , here in the interval $[0, 3/\pi^2]$, is a feature that also appears in other examples.

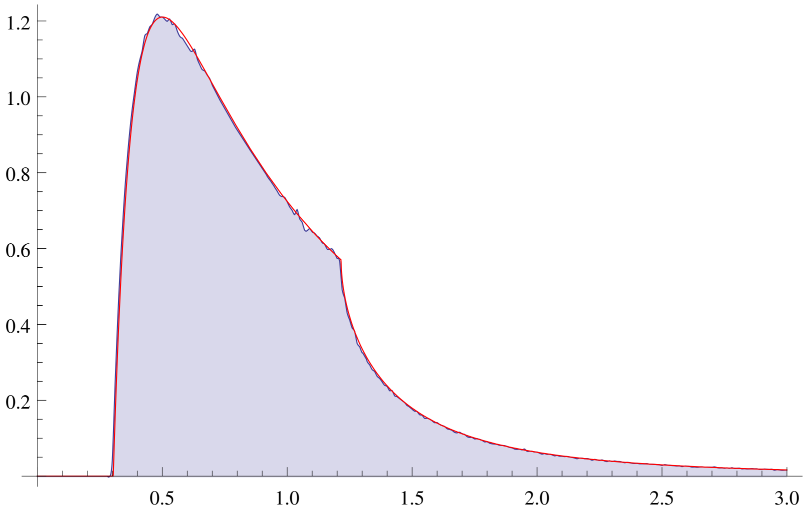

Figure 1.1. Empirical spacing distribution of a $\mathbb{Z}^2$ patch together with the exact density function in red.

Fig. 1.1 illustrates the function $g(t)$ and compares it with the empirical distribution for a patch of size $R = 2900$. This circular patch then provides $n \approx 1.98 \cdot 10^6$ angles for the numerical evaluation.

Remark 1.9
The result from Theorem 1.8 was first proved 2000 in [10] and also holds in a more general setting. If we replace the disc D_R in Procedure 1.1 with a star-shaped region satisfying some extra regularity conditions (continuity and piecewise $\mathcal{C}^1$ for the boundary D of the region) the limit distribution still exists and also a repartition function $F(t) := \nu([t, \infty))$ can be written down explicitly. Let D be parametrised by angle, i.e. we write

$$D \;=\; \{(r(\vartheta)\cos(\vartheta), r(\vartheta)\sin(\vartheta) \;:\; \vartheta \in [0, 2\pi)\} \; .$$

Then, we can see from [10, Thm. 0.1] that the function $F(t)$ tends to be a lot more complex than $g(t)$ from above because of the additional angular dependence. In fact, this shows that the shape of the expanding region is significant here,

and pertubations of it are likely to show up in the limit distribution.
Our hope is that the restriction to a disc D_R increases the odds of also finding analytic expressions for other ν.

A different approach for the proof of Theorem 1.8 can be found in [4], based on ergodic theory on $\mathrm{SO}(2,\mathbb{R})/\,\mathrm{SL}(2,\mathbb{Z})$. In particular, the two domain changes in Eq. (1.4) then have a nice geometric interpretation. The value of $g(t)$ here is computed as the area of the intersection of a fixed and a moving region in $\mathbb{R}^2$; also compare [2].

1.3. Disorder – Poisson distributed points

On the opposite end of the spectrum, we encounter the totally disordered case. In physics terminology, this is the realm of the ideal gas. The vertices in $\mathbb{R}^2$ are distributed according to a homogeneous spatial Poisson point process , a model also known as *complete spatial randomness* (CSR), emphasising that points are randomly located in ambient space.

Definition 1.10
Let μ denote the standard Borel–Lebesgue measure on $\mathbb{R}^n$, S the vertex set belonging to our ideal gas and $\lambda > 0$ a fixed parameter. For each $A \subseteq \mathbb{R}^n$, define $\mathrm{N}(A)$ to be the number of vertices from S in A, i.e.

$$\mathrm{N}(A) \;:=\; |A \cap S| \ .$$

Then, the set S is characterised by the following properties.

- (a) For each bounded, measurable $A \subseteq \mathbb{R}^n$, the quantity $\mathrm{N}(A)$ is a Poisson random variable, which is distributed according to $\mathsf{Pois}(\lambda \cdot \mu(A))$.
- (b) For each finite selection of disjoint $A_1, \ldots, A_k \subseteq \mathbb{R}^n$, the quantities $\mathrm{N}(A_1), \ldots, \mathrm{N}(A_k)$ are independent random variables.

We denote any realisation of such a configuration as S_{Pois} with intensity λ.

Lemma 1.11
Let S_{Pois} be an ideal gas configuration in $\mathbb{R}^2$ and V the corresponding set of visible vertices. Then, for any reference point $x_0 \in \mathbb{R}^2$, we have

$$S_{\mathsf{Pois}} \;=\; V$$

almost surely with respect to the law of the Poisson process.

Proof. The Poisson property (a) implies a condition for *overlapping* vertices, i.e. we have

$$\lim_{\mu(A)\to 0} \frac{\mathbb{P}(\mathrm{N}(A) \geqslant 1)}{\mathbb{P}(\mathrm{N}(A) = 1)} = 1 \ . \tag{1.5}$$

Consider a sequence $(A_i)_i$ with $\lim_{i\to\infty} \mu(A_i) = 0$. Then, by using that $\mathrm{N}(A_i)$ are all Poisson random variables, we see that

$$\mathbb{P}(\mathrm{N}(A_i) \geqslant 1) \;=\; \sum_{k\geqslant 0} \frac{\ell^k \exp(-\ell)}{k!} \quad \text{and} \quad \mathbb{P}(\mathrm{N}(A_i) = 1) \;=\; \ell \cdot \exp(-\ell) \;,$$

where $\ell := \lambda \cdot \mu(A_i)$. Simplifying the fraction in Eq. (1.5) and taking the limit by applying l'Hôpital's rule yields the assertion. The probability to find more than one vertex in a volume A therefore vanishes when $\mu(A)$ goes to zero. One can see this by the following argument.

Again, we can assume wlog that x_0 is the origin. Now, fix a radius $R > 0$, consider $S_R := S_{\mathsf{Pois}} \cap D_R(x_0)$ and project the vertices from S_R onto the boundary $\partial D_R(x_0)$. The overlapping property ensures that almost surely no overlaps occur even after the projection. Define for $\varphi_1, \varphi_2 \in [0, 2\pi)$ with $\varphi_1 < \varphi_2$ the half-open sector

$$S_{\varphi_1,\varphi_2} \;:=\; \{r \cdot \exp(i\theta) \;:\; 0 < r \leqslant R,\; \varphi_1 \leqslant \theta < \varphi_2\} \;\subset\; S_R$$

between the angles φ_1 and φ_2. Note that we always remove $x_0 = 0_{\mathbb{R}^2}$ from the sector, since the reference point never is a visible vertex. Let $\varphi \in [0, 2\pi)$ be fixed, set $\varphi_1 := \varphi$, $\varphi_2 := \varphi + \epsilon$ and consider the limit $\epsilon \to 0$. Since $\mu(S_{\varphi_1,\varphi_2}) \to 0$, the property in Eq. (1.5) implies that there is at most one projected vertex at the location φ on the boundary.

Hence, for each $R > 0$ the subset of visible vertices is already given by S_R. By taking the limit $R \to \infty$, the property extends to our initial set S_{Pois}, in the almost surely sense. ■

Lemma 1.12

Let S_{Pois} be an ideal gas in $\mathbb{R}^2$, $R > 0$ a fixed parameter and

$$\overline{\Phi}_R \;:=\; \{\overline{\varphi}_1, \ldots, \overline{\varphi}_n\}$$

the ordered set of rescaled angles as given in Eq. (1.2) from Procedure 1.1. Then, the set which one obtains by taking the limit $R \to \infty$ is another ideal gas in $\mathbb{R}_+$ with parameter $\lambda = 1$.

Proof. We reuse the sector notation S_{φ_1,φ_2} from the previous proof. Choose a subinterval $A := [a, b)$ of $[0, 2\pi)$, let $L := |b - a|$ and study the amount $\mathrm{N}(A)$ of points projected into the subinterval. The number of vertices in the sector $S_{a,b}$ equals $\mathrm{N}(A)$. By using property (a) from Definition 1.10, the value is a Poisson random variable with intensity $\lambda\, \mu(S_{a,b}) = \lambda \frac{R^2 L}{2}$.

$$\mathrm{N}(A) \;\sim\; \mathsf{Pois}(\lambda \frac{R^2 L}{2})$$

If n is the number of vertices inside $B_R(x_0)$, its average is $\mathbb{E}(n) = \lambda\pi R^2$. Hence, the exact factor $\frac{n}{2\pi}$ or its approximated version $\frac{\lambda R^2}{2}$ renormalises the distribution to $\mathsf{Pois}(L)$. We therefore have unit density on $[0, n)$ for finite R. Now take the limit $R \to \infty$ to extend this property to the full domain $\mathbb{R}_+$.

For the indendence property (b) consider disjoint $A_1, \dots, A_k$ in $[0, 2\pi)$. Then for each A_i we can construct a preimage before projection as some union of sectors $S_{a,b}$. For simplicity, assume that we have $A_i = [a_i, b_i)$ for all i, so each preimage is simply given by S_{a_i,b_i}. But since these sectors are also a finite disjoint selection of measurable sets, the corresponding vertex counts $\mathrm{N}(S_{a_i,b_i})$ are all independent. The property again carries over to arbitrary $A_1, \dots, A_k$ in $\mathbb{R}_+$ after taking the limit; compare the proof for Lemma 1.11. ■

Lemma 1.13

The limit distribution of an ideal gas S_{Pois} in $\mathbb{R}^2$ is the exponential distribution with density function

$$f_\lambda(t) = \begin{cases} \lambda \exp(-\lambda t), & t \geqslant 0, \\ 0, & t < 0\,, \end{cases}$$

and parameter $\lambda = 1$ due to our normalisation.

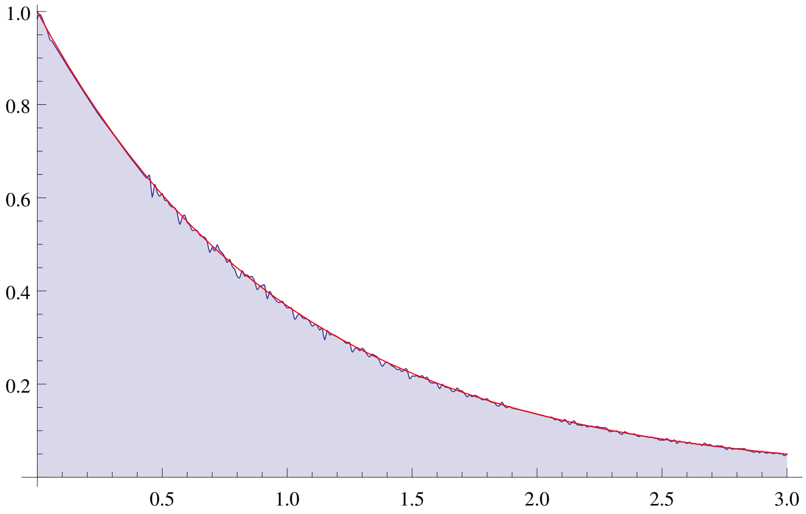

Figure 1.2. Empirical spacing distribution of a Poisson patch together with the exact density function in red.

The empirical distribution in Fig. 1.2 was computed from $n \approx 1.96 \cdot 10^6$ angles.

Proof. We have seen that that a 2-dimensional ideal gas induces a 1-dimensional one after (rescaled) radial projection, which can be identified as a spatial Poisson process in $\mathbb{R}_+$. The distance between consecutive points in such a process is known to be exponentially distributed.

In the probabilistic (temporal) interpretation of a Poisson process, this is the distribution of the waiting time between jumps. ■

Our reference densities therefore are of the following shape.

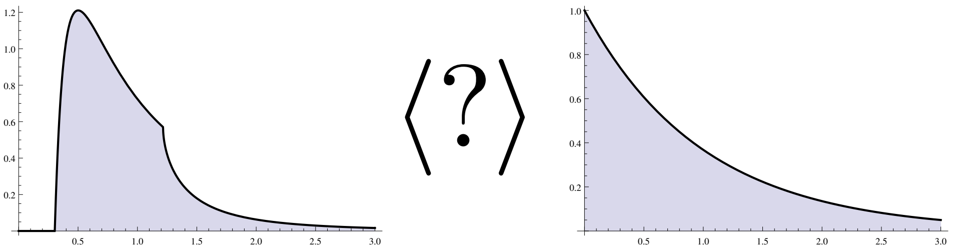

Figure 1.3. Exact density functions for $\mathbb{Z}^2$ and Poisson. Which shapes can be found in-between?

The approximations from our simulations, see Figs. 1.1 and 1.2 show a good match with the corresponding exact density function. This gives us some first hint at how large the amount of samples has to be in order to yield appropriate approximations.

Our interest now is to study other point sets and to check how they fit into this picture, i.e. we want to explore the big question mark in Fig. 1.3. Can one expect some kind of interpolation behaviour between the two reference densities? The primary focus will be on vertex sets coming from aperiodic tilings, since these feature both a repetitive structure and some disorder. In terms of density, one might then expect some "mixture" of the $\mathbb{Z}^2$ and the Poisson case.

We point out that the existence of a limit distribution is known in the two reference cases, as we have seen in Theorem 1.8 and Lemma 1.13. Furthermore, the results in [38, Thm. A.1] and [40] ensure the existence for regular model sets. In all other considered cases, we assume that the distribution exists, which is plausible from the numerics.

Remark 1.14

Consider a sequence $(x_i)_{i \geqslant 0}$ with values in $[0,1]$ and the following properties.

- (a) $x_0 = 0$
- (b) The entries x_i are pairwise distinct.
- (c) The sequence is uniformly distributed in $[0,1]$.

Define S_n as the ordered subset of the first $n+1$ entries of our sequence, i.e.

$$S_n \;=\; \{y_0 < y_1 < \ldots < y_n\}$$

where y_i is some value x_j, $0 \leqslant j \leqslant n$. Rescaling the set via $\overline{S}_n := n \cdot S_n$, gives us, like in Procedure 1.1, mean distance 1 between consecutive entries in $\overline{S}_n$. Denote the entries in $\overline{S}_n$ as $\overline{y}_i$ and define the probability measure

$$\lambda_n \;:=\; \frac{1}{n} \sum_{i=1}^{n} \delta_{\overline{y}_i - \overline{y}_{i-1}}$$

on $\mathbb{R}_+$. If we have a random variable X_n which is distributed according to λ_n, then $\mathbb{E}(X_n) = \frac{\overline{y}_n}{n}$. Since we have property (c), this expression convergences to 1 in the limit $n \to \infty$.

It is desirable to have some criteria for the sequence (x_i) that ensure the existence of a limit $\lim_{n\to\infty} \lambda_n$ as a probability measure. To our knowledge, little is known in this respect beyond [40] and references therein.

1.4. Generalisation to higher dimensions

Let $S \subset \mathbb{R}^d$ be a locally finite point set for an arbitrary dimension d. After a similar argument as in Procedure 1.1, we can always choose the reference point as $x_0 = 0$. Let $R > 0$ and consider the d-ball of radius R around x_0.

$$B_R \;=\; \{x \in \mathbb{R}^d \;:\; \|x - x_0\| \leqslant R\}$$

Like before, we collect the visible points from S with respect to x_0 to create a new set V, then proceed by restricting V to our d-ball,

$$V_R \;:=\; V \cap B_R\,.$$

For each vertex $x \in V_R$, we define the set of angles by

$$\Phi_R(x) \;:=\; \{\varphi \;:\; \langle x|y\rangle = \cos(\varphi)\cdot \|x\|\|y\| \quad \text{for a} \quad y \in V_R,\; y \neq x\}$$

and map x to $d_x := \min \Phi_R(x)$ for the projection step. Computing the distance between neighbouring angles is therefore replaced by taking the minimal distance to another vertex where distance in measured on the surface of the d-ball. After rescaling, the $\overline{d}_x$ are then again used to construct a discrete measure encoding the spacings.

This procedure is already computationally expensive for $d = 3$ since determining the closest vertex requires either an exhaustive search or at least the application of some $\mathbb{R}^3$ space partitioning algorithms, e.g. an Octree based approach; compare [41].

Since little is known already in the planar case, we concentrate on the latter and leave higher dimensions to future work.

CHAPTER 2

Planar aperiodic tilings

This chapter functions as an introduction and survey for the point sets that we have considered as input for the RPM.
We provide a short summary for each tiling, go over some of the interesting properties and then present a histogram that approximates the limit distribution. The questions arising from this procedure, namely construction of large tiling patches and determining the subset of visibile vertices, are covered separately in the later Chapters 3 and 4.

2.1. Preliminaries

We briefly introduce some concepts and notation for later use.

Definition 2.1
Let κ be an algebraic integer with the following properties.

(1) $\kappa > 1$
(2) $|\sigma(\kappa)| < 1$ for all non-trival algebraic conjugations σ of $\mathbb{Q}(\kappa)$, i.e. all the conjugates of κ lie in the open unit disc; also compare [5, Ch. 2.5].

Then, κ is called a *Pisot–Vijayaraghavan* number, or PV number for short. Such numbers appear e.g. scaling factors for inflation tiling; see Definition 2.3 below.

Remark 2.2
Consider a primitive root of unity $\zeta := \exp(2\pi \mathrm{i}/n)$ of order n $(n > 2)$. Then, the corresponding cyclotomic field $\mathbb{Q}(\zeta)$ is constructed by adjoining ζ to the rationals. We are mostly going to work with the integers inside $\mathbb{Q}(\zeta)$, which we denote as $\mathbb{Z}[\zeta]$. Some additional properties of these integers are introduced in Chapter 4, where we discuss visibility of vertices in tilings.
For more information on cyclotomic fields see [49].

There are essentially three methods to produce aperiodic tilings of the plane. The first one is by defining a set of prototiles with matching rules. This method is not suitable for the purpose of implementation. We therefore focus on the alternatives, namely inflation and projection.

Definition 2.3 (Inflation of prototiles)
Given a finite set of tiles $\{t_1, \ldots, t_n\}$, think of each t_i as some convex set with nice boundaries for now, and a scalar $\lambda > 0$, an *inflation rule* describes a recipe how to substitute a scaled version λt_i of a tile as a union of translated and

rotated copies of the original tiles. This recipe is subject to some restrictions concerning volume and disjointness of the tiles, see in particular [5, Def. 5.17] and the surrounding chapter.

Remark 2.4
An important subclass are the *stone inflations*, which we first encounter in Section 2.2 when looking at the Ammann–Beenker tiling. There, we work with a set P of prototiles, where the rescaled tile is dissected into copies, i.e. the volume of λt_i is preserved. The result of this two-stage process then includes rotated and reflected versions of tiles from P, which are again handled with the corresponding rotated/reflected rule.
We can now start with some tile $t \in P$ and apply the rule N times, resulting in a finite patch $\mathcal{P}$ of the tiling. From the patch we extract the vertices simply by discarding the edges. As discussed in Procedure 1.1, we are mostly interested in circular patches, hence we inspect $\mathcal{P}$ for subpatches with circular configuration. A suitable subpatch is then used as seed to create large patches for the radial projection.

A different possibility to construct tilings is given by the cut-and-project method. The advantage here is that it directly yields vertices of the tiling and does not require keeping track of the adjacency information, i.e. the edges of the tiles. Another reason for choosing this description, if applicable, is that some configurations admit a much easier condition to determine visibility of a given vertex by using local information only. In this regard, such cases behave similar to $\mathbb{Z}^2$ together with the GCD-test of the coordinates.

Definition 2.5
Consider the triple $(\mathbb{R}^d, \mathbb{R}^k, \mathcal{L})$ with $d, k \in \mathbb{N}$ and projections π, π_{int} that satisfy the following conditions,

(i) $\mathcal{L}$ is a lattice in $\mathbb{R}^d \times \mathbb{R}^k$;
(ii) $\pi \colon \mathbb{R}^d \times \mathbb{R}^k \to \mathbb{R}^d$, with $\pi|_{\mathcal{L}}$ injective;
(iii) $\pi_{\text{int}} \colon \mathbb{R}^d \times \mathbb{R}^k \to \mathbb{R}^k$, with $\pi_{\text{int}}(\mathcal{L}) \subset \mathbb{R}^k$ dense.

This setup is called a *cut-and-project scheme* (CPS). If we let $L := \pi(\mathcal{L})$, the conditions above induce a function

$$\star : \; L \longrightarrow \mathbb{R}^k$$

by composing π^{-1} and π_{int}. We denote this function as the *star map* and write $x^\star$ for $\star(x)$.

Remark 2.6
The notation $x^\star$ makes sense since the map is a natural extension of the algebraic conjugation for all our cases. Our lattice can then be written as *diagonal embedding*,

$$\mathcal{L} \;=\; \{(x, x^\star) \;:\; x \in L\} \;.$$

A CPS is usually encoded in a diagram. The right hand side in Fig. 2.1 describes the *internal* space, the left one the *direct* or *physical* space. The physical space is the domain where the point set of the tiling lives.

$$\begin{tikzcd}
\mathbb{R}^d & \mathbb{R}^d \times \mathbb{R}^k \arrow[l, "\pi"'] \arrow[r, "\pi_{\text{int}}"] & \mathbb{R}^k \\
\pi(\mathcal{L}) \arrow[u, hook] \arrow[d, equal] & \mathcal{L} \arrow[l, "\text{1-1}"'] \arrow[r] \arrow[u, hook] & \pi_{\text{int}}(\mathcal{L}) \arrow[u, hook, "\text{dense}"'] \arrow[d, equal] \\
L \arrow[rr, "\star"] & & L^{\star}
\end{tikzcd}$$

Figure 2.1. General case of a Euclidean CPS.

Details about the generic definition can be found in [47, 5]. Given a Euclidean CPS as defined above, a *projection set* comes from choosing a subset $W \subset \mathbb{R}^k$ and considering the set

$$\text{⅄}(W) \ := \ \{x \in L \ : \ x^{\star} \in W\} \ .$$

The subset W is called the *window* of the projection set, or sometimes also denoted by *acceptance region* or *occupation domain.* If W is relatively compact and has non-empty interior, $\text{⅄}(W)$ is denoted as *model set.*

It can be shown that point sets of many aperiodic inflation tilings can also be generated using this approach. This is also one important aspect for our implementation purpose, since the main work now consists of generating a suitable "cutout" $L_0 \subset L$ and then applying the window condition $x^{\star} \in W$ to each $x \in L_0$. In this regard, W tells us which vertices are accepted into the model set.
Since generic model sets are a broad topic, we restrict ourself to the more manageable subclass of cyclotomic type in the following. It should also be emphasised that we only consider model sets with physical space $\mathbb{R}^2$, for reasons pointed out in Section 1.4. There are many interesting and important generalisations, in particular with respect to more general internal spaces beyond the Euclidean case, but we shall not use this type of description below.

Definition 2.7
Let $(G, +)$ be a group and $A, B \subseteq G$ subsets. Then, we define

$$A + B \ := \ \{a + b \ : \ a \in A, \ b \in B\}$$

as the *Minkowski sum* of A and B.

Definition 2.8
Let $f \colon A \to B$ be a map between sets A and B, then we denote by $\Im(f) \subseteq B$ the *image* of f.

Let us now describe how one can reconstruct the density function from the RPM data.

Procedure 2.9
Consider a probability measure ν_R for some radius $R > 0$ as given in Procedure 1.1. Under the assumption that, for R large enough, ν_R approximates our sought-after limit distribution, we can reconstruct the corresponding density function, up to some error, with the following procedure.
Let $I := [a, b)$ be some interval and $d > 0$ the width, which we use to subdivide I. We use a uniform subdivision into subintervals, commonly denoted as *bins*, i.e.

$$b_i \;:=\; [a + i \cdot d, a + (i+1) \cdot d) \quad \text{for} \quad 0 \leqslant i < N,\; N \;:=\; \lfloor \frac{b-a}{d} \rfloor \,.$$

To make sure that the b_i cover the whole interval, we usually enforce that the length of I is an integer multiple of d. For each Dirac entry δ_{d_j} in our measure ν_R, we locate the index i of the bin that satisfies $d_j \in b_i$. If such an index exists, we count this event for b_i. Denote the total number of such occurences as h_i, the *height* of the bin.

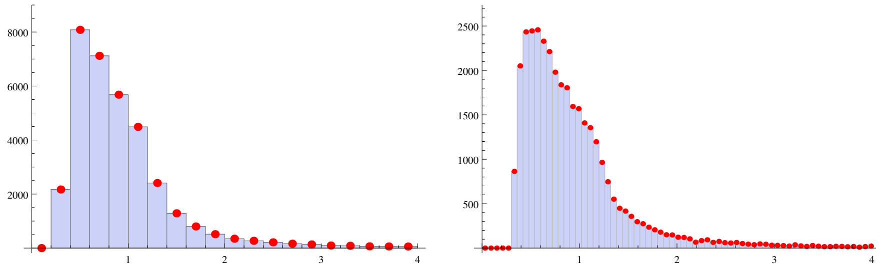

Figure 2.2. Histogram bins for the interval $[0, 4)$ with $d = 0.2$ (left) and $d = 0.06$ (right). The input data is the $\mathbb{Z}^2$ patch that we already used in Fig. 1.1.

After each height is computed, we can already extract a approximation of step function type of the density from Fig. 2.2. Increasing the resolution of the binning, i.e. moving from the left to the right hand side in Fig. 2.2, suggests that we approximate a continuous object here, in the limit $R \to \infty$. With this in mind, we proceed by applying two additional steps.

(1) As, per construction, ν_R is a probability measure, we rescale the computed heights. For this, we also have to consider the entries δ_{d_j} outside $[a, b)$. If k is the number of entries, then we multiply with $(k \cdot d)^{-1}$.
(2) Assuming that the subdivision is fine enough, we collect the midpoints of our b_i (indicated in red in Fig. 2.2) together with the corresponding rescaled heights.

We can now apply a spline interpolation [45, Sec. 3.3] through these new coordinates, obtaining an approximation of the density function for the corresponding empirical distribution. For simplicity, we continue to denote the plots of such approximations as *histogram* .
For the computation of these empirical distributions in the following sections, we mostly used either $d = 0.01$ or $d = 0.02$ for the subdivision. Some a posteriori adjustment of the subdivision and the patch size followed to reduce the interpolation error.

2.2. Ammann–Beenker

We employ the *Ammann–Beenker* (AB) tiling in its classic version [1, 5] with a triangle and a rhombus. It admits a stone inflation with prototiles

$$P_{\mathsf{AB}} \;=\; \{t_A, t_B\}\,,$$

where the triangle t_A is inflated as given below.

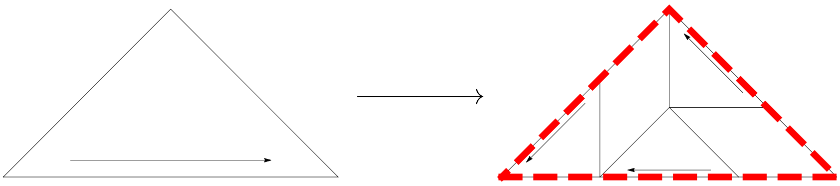

Figure 2.3. Inflation rule for the AB tiling, part 1.
Tile t_A maps to $3 \times t_A$ and $2 \times t_B$.

The triangle appears in the tiling with both chiralities, and the other chirality uses the reflected rule. The rhombus t_B appears without chirality and is inflated according to the following rule.

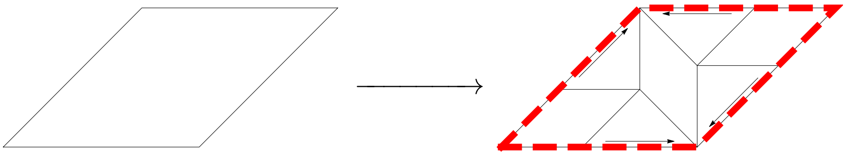

Figure 2.4. Inflation rule for the AB tiling, part 2.
Tile t_B maps to $4 \times t_A$ and $3 \times t_B$.

To make the dissection process work, i.e. to end up with tiles from P_{AB} again, the inflation multiplier has to be chosen as

$$\lambda_{\mathsf{AB}} \;=\; 1 + \sqrt{2}\,,$$

which is the *silver mean*. One can see that λ_{AB} is the positive root of the polynomial $p(x) = x^2 - 2x - 1$. Furthermore, it is a PV number since the algebraic conjugate is $1-\sqrt{2} \approx -0.4142$. The properties of the inflation multiplier are important, because there is a relation between the algebraic type of λ_T and regularity of the tiling T. Inflations of PV type seem to admit more regular tiling structures [5, Ch. 2.5]. Also, compare Section 2.6 for an example of a less regular case.

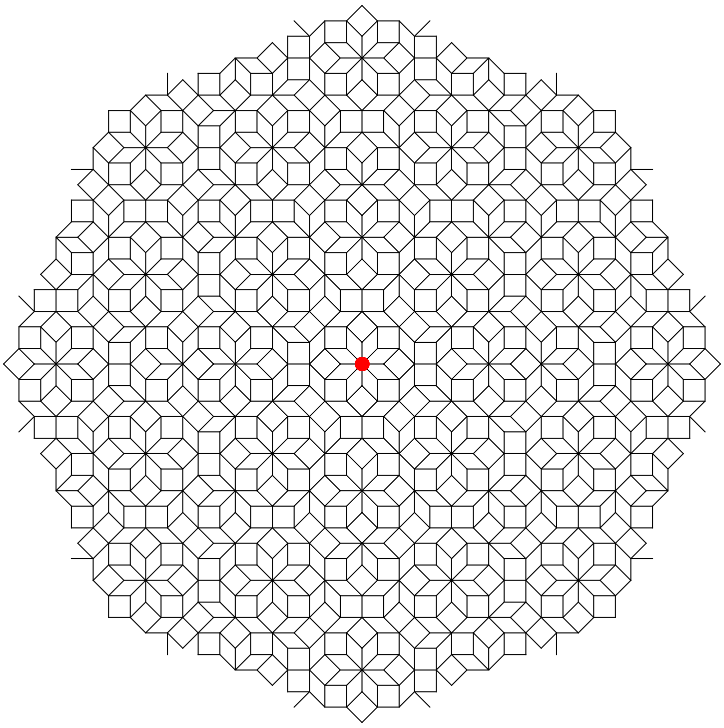

Figure 2.5. Patch of the AB tiling with perfect D_8 symmetry. Origin indicated with red marker.

A nice property of the AB tiling is that it can also be described as a cyclotomic model set [5, Ex. 7.8]. It corresponds to the diagram in Fig. 2.1 of cyclotomic type with parameter $n = 8$. The tiling vertices can therefore be described as the set

$$T_{\mathsf{AB}} \;=\; \{x \in \mathbb{Z}[\zeta_8] \;:\; x^{\star} \in W_8\}\;,$$

where the $\star$-map is given by the field extension of $\zeta_8 \mapsto \zeta_8^3$ and the window W_8 is a regular octagon centered at the origin. The octagon has edge length one, see Fig. 4.1 for its orientation. This configuration is non-singular, i.e. we do not encounter any vertices x with $x^{\star} \in \partial W_8$.

Also note that the maximal real subring of $\mathbb{Z}[\zeta_8]$ is $\mathbb{Z}[\sqrt{2}]$, with fundamental unit λ_{AB}, which connects the two descriptions on an algebraic level.

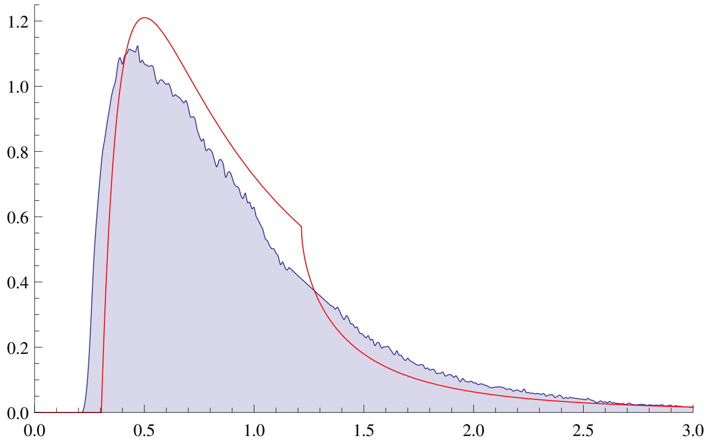

Figure 2.6. Empirical distribution of the radial spacings of a D_8-symmetric AB patch. The exact density function of $\mathbb{Z}^2$ is overlayed in red.

We see that the histogram, which was computed from approximately $1.8 \cdot 10^6$ vertices, features several characteristics which we have already observed for $\mathbb{Z}^2$. Let us mention three characteristic features.

(1) A pronounced gap is present where the distribution has zero mass.
(2) The middle section, here roughly extending from 0.2 to 1.4, comprises the bulk of the mass.
(3) A tail section exists, with a specific power law decay behaviour.

Unless stated otherwise, we will always overlay the $\mathbb{Z}^2$ density for comparison.

As explained in Procedure 1.1, the radial projection only considers the *visible* vertices from the chosen reference point, here the origin. We give some statistics in Table 2.1 about the number of (all) vertices and visible vertices, depending on the patch size. The quantity *steps* roughly measures how far we move along edges of the tiles, and is explained in more detail in Chapter 3.
At the end of this chapter, we briefly explore the effect of moving the reference point to some other vertex of the tiling. For now, we are going to stick with the canonical choice of the origin.

Table 2.1. Visibility statistics for the D_8-symmetric AB tiling.

steps	vertices	visible	proportion
40	561	327	58.2%
400	47713	27561	57.7%
1500	662265	382221	57.7%
2500	1835941	1059753	57.7%

We want to verify the empirical proportion in Table 2.1. From [5, Ex. 7.8] we know the density of the AB tiling as

$$\mathrm{dens}(T_{\mathsf{AB}}) \;=\; \frac{\lambda_{\mathsf{AB}}}{2} \;\approx\; 1.207\,.$$

The density of the visible points V_{AB} of the tiling can be expressed in terms of the generalised zeta function [48]

$$\mathrm{dens}(V_{\mathsf{AB}}) \;=\; \zeta^{-1}_{\mathbb{Z}[\sqrt{2}]} \;\approx\; 0.6969\,.$$

Combining these two values recovers a value of approximately 0.5773 for the proportion, which is pretty close to the values from our simulations. We are going to encounter $\zeta_{\mathbb{Z}[\sqrt{2}]}$ again in Section 7.3, when we study a visibility property induced by algebraic properties of the vertex.
For an overview of the histogram statistics, see Table 2.2 in Section 2.5 below.

2.3. Tübingen triangle

The *Tübingen triangle* (TT) tiling is another case which can be described either via inflation rules or as a model set. Again, we start with a set of two prototiles $P_{\mathsf{AB}} = \{t_A, t_B\}$, both triangles this time, where t_A is inflated via

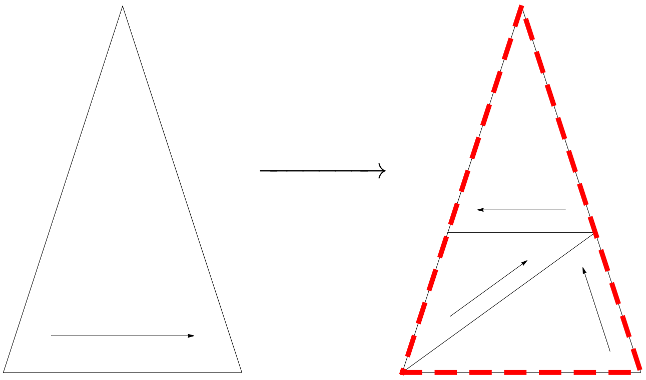

Figure 2.7. Inflation rule for the TT tiling, part 1.
Tile t_A maps to $2 \times t_A$ and $1 \times t_B$.

and t_B with the rule below.

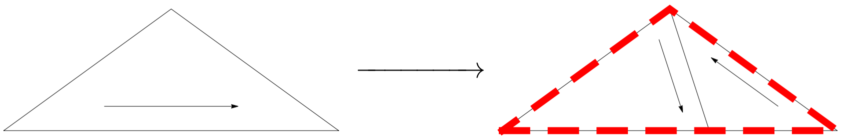

Figure 2.8. Inflation rule for the TT tiling, part 2.
Tile t_B maps to $1 \times t_A$ and $1 \times t_B$.

For reasons explained later, we prefer the description as model set. In this context, the TT tiling is a decagonal case of a cyclotomic model set with planar window (see [8, 7] and [5, Ex. 7.10]). The underlying module is $\mathbb{Z}[\zeta_5]$, with maximal real subring $\mathbb{Z}[\tau]$, where

$$\lambda_{\mathsf{TT}} \;=\; \tau \;:=\; \frac{\sqrt{5}+1}{2}$$

is again both the fundamental unit of the ring $\mathbb{Z}[\zeta_5]$ and the multiplier for the corresponding inflation rule. Note that τ is also known as the *golden ratio*. Fig. 2.9 shows a circular patch generated from applying the inflation rule four times.

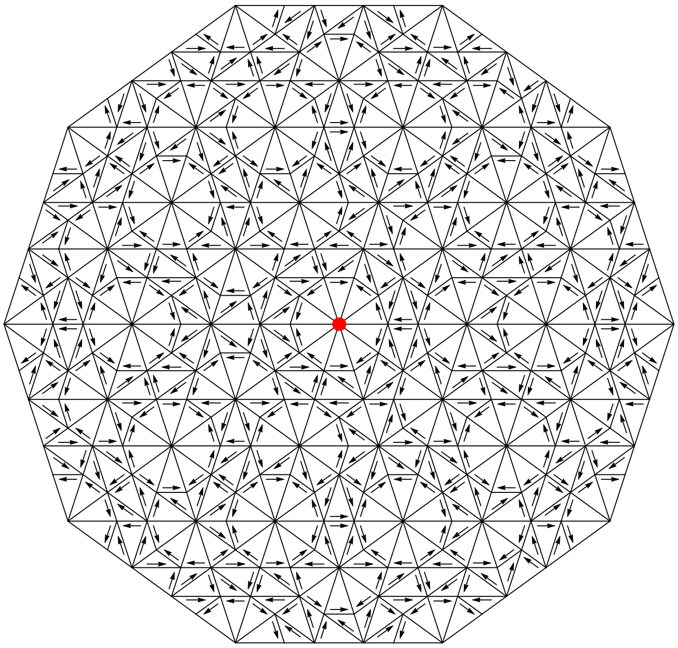

Figure 2.9. Patch of the TT tiling after 4 inflations of the central patch. Origin indicated with red marker.
Note that the patch is D_5-symmetric, while the corresponding infinite tiling has statistical D_{10} symmetry, see [5] for details.

The central patch consisting of 10 prototiles of type t_A is legal [1], which can be seen by inflating t_A five times in Fig. 2.10. For the computation of the vertices used for the radial projection, again the model set description

$$T_{\mathsf{TT}} \;=\; \{x \in \mathbb{Z}[\zeta_5] \;:\; x^\star \in W_{10} + s\}$$

---

[1] If we have a substitution ϱ on an alphabet, then a word is *legal* if it appears as subword of $\varrho^k(s)$ for some seed s, see [5, Def. 4.5] for details. In our setting the seeds are the prototiles, and the words are the patches.

was employed. The window W_{10} is a decagon with edge length $\sqrt{(\tau+2)/5}$, and like the AB window, the right-most edge is perpendicular to the x-axis. Here, the $\star$-map is the field extension of $\zeta_5 \mapsto \zeta_5^2$. In this case, we need to apply a small generic shift s to the window to avoid singular vertices, meaning vertices that stem from the boundary of W_{10}. Such vertices are difficult to handle because of precision issues when testing for the window boundary. Moreover, such singular cases fail to be repetitive and actually correspond to an overlay of several tilings. This results in the addition of extra points (of 0 density) which is undesirable. We therefore restrict our attention to non-singular configurations.

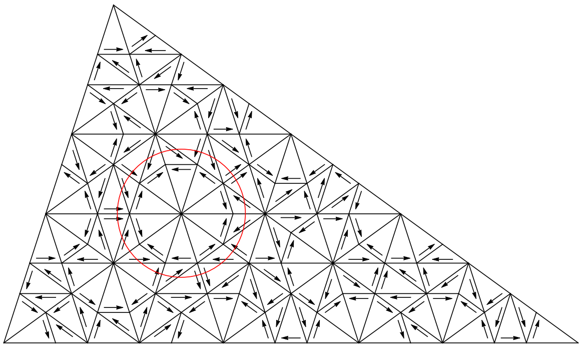

Figure 2.10. Patch produced from five inflation steps applied to a TT prototile of type t_A. Encircled in red is the seed used in Fig. 2.9.

In our case, we use $s := 10^{-4} \cdot (1,1)$ as the shift. The important aspect here is not to move in the direction of the window edges. Evaluation with a patch of suitable size ($\approx 1.5 \cdot 10^6$ vertices) produces the following histogram.

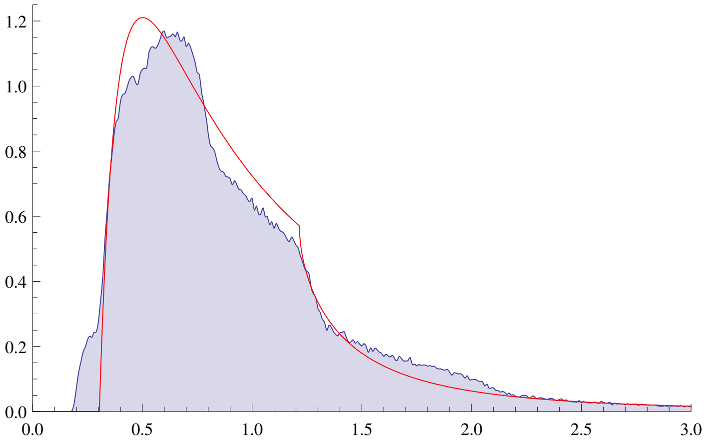

Figure 2.11. Empirical spacing distribution of a TT patch.

While being similar to the AB histogram on a global scale, there are numerous differences in detail, especially in the bulk. This one features more structure, in terms of areas resembling plateaux, and is also nicely aligned to the $\mathbb{Z}^2$ density function.

Zooming into the area near the gap and taking the piecewise composition of the density function for $\mathbb{Z}^2$ in account, the data might even suggest that the bulk decomposes into smaller components.

1. First component: $(0.18, 0.3)$
2. Second component: $(0.3, 0.5)$
3. Third component: $(0.5, 1.3)$

At present, the underlying mechanism for this structure is unclear.

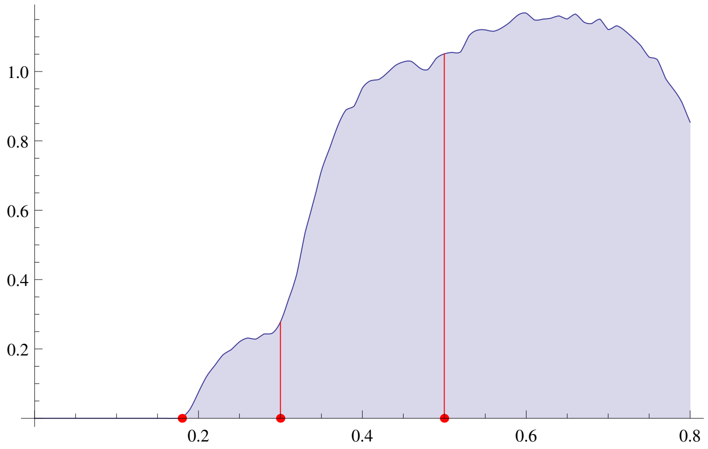

Figure 2.12. Zoom near the gap of the empirical TT distribution.

Again, the statistics can be found in Table 2.2 below.

A related example of a distribution in closed form, for the *golden L* (which is not a tiling system), has recently been described by Athreya et al. [3]. It bears strong resemblence with Fig. 2.11, thus making it fall into our “ordered regime”. This supports the existence of universal features in this approach.

A coarse observation here is that it seems possible to reconstruct the function in Fig. 2.11, to some extent, by overlaying multiple copies of the $\mathbb{Z}^2$ reference densities; see $g(t)$ in Theorem 1.8. If we let

$$h_{d,e}(t) \;:=\; (1-e)\cdot g(t) + e\cdot g(t-d)$$

for parameters $0 \leqslant e \leqslant 1$ and $d > 0$, then $h_{d,e}$ provides a rough approximation, which still displays the aforementioned bulk decomposition property.

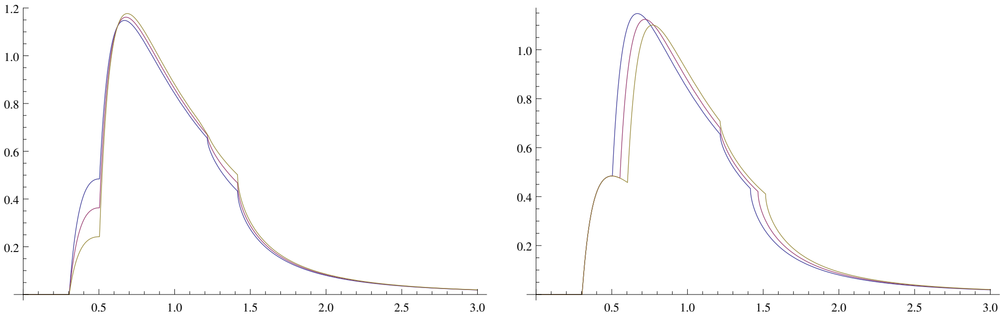

Figure 2.13. The function $h_{d,e}(t)$ for $d = 0.2$, $e = 0.6, 0.7, 0.8$ (left) and $e = 0.6$, $d = 0.2, 0.25, 0.3$ (right).

One can see in Fig. 2.13 that wiggling around with the parameters d and e allows for a wide range of shapes. We ask if this approach can be extended to the other cases, and if applicable, does it imply that we can reduce some of the problems here to the $\mathbb{Z}^2$ case?

2.4. Gähler shield

The *Gähler shield* (GS) tiling [23, Ch. 5] is our last cyclotomic model set with internal space $\mathbb{R}^2$. It uses a dodecagonal configuration [5, Ex. 7.12] and is also interesting in its algebraic properties, which make the visibility test slightly more involved. Note that similar to the TT tiling we only have statistical 12-fold symmetry of the tiling. In particular the finite patches we are working with are not 12-fold symmetric. The vertex set is

$$T_{\mathsf{GS}} \;=\; \{x \in \mathbb{Z}[\zeta_{12}] \;:\; x^\star \in W_{12} + s\}$$

with the $\star$-map defined by extension of $\zeta_{12} \mapsto \zeta_{12}^5$. The window W_{12} is a dodecagon with edge length one and the usual orientation. Again, a shift s has to be applied to avoid singular vertices. The underlying $\mathbb{Z}$-module decomposes into

$$\mathbb{Z}[\sqrt{3}] \oplus \mathbb{Z}[\sqrt{3}] \cdot \zeta_{12} \quad \text{with} \quad \lambda_{\mathsf{GS}} := 2 + \sqrt{3}$$

generating the unit group of $\mathbb{Z}[\sqrt{3}]$. As with the AB and TT cases, also here a description using inflation rules can be given. The “shield” part of the tiling name comes from the prototile in the lower-right corner of Fig. 2.14. Note that this description includes an unwanted rotation by $\pi/12$; compare [5, Rem. 6.8]. This is one of the reasons why we again use the model set description here.

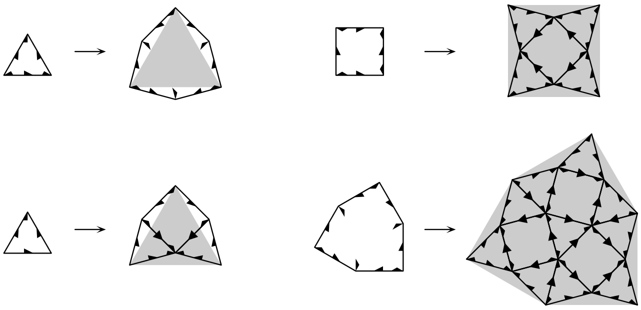

Figure 2.14. Inflation rules for the GS tiling using four (marked) prototiles. A stone inflation requires tiles with fractal boundaries; see [5, Rem. 6.9]

While still retaining the known three-fold structure of the previous two cases in it distribution, the GS tiling gravitates towards the slope-like characteristic of the Poisson case. A certainly new property is the existence of two local maxima in the bulk. In Chapter 5, where we study the effects of randomisation on the radial projection, we see that this property appears to be quite “robust”.

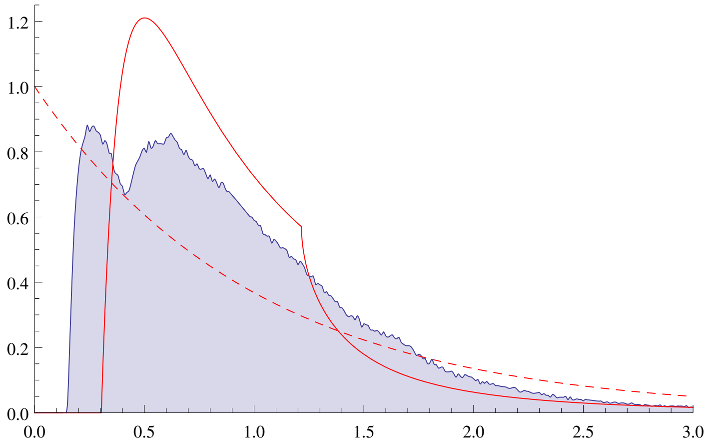

Figure 2.15. Empirical spacing distribution of a GS patch.

Obviously here neither the $\mathbb{Z}^2$ density, nor the Poisson density, overlayed as dashed red curve, provides a particular good fit. Some approach using the functions $h_{d,e}(t)$ from above might be more fruitful, but we did not try this here.

2.5. Tail statistics

It seems natural to compute statistical data (like variance and skewness) to analyse our histogram data. We choose not to do so, since this can be misleading, because such numbers will not be quantities of universal nature in our context.

In fact, there is another and more serious reason. One can see from the explicit density function $g(t)$ of the $\mathbb{Z}^2$ case in Theorem 1.8 that the moments of order $k \geqslant 2$ fail to exist. A Taylor expansion gives

$$g(1/t) \;=\; \frac{36}{\pi^4}t^3 + \frac{162}{\pi^6}t^4 + \mathcal{O}(t^5) \quad \text{for} \quad t \to 0_+ \;,$$

thus characterising the decay behaviour of the tail. Hence, any of the usual statistical quantaties only exists because of finite-size effects, i.e. because we can only compute finite patches.

Instead of the statistics, we provide the coefficients c_k of t^k (usually two values are good enough) when the tail of the respective histogram can be fitted with a power law.

Table 2.2. Statistical data generated from radial projection (the mean is always 1.0).

tiling	gap size	c_3	c_4	e	k
$\mathbb{Z}^2$	0.304	0.369	0.168	—	—
AB	0.222	0.248	0.496	2.79	38560
TT	0.182	0.239	0.513	2.60	31376
GS	0.152	0.232	0.547	4.75	67524

The power law fitting was done for the tail starting at position 3.0. We indicate the quadratic error of the approximation by e in units of 10^{-10} and the amount of data points by k.

More statistical data for the other tiling cases we considered can be found in Table 2.3 on page 29.

2.6. Lançon–Billard

We have seen that the previous three tilings are qualitatively close to the order properties of the $\mathbb{Z}^2$ lattice. A similar behaviour of cyclotomic model sets can also be seen in the mildly related case of discrete tomography [30]. One might guess that all kind of deterministic aperiodic tilings behave that way. However, it turns out that this is not the case.

The chiral *Lançon–Billard* (LB) tiling [36] is an example of an inflation-based tiling with a non-PV multiplier given by

$$\lambda_{\mathsf{LB}} \;=\; \sqrt{\frac{1}{2}\bigl(5+\sqrt{5}\bigr)} \;.$$

The inflation rule applies to two rhombic prototiles of unit edge length (see Fig. 2.16 and Fig. 2.17).

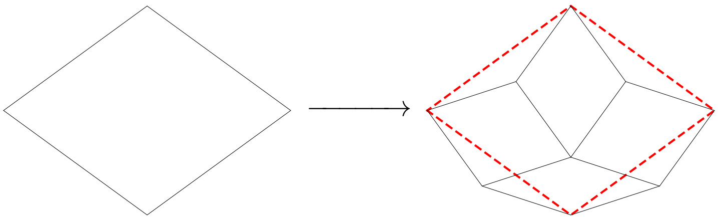

Figure 2.16. Inflation rule for the LB tiling, part 1.
Tile t_A maps to $3 \times t_A$ and $1 \times t_B$.

The resulting tiling vertices live in $\mathbb{Z}[\zeta_5]$ (see [5, Ch. 6.5.1] for details, also concerning the non-PV property of λ_{LB}), like the TT tiling above.

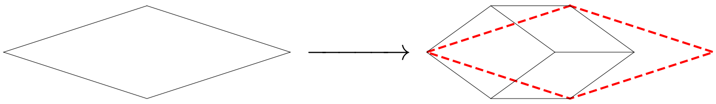

Figure 2.17. Inflation rule for the LB tiling, part 2.
Tile t_B maps to $1 \times A$ and $2 \times B$.

The LB tiling admits no model set description and it fails to be a stone inflation, as one can see from the above rules.
By multiple inflation of one tile t_A, one can isolate a legal patch of circular shape that is comprised of five tiles of type t_A. We use this configuration as our initial seed to grow suitable patches.

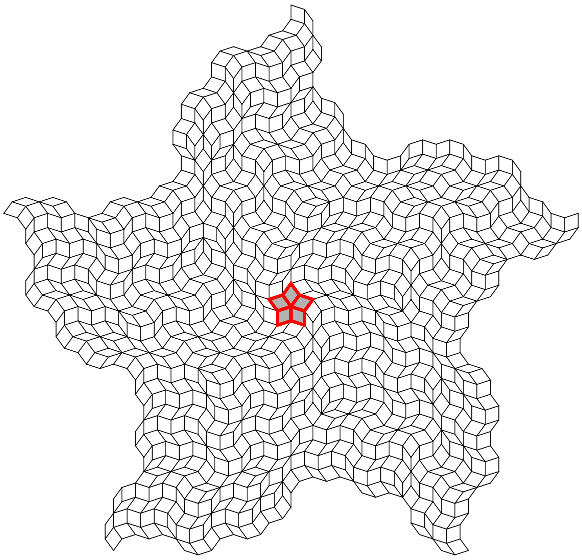

Figure 2.18. Fivefold symmetric patch of the chiral LB tiling after 4 inflations of the initial patch.

The computed patches are C_5 symmetric and begin to show a high amount of spatial fluctuation when increasing the number of inflation steps (the histogram in Fig. 2.19 was computed after applying 12 inflations).

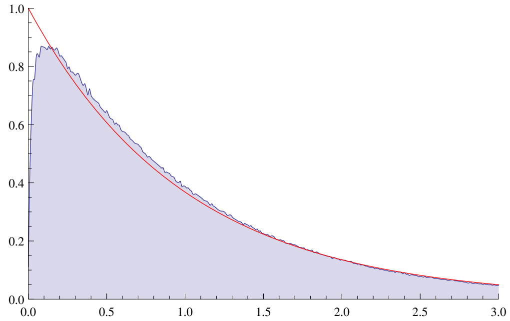

Figure 2.19. Empirical spacing distribution of a LB patch, with the exponential distribution overlayed.

While not exactly matching the exponential distribution from the Poisson case, the radial projection appears to be sensitive to the higher amount of spatial disorder in this tiling. In particular, it shows an exponential rather than a power law decay for large spacings. For histogram statistics, see Table 2.3 on page 29.

2.7. Planar chair

After this encounter of radial disorder, we want to go back and explore the other side of our order spectrum some more.

The planar chair tiling [26] is an example of an inflation tiling with integer multiplier $\lambda_{\text{chair}} = 2$. It works with just one L-shaped prototile and can produce patches with D_4 symmetry. There also exists a model set description [5], but with a more complicated 2-adic internal space. We thus employ the inflation method here.

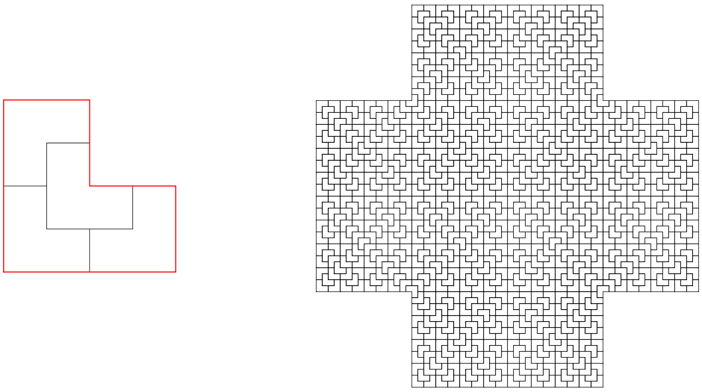

Figure 2.20. Inflation rule (left) and D_4 symmetric patch (left) of the chair tiling.

The vertices of the tiling are a subset of the $\mathbb{Z}^2$ lattice, where we already know the limit distribution. Because of this "proximity", we expect the radial projection to behave similarly. In particular, we were interested in the impact of the visibility condition on the histogram. Since we are only working with a subset, the test using the GCD of the coordinates does not work here.
Consider a vertex $x := (a, b)$ which is not coprime, say with $\gcd(a, b) =: k > 1$. For the $\mathbb{Z}^2$ lattice, one knows that $\tilde{x} := (\frac{a}{k}, \frac{b}{k})$ is an element of the set and therefore occludes x. In this case $\tilde{x}$, might not be element of the vertex set.

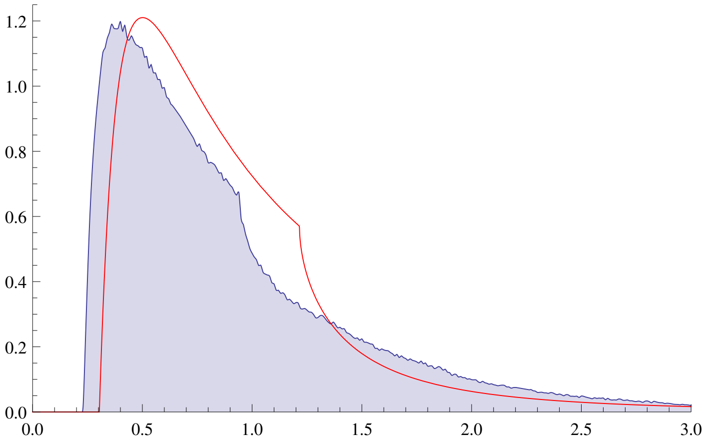

Figure 2.21. Empirical spacing distribution of a `chair` patch using the (wrong!) GCD criterion for the visibility test.

Comparing the results in Fig. 2.21 and 2.22 shows that applying the correct test is significant and, based on numerical evidence, also doesn't cancel out in the limit.

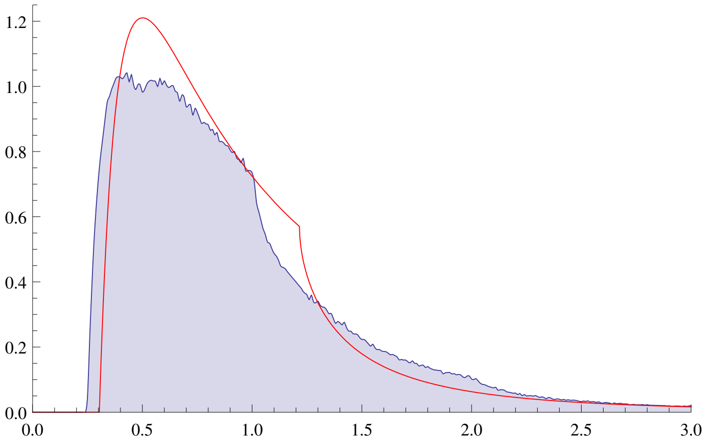

Figure 2.22. Empirical spacing distribution of a `chair` patch using the correct visibility test.

2.8. Miscellanea

The tilings considered in the previous sections indicate that our method gives at least partial information about the order of the point set. Let us briefly look at some other examples.

The *Penrose–Robinson* (PR) tiling is similar to the TT tiling on the level of the inflation rule. It uses the same prototiles, but a different dissection rule [5, Ch. 6.2] after blowing up the tiles by the inflation factor $\lambda_{\mathsf{PR}} = \tau$.

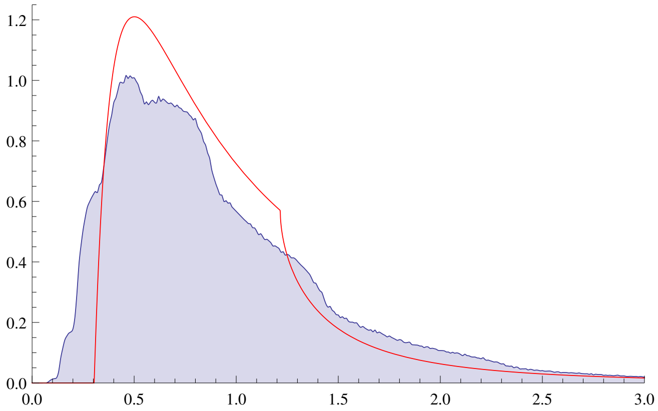

Figure 2.23. Empirical spacing distribution of a PR patch.

Even though it shares these features with the TT, the resulting distribution is rather different. In particular, the number of plateau areas in the bulk has increased from 2 to 4 here.

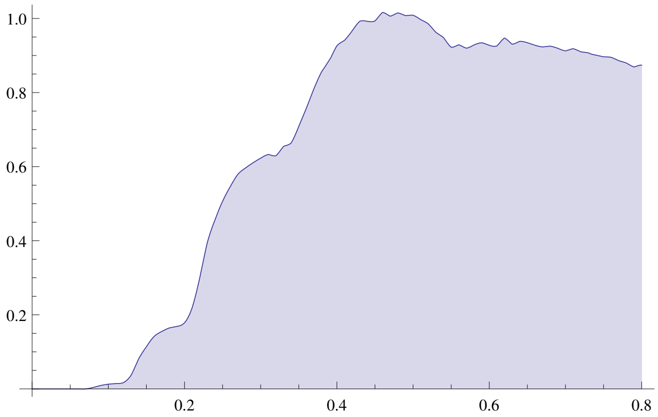

Figure 2.24. Zoom near the gap of the empirical PR distribution.

Another tiling of *Penrose*-type can again be implemented by using a model set description. This rhombic Penrose (RP) tiling [7] is special in that it uses a multi-window configuration [5, Ex. 7.11]. Here, the CPS in Fig. 2.1 is fixed, but multiple windows W_i are used. Define the homomorphism

$$\kappa : \mathbb{Z}[\zeta_5] \longrightarrow \mathbb{Z}/5\mathbb{Z} \quad \text{by} \quad \kappa(\sum_i c_i \zeta_5^i) := \sum_i c_i \bmod 5 \, .$$

Then, the window W_i for which the vertex $x \in \mathbb{Z}[\zeta_5]$ is tested, is chosen depending on $\kappa(x)$.

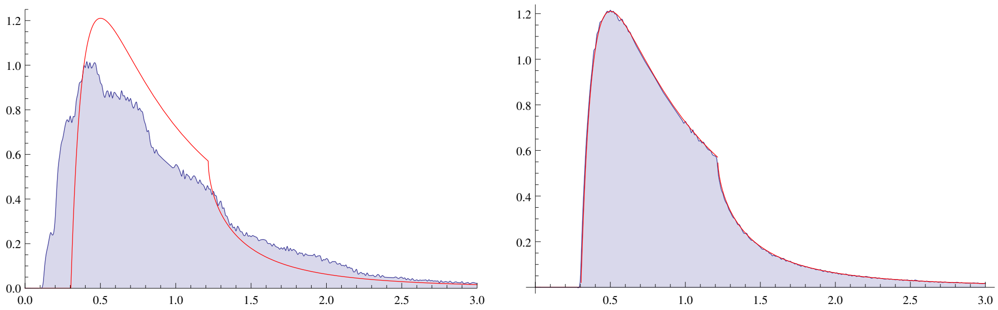

Figure 2.25. Empirical spacing distribution of a RP (left) and triangular (right) patch.

As we pointed out before, the construction as model set allows for an easier description of the subset of visible vertices. However, the patches for this case had to be generated using a generic visibility test. Although the vertices coming from different W_i are disjoint, there is still occlusion between the sets. Hence, we cannot determine the visible subset for each W_i individually and then consider the union of these subsets.

Also included in Fig. 2.25 is the result for the a patch of the triangular tiling $\mathcal{T}_{\mathsf{tri}}$, where the vertex set is just the hexagonal lattice. The set is closely related to our reference set $\mathbb{Z}^2$ since $\mathcal{T}_{\mathsf{tri}}$ is derived from $\mathbb{Z}^2$ by applying a shearing transformation. Also, the visibility of a vertex can be computed using the GCD of the coordinates. We see that the radial projection apparently is insensitive to this transformation, and further numerical tests indicate this this applies to any shearing map.

Table 2.3. Statistical data for the other considered tilings (e is the error term).

tiling	gap size	c_3	c_4	c_5	e
LB	0.0030	—	—	—	—
chair	0.2536	0.229	0.538	—	$5.07 \cdot 10^{-10}$
PR	0.0783	0.066	1.339	—	$1.81 \cdot 10^{-10}$
RP	0.1169	0.459	-2.432	8.395	$0.14 \cdot 10^{-10}$

From [10], we know that the shape of the expanding region, in our setting always a disc, plays a fundamental role in the limit distribution. In particular an ellipse, i.e. a disc after shearing, would yield a different result here. We therefore ask how “lenient” the radial projection is here, i.e. which subset of transformation leaves the distribution invariant?

Since the symmetry property of the tiling seems to play a large role in determining the shape of the spacings distribution, we tried to utilise the CPS framework once again.

If we choose $L := \mathbb{Z}[\zeta_7]$ in Definition 2.5, then for a planar physical space, i.e. $d = 2$, the internal space becomes $\mathbb{R}^4$. As window we appointed a 4-ball with radius $r^2 = 7.25$. We denote this setting as simple heptagonal.

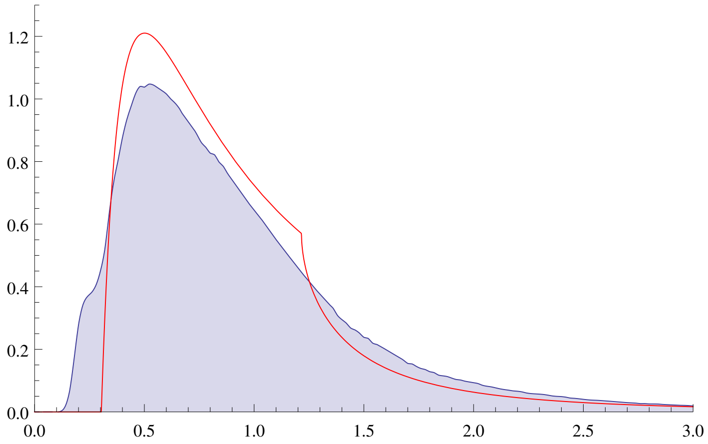

Figure 2.26. Empirical spacing distribution of a heptagonal patch.

Somewhat surprisingly no obvious new feature can be found here except, perhaps, a tendancy towards a higher degree of (local) smoothness of the distribution function. It would be interesting to evaluate how much influence the window has for this configuration. For example, choosing some regular polyhedron or even a unconnected union of such. Due to time constraints and the fact that we did not develop generic code that works for all CPS of cyclotomic type (the case n being a prime is already the simplest case here), we did not explore the realm of $n \geqslant 13$.

2.9. Non-canonical reference point

The decision to select the origin of the tiling as canonical reference point is certainly artificial, and was primarily done for simplicity. We want to briefly cover the implications of moving the reference point to another vertex of the tiling. The most general case of a generic $x_0 \in \mathbb{R}^2$ was not explored.

In particular, we want to point out that some of the nice properties of the tilings introduced in Sections 2.2, 2.3 and 2.4 with respect to determining visibility, are lost in this more general setting.

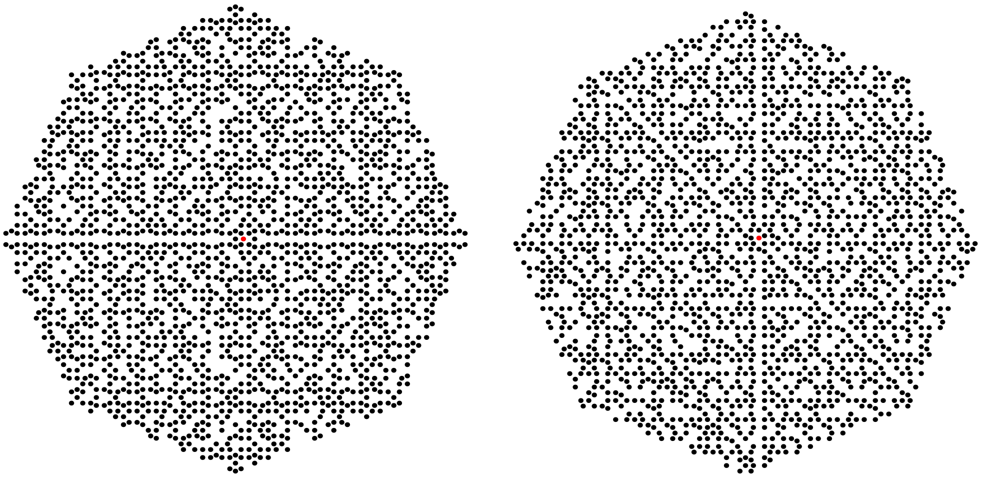

Figure 2.27. Two examples of visible vertices of a D_8 symmetric AB patch (origin) with a non-canonical reference point.

The reference points here are ζ_8^0 and $\zeta_8^0 + \zeta_8^1$, i.e. the two distinct positions which one can move to from the origin in the tiling, see Fig. 2.5, in one step. The origin is indicated in red for both vertex sets.

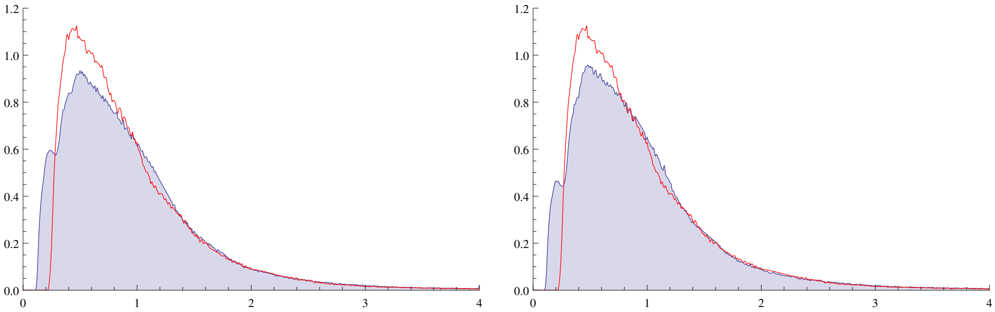

Figure 2.28. Empirical spacing distribution of a D_8 symmetric AB patch with non-canonical reference point.

We can see that the complexity of the bulk depends on the choice of reference point. Once we move away from the origin, plateaux similar to the ones we saw for the TT tiling appear. The following investigation suggests that the canonical configuration, see Fig. 2.6, is indeed special and that the generic case behaves more like the data in Fig. 2.28.

2.10. Averaging

As we have seen above, the spacing distributions depends on our reference point. If we assume that the distribution provides an encoding of the order properties of the initial point set, then all the previous histograms display only a part of this information.

To counter this issue, it is natural to *average* over the different configurations of distributions found in the tiling. We start with a circular patch $\mathcal{P}$ around zero with radius R_0 and choose a subpatch radius $0 < R < R_0$. Now, we select a reference point x from $\mathcal{P}$ at random and check if the subpatch around x with radius R is contained in $\mathcal{P}$. If this is true, we compute the empirical distribution $\nu_{R,x}$ of the subpatch.

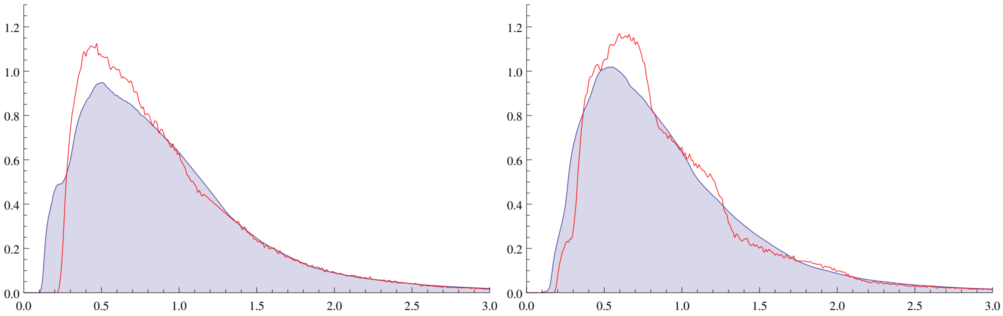

Figure 2.29. Averaged empirical spacing distribution of a AB (left) and TT (right) patch. The graph of the canonical case is overlayed in red.

Let $K \in \mathbb{N}$ and repeat this procedure until we have computed K distributions corresponding to reference points $x_1, \ldots, x_K$ and average, i.e.

$$\nu_R := \frac{1}{K} \sum_{i=1}^{K} \nu_{R,x_i} \, .$$

It appears that, for the AB patch, the configuration with the reference point at the origin is the exception, and the common case are the configurations we have seen in Fig. 2.28. In the case of the TT patch, the averaging does what one would expect from it, namely smoothing out the graph.

Another interesting aspect is the ratio of visible vertices from each reference point.

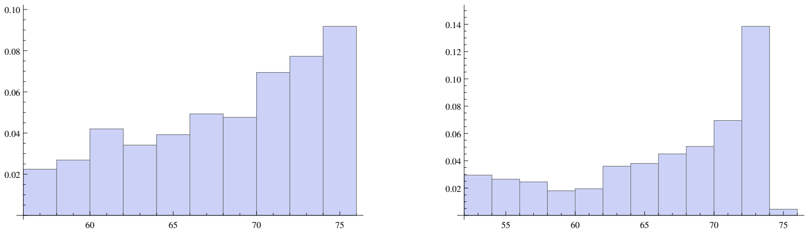

Figure 2.30. Distribution of the percentage of visible vertices for AB (left) and TT (right).

On the x-axis in Fig. 2.30, we have the ratio (in %) of visible vertices to all vertices in the subpatch, and the relative frequency of that ratio on the y-axis. Values for the AB tiling are in the range $[57, 75]$, while we have $[53, 74]$ for the TT tiling, hence more fluctuation in latter case.

Conclusion 2.10
The first results presented in this chapter indicate that the RPM can detect order to some extent. We could observe that the model set cases behave more like the $\mathbb{Z}^2$ lattice, while disorder pushes the radial projection into the direction of the Poisson case. In Chapter 5 we have further explored this, by gradually adding disorder to some of our tilings. Also, we have seen in Section 2.9 that the RPM results are not constant on the hull of a tiling, like other prominent properties, e.g. *FLC* or the frequency of patches, are.
Still, There is much to explore here, like e.g. how the LB tiling behaves for a non-canonical reference point and under averaging. In general, it would be interesting to check how often a given configuration appears during the averaging process, i.e. fix a $\nu_{R,x}$ and count the number of subpatches that produce exactly this empirical distribution. This would give us a better idea how the final result of the averaging is composed.
In the next chapter, we focus on the construction of large patches of the tiling that served as the input of the RPM here.

CHAPTER 3

Construction of tilings

The efficient construction of large patches of a tiling T is a crucial step in computing good approximations of the limit distribution of the radial projection of T. In particular, the involved algorithms should to be fast, conservative in their use of system memory, and numerically stable. In general, we try to avoid the use of floating-point computations and keep all data exactly represented by integers of machine-size.

Remark 3.1
For the construction of the patches we use standard data structures, either managed arrays (`std::vector` from the `C++` standard template library) or double-linked lists (`std::list`). Managed arrays are linear arrays which grow and shrink depending on size requirements. Hence, the complexity of appending a element is constant amortised [1]. The amortisation can be omitted, if the maximum number of elements is known in advance. In this situation, we can preallocate [2] the storage in system memory needed for the array.
In the following, we abbreviate the two structures by *array* and *list*, respectively.

3.1. Cyclotomic model sets

The physical space of a regular model set of cyclotomic type with parameter n is $\mathbb{R}^2$, with L (see Definition 2.5) being the ring of integers $\mathcal{O} = \mathbb{Z}[\zeta_n]$ of a cyclotomic field. We omit the index of the primitive root of unity ζ_n in the following for simplicity. Each $x \in \mathcal{O}$ can be written as

$$x \;=\; \sum_{i=0}^{n-1} \alpha_i \zeta_n^i$$

but this representation is usually not unique. By using the algebraic properties of ζ, one can reduce the above sum to

$$x \;=\; \sum_{i=0}^{\phi(n)-1} \alpha_i \zeta^i \;, \tag{3.1}$$

---

[1] Complexity is constant as long the internal linear array of the `std::vector` is still large enough to fit the elements which are appended.

[2] Allocation is the process of requesting system memory from the operating system (OS). Deallocation means returning such memory back to the OS.

with $\phi(n)$ being the *Euler-Phi* or totient function. With this reduction, the representation becomes unique, because $\mathcal{O}$ is a $\mathbb{Z}$-module of rank $\phi(n)$, with $\mathcal{O} \simeq \mathbb{Z}^{\phi(n)}$ as additive Abelian groups. We are going to work with large arrays of vertices later, so this reduction is convenient because of several features.

1. The representation allows us to encode vertices exactly in our algorithms, as long as the α_i in Eq. (3.1) stay within a certain range.
2. Since $\phi(n) < n$ we use less system memory to store vertices.
3. It ensures that two elements are equal iff the corresponding α_i match, which simplifies the removal of duplicate vertices from the arrays.

Also error estimates during the construction are now superfluous.

Definition 3.2
Let $X := \mathbb{Z}^k$ for some $k \in \mathbb{N}$, and $S \subset X$ with the following properties.

- (a) S is finite and non-empty.
- (b) $0 \notin S$
- (c) $S = -S$ (symmetry)

Let $A_0 := \{0\}$, $A_{-1} := \varnothing$ and recursively define sets $A_i \subseteq X$, $i \geqslant 1$, by

$$A_i \ := \ (A_{i-1} + S) \setminus (A_{i-1} \cup A_{i-2})$$

and denote A_i as the *shell* of index i. The constraint to have $x + s$ neither in A_{i-1} nor in A_{i-2} shall be called level 2 *backtracking*, i.e. we go back two levels in our sequence of shells to construct a new one.

Corollary 3.3
By construction of the shells, we have the following properties.

1. $A_k \subseteq \{\sum_{i=1}^{k} s_i \ : \ s_i \in S\}$ for all $k \in \mathbb{N}$.
   Note that we do not impose any *minimality* on the sum at this point.
2. $A_k \cap A_{k-1} = \varnothing$ for all $k \in \mathbb{N}$.
3. $A_k \cap A_{k-2} = \varnothing$ for all $k \in \mathbb{N}$.

Definition 3.4
Define the S-induced graph distance d_G on X by

$$d_G(x, y) \ := \ \min\{\ell \in \mathbb{N}_0 \ : \ \exists \, (x_i)_i \subset X, \ x_0 = x, \ x_\ell = y, \ x_i - x_{i-1} \in S \, \forall \, i\} \tag{3.2}$$

and sets $B_i \subseteq X$, $i \geqslant 1$, by

$$B_i \ := \ \{x \in X \ : \ d_G(0, x) = i\} \ .$$

We call B_i the *d_G-shell* of index i.

Corollary 3.5
Let $y \in B_k$ for some k and consider a corresponding sequence $(x_i)_i$ in Eq. (3.2). Denote the associated steps $(s_i)_i$ as *path* of y, i.e. the s_i are defined by the

property

$$x_i \;=\; \sum_{j=1}^{i} s_j \; .$$

Hence, this B_k contains the elements of X which can be reached with a minimum of k steps in terms of elements of S. In particular, a path as defined above to an element in B_k is not contractible, i.e. cannot be replaced with a path of shorter length. Two d_G-shells with different indices are therefore disjoint.

Example 3.6
Let us look at the first shells A_i:

(1) $A_0 = \{0\}$
(2) $A_1 = \{x + s,\, x = 0,\; s \in S \;:\; x + s \neq 0\} = S$
(3) $A_2 = \{x + s,\, x \in A_1 = S,\; s \in S \;:\; x + s \notin A_1 = S,\; x + s \notin A_0 = \{0\}\}$
$\quad = \{s_1 + s_2,\; s_i \in S \;:\; s_1 + s_2 \neq 0,\; s_1 + s_2 \neq s \,\forall\, s \in S\}$
(4) $A_3 = \{s_1 + s_2 + s_3 \;:\; s_i \in S,\; s_1 + s_2 \in A_2,\; \sum s_i \notin A_2, \sum_{s_i} \notin A_1\}$

The conditions for a $x \in A_2$ say that a path s_i for x is not contractible. In particular, one can already see here that this property is not easily extracted for the set A_3. Still, it follows that

$$A_i \;=\; B_i \quad \text{for} \quad i \in \{0, 1, 2\} \; ,$$

which is going to serve as the induction basis for a later argument.

Corollary 3.7
One has the following inclusion and intersection properties,

(a) $B_i \subseteq A_i$ for all i;
(b) $A_i \subseteq \bigcup_{j \leqslant i} B_j$ for all i;
(c) $B_i \cap B_j = \varnothing$ for all $i \neq j$.

Theorem 3.8
The recursive and the graph-theoretic shell construction define the same object, i.e. we have

$$\forall\, i \in \mathbb{N} \;:\; A_i \;=\; B_i \; .$$

Proof. We show the statement via induction.
basis: Already given in Example 3.6.
hypothesis: There exists $i \geqslant 2$ such that, for all $j \in \{i-1, i\}$, we have $A_j = B_j$.
step: $i \mapsto i + 1$
We show $A_{i+1} \subseteq B_{i+1}$. If $x \in A_{i+1}$, there exist $y \in A_i$ and $s \in S$ such that $x = y + s$. Using the induction hypothesis and property (a) from Corollary 3.7 we see that $x \in A_i = B_i$.
Next, we rule out that $x \in B_m$ for any $m < i - 1$. Suppose this is the case and

consider $x \in B_m$. Then, x can be written as

$$x \;=\; y+s \;=\; \sum_{k=1}^{m} s_k \quad (s_k \in S)$$

and hence

$$y \;=\; x+(-s) \;=\; \sum_{k=1}^{m} s_k + (-s) \in \bigcup_{j \leq m+1} B_j$$

where we use property (c) of Definition 3.2. But this is a contradiction to $y \in B_i$, since $j \leqslant m+1 < i-1+1 = i$.

So, x can be in either B_{i-1}, B_i or B_{i+1} (exclusively). Using the hypothesis again, we see that $B_i = A_i$ and $B_{i-1} = A_{i-1}$. But by using Corollary 3.3 we know that A_{i+1} has no intersection with either A_i or A_{i-1}. This leaves only $x \in B_{i+1}$ which concludes the proof. ■

Lemma 3.9

For all $k \in \mathbb{N}_1$ and all $j \geqslant 3$, we have

$$x \in A_k \quad \Longrightarrow \quad x \notin A_{k-j}\ .$$

Proof. This follows by using Theorem 3.8 and Corollary 3.5. Since the recursively defined shells match the d_G-shells, which are disjoint, we have

$$A_k \cap A_{k-j} \;=\; \varnothing\ .$$

■

The key ingredient for the recursive construction of the shells is the existence of minimal loops of length two, which is guaranteed by property (c) in Definition 3.2.

Fortunately, we can relax this property and still find a recursive description for the shells.

Definition 3.10

Let X and S be as in Definition 3.2 but omit the symmetry (c). Let $s \in S$ and L a *zero-loop* for s, i.e. there exists $(s_i)_{i=1}^{j} \subseteq S$ such that

$$s + \sum_{i=1}^{j} s_i \;=\; 0\ .$$

Denote by $l(L) = j+1$ the length of the loop. In case the loop context is clear, we just write $L = (s_i)_i$ with $s_0 = s$. For $s \in S$, we define the *minimal zero-loop length* by $\operatorname{mzl}(s) := 0$ in case s has no zero-loops and

$$\operatorname{mzl}(s) \;:=\; \min\{l(L) \;:\; L \text{ is a zero-loop for } s\}$$

otherwise. We further extend mzl to the set S by

$$\operatorname{mzl}(S) \;:=\; \max\{\operatorname{mzl}(s) \;:\; s \in S\}\ .$$

For a symmetric S as defined in Definition 3.2, we have $\mathrm{mzl}(S) = 2$ since $\mathrm{mzl}(s) = 2$ for all $s \in S$.
That the choice to let $\mathrm{mzl}(s) = 0$ if no zero-loop exists makes sense can be seen from the following example.

Example 3.11
Let $S = \{s_0\}$ with $s_0 \neq 0$ be a singleton set. Obviously, s_0 has no zero-loops. Each shell A_j then just contains the element

$$j \cdot s_0 \;=\; \sum_{i=1}^{j} s_0 \;,$$

and for constructing A_{j+1} from A_j no backtracking is needed.

Example 3.12
Let S be a step set with $\mathrm{mzl}(S) = 0$. Since no $s \in S$ has a zero-loop, again no backtracking is needed and each shell is a "convex combination" of the form

$$A_j \;=\; \left\{ \sum_{i=1}^{k} \alpha_i \cdot s_i \;:\; \alpha_i \in \mathbb{N},\; s_i \in S \right\}$$

with $\alpha_1 + \ldots + \alpha_k = j$.

Theorem 3.13
Consider X, S and $\mathrm{mzl}(S)$ as given in Definition 3.10. Then, a recursive definition of the shells A_i is provided by

$$A_i \;:=\; (A_{i-1} \;+\; S) \setminus \bigcup_{j=1}^{\mathrm{mzl}(S)} A_{i-j+1} \;,$$

i.e. backtracking needs to be done up to $\mathrm{mzl}(S)$ levels.

Proof. For the trivial case $\mathrm{mzl}(S) = 0$, we refer to Example 3.12. Now, let $C := \mathrm{mzl}(S) - 1$. We can just copy the proof of Theorem 3.8 and modify the induction hypothesis to

$$\exists\, i > C \quad \forall\, j \in \{i - C, \ldots, i\} \;:\; A_j = B_j$$

and the part where $x \in B_m$ is considered. In this case we have $m < i - C$. Again, we can write

$$x \;=\; y + s \;=\; \sum_{k=1}^{m} s_k,\; y \in A_i = B_i,\; s \in S$$

and hence

$$y \;=\; x + \text{"}(-s)\text{"} \;=\; \sum_{k=1}^{m} s_k + \sum_{k=1}^{j} s'_i$$

for $L = (s'_i)_{i=1}^{j}$ the smallest zero-loop for s. Note that we purposely put the $(-s)$ in quotes to indicate this it does not exist as an element in S. Since $j \leqslant C$, we have

$$y \in \bigcup_{j \leqslant m+C} B_j$$

in the worst case. Since $y \in B_i$ and $j \leqslant m + C < i - C + C = i$, we have a contradiction. Consequently, x can only be an element from $\bigcup_{j=i-C}^{i+1} B_j$, but from the induction hypothesis we know that $x \notin \bigcup_{j=i-C}^{i} B_j$, hence $x \in B_{i+1}$. ■

Remark 3.14

All three cyclotomic cases $n = 8, 10, 12$ use $\mathbb{Z}^4$ as underlying group, i.e. $X = \mathbb{Z}^4$ in Definition 3.2. Denote by e_i the four standard basis vectors. Then, the step sets are given by

$$\begin{aligned} S &= \{\pm e_i \,:\, 1 \leqslant i \leqslant 4\} \quad \text{for } n = 8 \\ S &= \{\pm e_i \,:\, 1 \leqslant i \leqslant 4\} \cup \{\pm \sum_{k=1}^{4} e_k\} \quad \text{for } n = 10 \\ S &= \{\pm e_i \,:\, 1 \leqslant i \leqslant 4\} \cup \{\pm(-e_1 + e_3),\ \pm(-e_2 + e_4)\} \quad \text{for } n = 12\ , \end{aligned}$$

where one can see that, for $n = 12$, also loops of length 3 can occur, e.g. by joining e_1, $-e_3$ and $(-e_1 + e_3)$.

Remark 3.15

We have seen that for S a symmetric step set we only need backtracking up to 2 levels when constructing our shells. We want to point out that for the AB tiling we can do slightly better. Define

$$n(x) \;:=\; \sum_{i=1}^{4} x_i$$

on X. Then, we obviously have $n(x) + n(y) = n(x + y)$ for all $x, y \in X$ and $|n(s)| = 1$ for all $s \in S$.

When we compute $n(x)$ for the first shells

$$\begin{aligned} n(x) &= 0 && \text{for} \quad x \in A_0 \\ n(x) &\in \{\pm 1\} && \text{for} \quad x \in A_1 \\ n(x) &\in \{\pm 2, 0\} && \text{for} \quad x \in A_2 \\ n(x) &\in \{\pm 3, \pm 1\} && \text{for} \quad x \in A_3 \\ n(x) &\in \{\pm 4, \pm 2, 0\} && \text{for} \quad x \in A_4 \end{aligned}$$

we see that two adjacent shells always have elements with different parity, so with $x \in A_i$ and $y \in A_{i+1}$ one has

$$(-1)^{n(x)} \;\neq\; (-1)^{n(y)}\ .$$

In particular, this enables us to drop one level of backtracking, wherefore we can define the shells simply by

$$A_i \;:=\; (A_{i-1} + S) \setminus A_{i-2}\ ,$$

since $x + s \in A_{i-1}$ cannot happen due to the observed change of parity when moving from one shell to the next.
In general, this property does not hold, as one can see from the TT and the GS tiling. Here, both types of parity can occur in the same shell.

By using Theorem 3.8, we can now detail an efficient algorithm for constructing patches of a cyclotomic model set. Choose some parameter n. Then, our underlying set of the construction becomes $X := \mathbb{Z}^m$ with $m = \phi(n)$. If f is the bijection which maps from $\mathcal{O}$ to $\mathbb{Z}^m$, $\{f(\pm\zeta^i) : i\}$ is our set of steps S. Hence, the construction step only uses integer arithmetic so far.

Remark 3.16
To determine whether an element $x \in \mathcal{O}$ is part of the model set, we still need to check whether $x^\star \in W$ holds. For our setting, the star map is a linear map g_T from $\mathbb{Z}^m$ to $\mathbb{Z}^m$, followed by some "evaluation" map e_T giving us a value in $\mathbb{R}^k$ (usually $k = 2$), see the right side of Fig. 2.1. In our standard basis, the $\star$-maps are represented by the matrices

$$g_{\mathsf{AB}} := \begin{pmatrix} 1 & 0 & 0 & 0 \\ 0 & 0 & 0 & 1 \\ 0 & 0 & -1 & 0 \\ 0 & 1 & 0 & 0 \end{pmatrix}, \quad g_{\mathsf{TT}} := \begin{pmatrix} 1 & 0 & -1 & 0 \\ 0 & 0 & -1 & 1 \\ 0 & 1 & -1 & 0 \\ 0 & 0 & -1 & 0 \end{pmatrix}, \quad g_{\mathsf{GS}} := \begin{pmatrix} 1 & 0 & 1 & 0 \\ 0 & -1 & 0 & 0 \\ 0 & 0 & -1 & 0 \\ 0 & 1 & 0 & 1 \end{pmatrix}.$$

The evaluation map has to be treated with care. Once applied, we leave the realm of exactly encoded coordinates. We now have to ascertain that the numerical precision after evaluation is high enough to properly discern whether $x^\star$ is inside or outside the window. As pointed out in Section 2.3, singular configurations make this particularly difficult. Also note that the e_T encode the projection basis; see Definition 2.5.

$$\begin{aligned} e_{\mathsf{AB}} &:= \frac{1}{2} \cdot \begin{pmatrix} \sqrt{2} & 1 & 0 & -1 \\ 0 & 1 & \sqrt{2} & 1 \end{pmatrix} \\ e_{\mathsf{TT}} &:= \frac{1}{2} \cdot \begin{pmatrix} 2 & -\tau' & -\tau & -\tau \\ 0 & \sqrt{\tau+2} & \sqrt{\tau'+2} & -\sqrt{\tau'+2} \end{pmatrix} \\ e_{\mathsf{GS}} &:= \frac{1}{2} \cdot \begin{pmatrix} 2 & \sqrt{3} & 1 & 0 \\ 0 & 1 & \sqrt{3} & 2 \end{pmatrix} \end{aligned}$$

For the choice of the evaluation maps, see [5, Ex. 3.6].

Remark 3.17
We have stated that, in the case of a symmetric step set S, we have level 2 backtracking, i.e. we need to consider the last two shells when constructing the next one.
However, when implementing the construction as an algorithm, we need one additional (working) shell. Each shell is implemented as an array and therefore can contain the same element more than once. Hence, we also need to keep track

of the shell that is currently constructed, so that we do not append vertices twice.

Let us now describe the construction algorithmically.

Procedure 3.18
The construction algorithm takes three input parameters. steps defines after which shell index the algorithm terminates, init is the initial element in A_0, and window a subset of $\mathbb{R}^2$. In all cases considered, we have init $= 0$ and window is a simple geometric shape (n-gon or circle). The output is another array of vertices. Whenever some element of $\mathcal{O}$ is used in the following code, we mean the corresponding coordinatisation in X on the level of the actual implementation.

```
input  : steps, init, window
output : vertexarray
vertexarray ← {init};
for s ← 1 to steps do
    foreach p ∈ vertexarray do
        for $k$ ← 0 to $n-1$ do
            pp ← p + $\zeta_n^k$;
            if pp ∈ vertexarray then
                skip;
            if pp$^\star$ ∉ window then
                skip;
            add pp to vertexarray;
        end
    end
end
```

Algorithm 1: Patch generation for the cyclotomic case.

With our knowledge from Lemma 3.9, we can optimise the check pp $\in$ vertexarray by partitioning the array into two parts. One is the head section consisting of the last 3 shells, and the other part is the tail section which consists of all other "past" shells. With this, our algorithm only has to look into the head section to determine whether a vertex is already present in the array.
Another easy but efficient optimisation is to apply lexicographic ordering inside each shell. Let $x, y \in A_i$ for some shell A_i. Then,

$$x = (x_1, \dots, x_k) \quad \text{and} \quad y = (y_1, \dots, y_k) \, ,$$

and we say that $x < y$ iff $x_i < y_i$ for the first i where x_i and y_i do not match. Consider the case that A_i is currently being constructed and that x is a potential candidate to be appended, i.e. it is not yet part of the array. In the likely case that $x \notin A_{i-1}$ and $x \notin A_{i-2}$, we would still have to iterate over all entries of A_{i-1} and A_{i-2} to confirm this. The lexicographic order ensures that we usually

only iterate over a small amount of elements.
Of course, sorting the shell consumes processing time as well, but all our measurements have shown that the time spent sorting is amortised by the reduction of time spent searching. The sorting process is done once after the shell construction is finished.

Remark 3.19
The code in Algorithm 1, except for the check $\mathsf{pp}^\star \notin \mathsf{window}$, relies only on integer arithmetic. Under the assumption that no integer under- or overflow occurs, the computation is exact at this point.
For the window check, we apply the following procedure. Since the window W is a centred n-gon in $\mathbb{R}^2$ with some potential shift s, i.e. $W = W_0 + s$ (W_0 centred), we can accept/discard most vertices by testing against the inner radius R_{inner} or outer radius R_{outer} of W_0, respectively.

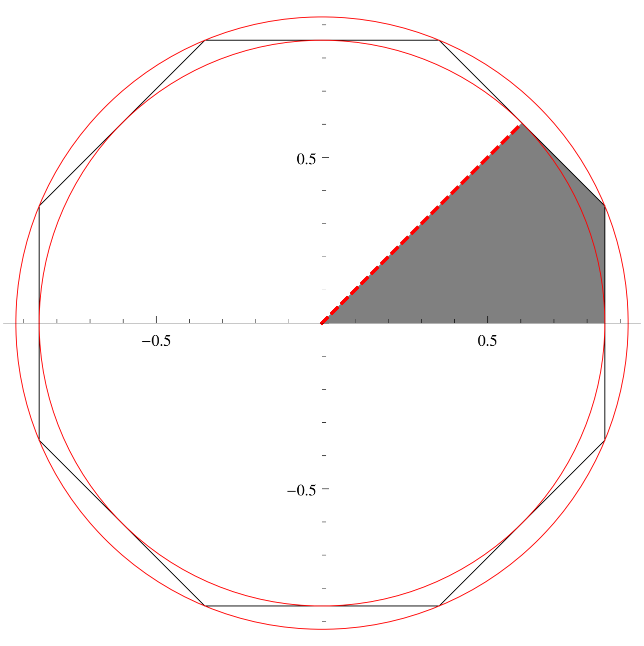

Figure 3.1. Window check for the AB tiling where we test against a regular octagon.

Consider $y := x^\star \in \mathbb{R}^2$ in internal space. If both conditions $\|y\| \leqslant R_{\mathsf{inner}}$ and $\|y\| > R_{\mathsf{outer}}$ fail, then y is contained in the area enclosed by the two red circles in Fig. 3.1. Write $y = (a, b)$ and use the symmetry of W_0 to transform y into the grey area, i.e. $y' := (|a|, |b|)$ if $|a| \leqslant |b|$.
At this point, we just need to check y' against two lines. If $(v_i)_{i\geqslant 0}$ are the vertices of W_0 in counter-clockwise order (v_1 the vertex in the grey area), then $\overline{v_0 v_1}$ and $\overline{v_1 v_2}$ are the corresponding lines. Consider (a_0, b_0), (a_1, b_1) and (a_2, b_2). Then,

the sign of

$$\epsilon \;:=\; (a_1 - a_0) \cdot (b_2 - b_0) - (b_1 - b_0) \cdot (a_2 - a_0)$$

tells us on which side of the line $\overline{(a_0, b_0)(a_1, b_1)}$ the vertex (a_2, b_2) is located ($\epsilon = 0$ if it is located on the line).
The implementation of the window checks for the other tilings works analogously. Computations on this level were done with double precision *IEEE 754* [31] floating point numbers. One has to be careful when working with singular model sets, i.e. model sets where the situation $x^\star \in \partial W$ occurs. In this case, the sign test above becomes unstable and one has to derive a separate test to identify singular vertices.

Remark 3.20
In Remark 3.1, we mentioned that the computational complexity of appending operations for managed arrays is constant, as long as the internal storage does not need to grow. For this reason, it is desirable to know the final number of vertices in Procedure 3.18 in advance.
Another reason is the randomisation explained in Chapter 5. There we discard a certain percentage p of the vertices before applying RPM to the patch. Still we always want to have roughly the same amount data to compare the RPM results for different p. Hence, if we fix the number of vertices N, we have to estimate steps, such that Procedure 3.18 outputs N vertices. We constructed an estimator by applying the following steps.
Fix a tiling T, a sample count $k \in \mathbb{N}$, and a sample width $d \in \mathbb{N}$. Now run our procedure with $\mathsf{steps} = i \cdot d$ for each $1 \leqslant i \leqslant k$ and record the number of vertices N_i. A least squares fit of the sequence $(N_i)_i$ with a quadratic polynomial $p(x) = a_2 \cdot x^2 + a_1 \cdot x$ gives us a map $\mathsf{steps} \to N$. Since p is quadratic, we can simply invert the map, giving us an estimator for the tiling T. We write the estimator as

$$q(x) \;=\; b_0 \cdot (b_1 + \sqrt{b_2 + b_3 \cdot x})$$

with the coefficient from Table 3.1.

Table 3.1. Coefficients for the $N \to \mathsf{steps}$ estimator.

tiling	b_0	b_1	b_2	b_3
AB	0.213296	−2.23594	4.99944	9.37663
TT	0.117292	−5.94039	35.2883	17.0515
GS	0.051852	−10.6339	113.08	38.5713
RP	0.209245	−2.00585	4.02342	9.55819

3.2. Inflation tilings

For the construction of patches of inflation based tiling, we first have to consider how to encode all the tiles that appear. We start with the planar chair tiling; see Section 2.7 as an example.

Example 3.21
The planar `chair` tiling uses L-shaped tiles in four orientations.

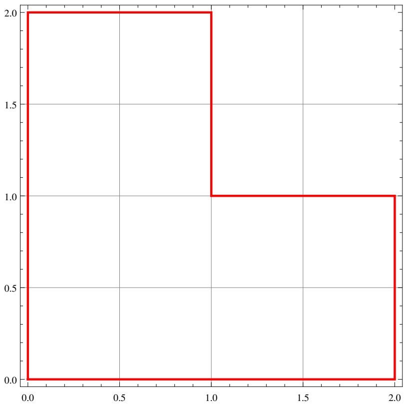

Figure 3.2. A single tile of the `chair` tiling embedded in $\mathbb{Z}^2 \subset \mathbb{R}^2$.

If we choose the reference point $p \in \mathbb{Z}^2$ to be the coordinate of the left-bottom vertex of the tile, we can encode each tile as pair (p, r), with $r \in \mathbb{Z}/4\mathbb{Z}$ the rotation around p. The initial patch with D_4 symmetry is then encoded as the set

$$\{(0', 0),\ (0', 1),\ (0', 2),\ (0', 3)\}\ ,$$

where $0' = 0_{\mathbb{Z}^2}$. If we have a pair (p, r), we can recover the vertices of the corresponding tile via

$$\{p\} \cup \{p + R(r, v_i)\ :\ 1 \leqslant i \leqslant 5\}$$

with

$$v_1 := (2, 0),\ v_2 := (2, 1),\ v_3 := (1, 1),\ v_4 := (1, 2),\ v_5 := (0, 2)$$

and the rotation map

$$R(r, v)\ :=\ \begin{pmatrix} 0 & -1 \\ 1 & 0 \end{pmatrix}^r \cdot v\ .$$

If the vertices are created in the order given above, the edges of the tile can be reconstructed by connecting consecutive vertices, i.e. we connect p with $p + R(r, v_1)$, $p + R(r, v_1)$ with $p + R(r, v_2)$ and so on.
We have already seen in Fig. 2.20 that each tile produces four tiles after applying an inflation step. We again start with a tile (p_0, r_0) and denote the result after the inflation as

$$\{(p_i, r_i)\ :\ 1 \leqslant i \leqslant 4\}\ .$$

First, take the rescaling by a factor of 2 into account. Let $p' = p_0 \cdot 2$. Then, we can write the rotation parameters as

$$r_1 \coloneqq r_0,\ r_2 \coloneqq r_0,\ r_3 \coloneqq r_0 + 1,\ r_4 \coloneqq r_0 + 3$$

and the new reference points as

$$p_1 \coloneqq p',\ p_i \coloneqq p' + R(w_{i-1}, r_0),\ \text{for } 2 \leqslant i \leqslant 4\ .$$

Here, we have $w_1 \coloneqq (1, 1)$, $w_2 \coloneqq (4, 0)$ and $w_3 \coloneqq (0, 4)$.
The important property here is that the parameters of a tile can be stored exactly. In particular, this is due to the tile only appearing with a finite number of possible rotations. We can encode the rotation parameter with just 2 bits here. For the encoding of the reference point, we have to consider some bound on the number of inflation steps.
If we use the D_4-symmetric arrangement of 4 tiles as our initial patch, 13 inflations usually yields enough data for our calculations. Going one step further, using 14 inflation, we see that the coordinates $p = (x, y)$ are bounded by 23172, i.e. $|x|, |y| \leqslant 23172$. Hence, we can encode both x and y with signed short types (signed short uses 2 bytes storage and can represented the integer range $[-32768, 32767]$).
If we use an unsigned long (4 bytes storage) for the rotation, the entire tile consumes 8 bytes, which is then also nicely aligned to 4 bytes, another property chosen for performance reasons.

Remark 3.22
If we start the inflation of the planar chair tiling from the initial arrangement as given in Example 3.21, we end up with a patch the shape of a "plus". Hence, the patch is not suitable if we want to use it as input for radial projection.
Assume that we apply k inflations. Then, we have to intersect the resulting patch with a disc of radius $\sqrt{2} \cdot 2^k$ to recover a patch with circular shape. On the level of tiles, we discard a large percentage of them. But we can do better in this case. First of all, we can just use the single tile from Fig. 3.2 as initial arrangement to avoid redundancy from the D_4 symmetry. Next, we apply some clipping after each inflation iteration, to discard tiles which do not contribute to our final circular patch. Assume that we have currently applied inflation step i of a total of k steps. Denote by T_i the set of tiles produces by step i. We remove every $t \in T_i$ where all vertices of t are outside the ball of radius $\sqrt{2} \cdot 2^i$. This way, we reduce the number of tiles by dropping those which would be discarded later anyway.

Example 3.23
Another tiling which admits an exact encoding of its tiles, similar to the encoding of the planar chair tiling, is the chiral LB tiling.

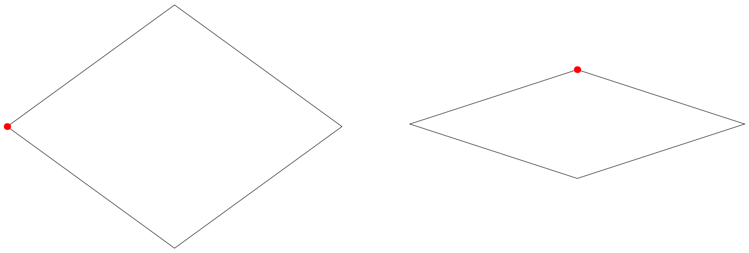

Figure 3.3. The two prototiles of the LB tiling. The reference point is indicated in red.

Essentially, we can proceed as in Example 3.21. This time, we have two types of tiles, the thick rhombus (type A) and the thin rhombus (type B). We know that the vertices of the tiling live in $\mathbb{Z}[\zeta_5] = \mathbb{Z}[\zeta_{10}]$, but for the construction step we choose to move to $X := \mathbb{Z}[\zeta_{20}]$, for reasons that will become clear in a moment. Hence, the encoded tile can be written as (t, p, r) where $t \in \{\mathsf{A}, \mathsf{B}\}$, $p \in X$ is the reference point (see Fig. 3.3) and $r \in \mathbb{Z}/20\mathbb{Z}$ is the rotation of the tile around p. Since $\phi(20) = 8$, we coordinatise p as element in $\mathbb{Z}^8$.
The initial patch with C_5 symmetry is then encoded as follows.

$$\{(\mathsf{A}, \zeta^7{+}\zeta^3, 15),\ (\mathsf{A}, \zeta^7{+}\zeta^{11}, 19),\ (\mathsf{A}, \zeta^{11}{+}\zeta^{15}, 3),\ (\mathsf{A}, \zeta^{15}{+}\zeta^{19}, 7),\ (\mathsf{A}, \zeta^{19}{+}\zeta^3, 11)\}$$

We define $\zeta := \zeta_{20}$ for the time being. The vertices for a tile (t, p, r) can be recovered via

$$\{p\} \cup \{p + R(r, \zeta^{18}),\ p + R(r, \zeta^{18} + \zeta^2),\ p + R(r, \zeta^2)\}$$

for $t = \mathsf{A}$, and

$$\{p\} \cup \{p + R(r, \zeta^{11}),\ p + R(r, \zeta^{11} + \zeta^{19}),\ p + R(r, \zeta^{19})\}$$

for $t = \mathsf{B}$. Here, R is again a rotation map, this time given by $R(r, v) := \zeta^r \cdot v$. Inflation of a tile (t_0, p_0, r_0) results in the set

$$\{(\mathsf{A}, p', r + 1),\ (\mathsf{A}, p', r + 9),\ (\mathsf{A}, p', r + 5),\ (\mathsf{B}, p', r)\}$$

for $t_0 = \mathsf{A}$, and

$$\{(\mathsf{A}, p', r + 10),\ (\mathsf{B}, p', r + 9),\ (\mathsf{B}, p', r + 1)\}$$

for $t_0 = \mathsf{B}$. The new reference point p' is computed as follows,

$$p' = \begin{cases} r \cdot \lambda + R(r, \zeta^1 + \zeta^{17}) & : \ t = \mathsf{A}\ , \\ r \cdot \lambda + R(r, \zeta^{18} + \zeta^{10}) & : \ t = \mathsf{B}\ . \end{cases}$$

Here, $\lambda = \sqrt{(5 + \sqrt{5})/2}$ is the inflation multiplier of the tiling. In terms of coordinates in X, we can write $\lambda = \zeta + \zeta^{-1}$, so multiplication with λ is, like applying R, again a linear map on $\mathbb{Z}^8$.

Assume that we have just constructed a patch of the tiling. Let $x \in X$ be any vertex of the tiling, and write

$$x \;=\; \sum_{k=0}^{19} \alpha_k \zeta^k \,.$$

Then, we either have $\alpha_k = 0$ for all even k, or for all odd k, which only depends on the parity of the number of inflation steps. In the case that all even coordinates vanish, we have

$$x \;=\; \sum_{k=0}^{9} \alpha_{2k} \zeta^{2k} \,.$$

Since $\zeta^2 = \zeta_{10}$, every vertex $x \in X$ is already an element of $\mathbb{Z}[\zeta_5]$. In the other case, where all odd coordinates vanish, we have $x = \zeta \cdot x'$ for some $x' \in \mathbb{Z}[\zeta_5]$. Hence, up to some constant rotation of 18 degree, all vertices are again in $\mathbb{Z}[\zeta_5]$. Once the tiling is constructed, we can therefore apply some "reduction" when collecting the vertices of the tiles.

For the tile encoding this means the following. The type and the rotation parameter both use an unsigned short. Each coordinate of X uses a signed short, which results in $2 \cdot 2 + 8 \cdot 2 = 20$ bytes for each tile. For the vertex collection step, we just need $4 \cdot 2 = 8$ bytes for each vertex.

Remark 3.24

The pinwheel tiling is an example where none of the constructions explained so far applies. Even though it uses just one prototile, a triangle with sidelenghts $\{1, 2, \sqrt{5}\}$, the tile appears in infinitely many rotated versions; see [5, Ch. 6.6]. Hence, it is not possible to encode a tile using the reference point together with an angle from a finite list.

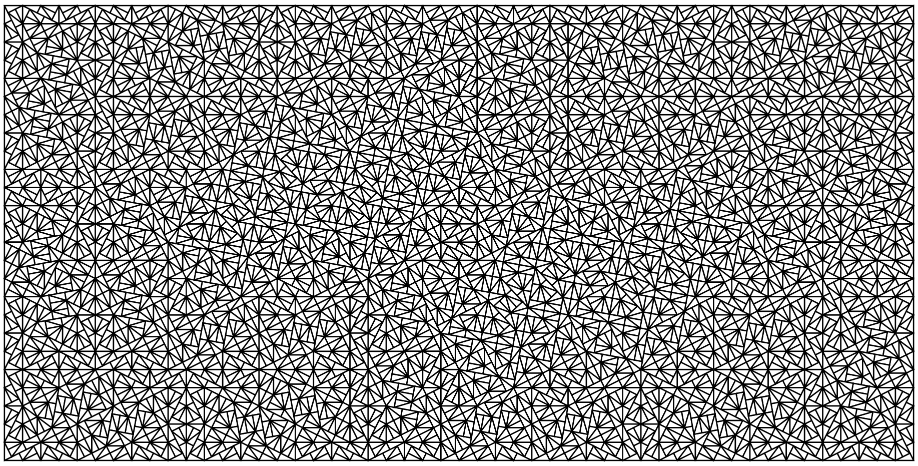

Figure 3.4. Rectangular patch of the pinwheel tiling.

Still, it would be possible to encode a tile exactly by storing all three vertices of the triangle, which are known to have rational coordinates, see [46]. As long as the coordinate $\frac{p}{q}$ has "small" p and q, we can store the numerator and denominator again as integer with machine-size. However, initial tests have shown that this is not the case. Both p and q grow quickly with each inflation iteration, making it necessary to use an arithmetic bignum library (like the GMP, see [25]) to store the coordinates. A compromise would be to use a floating-point representation of the coordinates, but then the question of the error introduced by each inflation step arises. Since small changes to coordinates heavily influence the visibility property of a vertex, we have refrained from pursuing this approach. Also, the logarithmic growth behaviour of tiling poses a problem here.

However, since the diffraction of the pinwheel displays S_∞ symmetry, it would certainly be interesting to check how this property translates to radial projection.

Remark 3.25

The *de Bruijn* method [12] via dualisation of a grid provides an alternative approach for constructing tilings with n-fold rotational symmetry. We considered this approach, in particular because the construction is generic, but abandoned it again because of the following difficulty.

Take ζ a primitive root of unity (compare Remark 2.2), and $\gamma \in \mathbb{R}$ some displacement $d \in \mathbb{R}$, then the corresponding grid in $\mathbb{R}^2 \simeq \mathbb{C}$ is defined as

$$\mathcal{G}(\zeta, d) \;:=\; \{z \in \mathbb{C} \;:\; \Re(z\zeta^{-1}) + d \in \mathbb{Z}\} \;.$$

Given displacement values $d_1, \ldots, d_n$ the n-grid is then just the union of the $\mathcal{G}(\zeta^i, d_i)$. For the numerical implementation however, we can only work with finite grids. If we start with a finite configuration of grids, symmetric around the origin, the resulting tiling is going to be symmetric as well, but comes with a "corona" of defects. Computing an appropriate cut-off radius (depending on the size of the grids) to remove this corona proved to be difficult.

Another issue was that the input n-grid had to be regular (see [5, Ch. 7.5.2]) for the dualisation procedure to work.

Conclusion 3.26

The detailed numerical analysis of the radial projection requires large circular patches of the tiling. On the one hand, we have seen that tilings described by a cyclotomic model set provide a natural way of efficiently constructing such patches. On the other hand, inflation tilings require custom construction algorithms that have to be derived by looking at the individual inflation rules. Another difficulty that arises with the latter case, is that control over the patch size is quantised with respect to the number of inflation steps. The former case allows more precise control by changing the number of shells. We tried to improve the size control for inflation tilings by introducing tile discarding between the inflation steps, but did not pursue this strategy further after getting mixed results.

So, after having established the algorithms to create our patches, we still need to isolate the visible vertices. We discuss this topic in the next chapter.

CHAPTER 4

Determining visibility of tiling vertices

For every point set X that we plug into the radial projection procedure, we are only interested in the subset of the visible points of X. As we have seen with the integer lattice case in Section 1.2, studying this subset is crucial in understanding the resulting limit distribution. While an arbitrary X will not admit a nice description of the subset, we have already come across some positive examples.

4.1. Simple cyclotomic model sets

Definition 4.1
Let $X \subseteq \mathbb{R}^2$ be the set of tiling vertices and fix a reference point $x_0 \in \mathbb{R}^2$. Let $x \in X$ and consider the (open) connecting line $\mathfrak{L}(x)$ between x and x_0, i.e.

$$\mathfrak{L}(x) \;\coloneqq\; \{x_0 + \lambda \cdot (x - x_0) \;:\; \lambda \in (0,1)\}\ .$$

We say that x is *visible* from x_0 when $\mathfrak{L}(x) \cap X$ is empty, i.e. nothing is blocking the "view" from x_0 to x, and denote this as the *geometric visibility* property. Since we can always move X, we assume w.l.o.g. that $x_0 = 0$. The condition then simplifies to

$$\forall\, \lambda \in (0,1) \;:\; \lambda \cdot x \notin X,$$

which is the version which we are going to use primarily.

4.1.1. Ammann–Beenker and Tübingen triangle.

Definition 4.2 (Notation for underlying sets)
Let $n \in \mathbb{N}_{\geqslant 2}$ and $\zeta \coloneqq \zeta_n \coloneqq \exp(2\pi \mathrm{i}/n) \in \mathbb{C}$ a primitive n-th root of unity. We use the following notation; see [49] for general background.

1. $\mathbb{K} = \mathbb{Q}(\zeta)$ for the cyclotomic field with parameter n.
2. $\Bbbk = \mathbb{Q}(\zeta + \bar{\zeta})$ for the maximal real subfield of $\mathbb{K}$ ($\bar{z}$ denotes the complex conjugate of z).
3. $\mathcal{O} = \mathbb{Z}[\zeta]$ for the cyclotomic ring of integers.
4. $\mathfrak{o} = \mathbb{Z}[\zeta + \bar{\zeta}]$ for the ring of integers of $\Bbbk$. Here, $\mathfrak{o}$ is the maximal real subring of $\mathcal{O}$.
5. When $\Bbbk$ is a quadratic field, we use ϵ to denote a fundamental unit of $\mathfrak{o}$.

We have already seen in Section 3.1 how to coordinatise $\mathcal{O}$, but the same can also be done with $\mathfrak{o}$. We prefer to have an ϵ with small entries in the coordinatisation.

From this point onwards, we assume that n in Definition 4.2 is chosen such that $\Bbbk$ is a quadratic field. In addition to the sets defined above, we need some more tools.

Definition 4.3 (Algebraic tools)
Consider the algebraic norm of $\mathfrak{o}$ and denote it by $\mathrm{N}\colon \mathfrak{o} \to \mathbb{Z}$. Let $\mathfrak{o}^\times$ be the group of units of $\mathfrak{o}$. Then, we have

$$\alpha \in \mathfrak{o}^\times \quad \Longleftrightarrow \quad |\mathrm{N}(\alpha)| = 1 \; .$$

We further write x' for the algebraic conjugate of an element $x \in \mathfrak{o}$, which is unique since $\Bbbk$ is quadratic. By some coordinate transformation, we can always write $\mathcal{O}$ as the direct sum

$$\mathcal{O} \;=\; \mathfrak{o}\cdot 1 \oplus \mathfrak{o}\cdot\zeta, \quad \mathcal{O} \ni x \;=\; x_1 + x_2\cdot\zeta,\; x_i \in \mathfrak{o} \tag{4.1}$$

and, under the condition that $\mathcal{O}$ is a GCD domain (GCD domains are a subset of *unique factorisation* domains), define the *greatest common divisor* of x by

$$\gcd(x) \;\coloneqq\; \gcd_{\mathfrak{o}}(x_1, x_2) \; ,$$

where $\gcd_{\mathfrak{o}}$ is the GCD of two elements of $\mathfrak{o}$. In fact, for all considered cases, $\mathcal{O}$ is a Euclidean domain, which provides us with an efficient algorithm to compute the GCD. Since the direct-sum decomposition in Eq. (4.1) is unique, the GCD for an element of $\mathcal{O}$ is well-defined up to units of $\mathfrak{o}$.

Remark 4.4
For $n = 8$, we have $\Bbbk = \mathbb{Q}(\sqrt{2})$, $\mathfrak{o} = \mathbb{Z}[\sqrt{2}]$ and $\epsilon = 1 + \sqrt{2}$. An element $a + b\cdot\sqrt{2}$ from $\mathfrak{o}$ has the algebraic conjugate $a - b\cdot\sqrt{2}$, and the algebraic norm N of $\mathfrak{o}$ is given by

$$x \;=\; a + b\cdot\sqrt{2} \quad\longmapsto\quad \mathrm{N}(x) \;=\; x\cdot x' \;=\; a^2 - 2b^2 \; .$$

The group of units can be explicitly written as

$$\mathfrak{o}^\times \;=\; \{\pm\epsilon^k \;:\; k \in \mathbb{Z}\} \tag{4.2}$$

For $n = 10$, we have $\Bbbk = \mathbb{Q}(\tau)$, $\mathfrak{o} = \mathbb{Z}[\tau]$ and $\epsilon = \tau$ with τ the golden ratio, i.e.

$$\tau \;=\; \frac{1+\sqrt{5}}{2} \; ,$$

with $\tau' = (1-\sqrt{5})/2 = -1/\tau$ its conjugate. The norm is given by

$$x \;=\; a + b\cdot\tau \quad\longmapsto\quad \mathrm{N}(x) \;=\; x\cdot x' \;=\; a^2 + ab - b^2$$

with $x' = a + b\cdot\tau'$ the conjugate of x. The group of units is of the same form as in Eq. (4.2), i.e.

$$\mathfrak{o}^\times \;=\; \{\pm\tau^k \;:\; k \in \mathbb{Z}\} \; .$$

Definition 4.5
Let $z \in \mathcal{O}$ be non-zero. We call z *strongly* $\mathfrak{o}$-primitive when

$$\forall\, \kappa \in \Bbbk \;:\; (\kappa z \in \mathcal{O} \implies \kappa \in \mathfrak{o}) \tag{4.3}$$

holds. We call z *weakly* $\mathfrak{o}$-primitive when

$$\forall\, \kappa \in \mathfrak{o} \;:\; \big(z \in \kappa\mathcal{O} \implies \kappa \in \mathfrak{o}^{\times}\big) \tag{4.4}$$

holds. The last version of primitivity is defined by using the GCD. We call x gcd-primitive (or simply *coprime*) when

$$\gcd(z) \in \mathfrak{o}^{\times} \;.$$

Note that even though the GCD is not unique (so rather we talk about *a* GCD), this does not pose any difficulty here since all GCDs can be transformed into one another by multiplication with a unit from $\mathfrak{o}$.

A more natural approach would use ideals. In view of our later implementation, we prefer to stay on the level of numbers, and then deal with the units separately.

Remark 4.6
If we consider elements of $\mathbb{k}$ to be *scalars*, then Eqs. 4.3 and 4.4 can also be interpreted in the following way.
The strong property says that scaled copies of z can only be again cyclotomic integers if the scalar already was an integer. By writing the weak condition as

$$\forall\, 0 \neq \kappa \in \mathfrak{o} \;:\; \big(\kappa^{-1} z \in \mathcal{O} \quad\implies\quad \kappa^{-1} \in \mathfrak{o}\big)\,,$$

where we consider κ^{-1} to be the inverse in $\mathbb{k}$, we see that only scalars of the type κ^{-1}, $\kappa \in \mathfrak{o}$, play are role here. Since $\{\kappa^{-1} : 0 \neq \kappa \in \mathfrak{o}\}$ is a proper subset of $\mathbb{k}$, this condition is the "weak" version.
The main reason to also take gcd-primitivity into account is for implementation purpose. All considered cases allow computation of the GCD via the Euclidean algorithm, which in turn relies on a *modulo* operation in the corresponding (real) ring of integers. Strong and weak primitivity are the notions used for the theoretical part.

Theorem 4.7
For $n \in \{8, 10\}$, all three types of primitivity from Definition 4.5 are equivalent.

Proof. We first show that strong primitivity and gcd-primitivity are equivalent. We begin by reformulating strong primitivity.
For this, let $z \in \mathcal{O}$ and write z as $\alpha + \beta \cdot \zeta$ with $\alpha, \beta \in \mathfrak{o}$. Let $\kappa \in \mathbb{k}$. Then, we have

$$\kappa z \;=\; \kappa\alpha + \kappa\beta \cdot \zeta \;,$$

so if $\kappa z \in \mathcal{O}$ then $\kappa\alpha$ and $\kappa\beta$ have to be the coefficients in the $\mathfrak{o} \cdot 1 \oplus \mathfrak{o} \cdot \zeta$ decomposition and are therefore again unique. Since $\kappa\alpha \in \mathfrak{o}$ and $\kappa\beta \in \mathfrak{o}$, we can reformulate the strong primitivity as

$$\kappa\alpha \in \mathfrak{o} \,\wedge\, \kappa\beta \in \mathfrak{o} \quad\implies\quad \kappa \in \mathfrak{o}\;.$$

Proceed by writing κ as $\kappa = \tau_0/\tau_1$ with $\tau_0, \tau_1 \in \mathfrak{o}$ coprime elements, i.e. the fraction is maximally reduced up to units. The primitivity condition then reads

$$\frac{\tau_0}{\tau_1}\alpha \in \mathfrak{o} \;\wedge\; \frac{\tau_0}{\tau_1}\beta \in \mathfrak{o} \quad \Longrightarrow \quad \tau_1 \in \mathfrak{o}^\times \,.$$

strong $\Rightarrow$ gcd:
Let g be a GCD of α, β and choose $\Bbbk \ni \kappa := \frac{1}{g}$ ($\tau_0 = 1$ and $\tau_1 = g$). But

$$\frac{\alpha}{g} \in \mathfrak{o} \quad \text{and} \quad \frac{\beta}{g} \in \mathfrak{o}$$

according to the definition of the GCD. By assumption, we get $g \in \mathfrak{o}^\times$.
gcd $\Rightarrow$ strong:
Again, let g be a GCD of α, β and assume $g \in \mathfrak{o}^\times$. As explained above, we write $\kappa = \tau_0/\tau_1$. Now, define $\frac{\tau_0}{\tau_1}\alpha =: \lambda_0 \in \mathfrak{o}$ and $\frac{\tau_0}{\tau_1}\beta =: \lambda_1 \in \mathfrak{o}$ and hence

$$\tau_0\alpha = \tau_1\lambda_0, \quad \tau_0\beta = \tau_1\lambda_1 \,.$$

By construction, we can assume $\gcd_{\mathfrak{o}}(\tau_0, \tau_1) \in \mathfrak{o}^\times$ which makes the integer τ_1 both a factor of α and of β. Another common factor of α and β is g. Since g is by definition the greatest one with respect to the algebraic norm,

$$g \mid \alpha, \beta \;\wedge\; \tau_1 \mid \alpha, \beta \quad \Longrightarrow \quad |\mathrm{N}(\tau_1)| \le |\mathrm{N}(g)|$$

follows. But since

$$0 \ne |\mathrm{N}(\tau_1)| \le |\mathrm{N}(g)| = 1 \,,$$

we conclude $|\mathrm{N}(\tau_1)| = 1$. So, τ_1 is a unit and $\kappa = \tau_0/\tau_1$ is an element of $\mathfrak{o}$.
Next, we show that weak and strong primitivity are equivalent.
strong $\Rightarrow$ weak:
Let $\kappa \in \mathfrak{o}$ be an integer with $\kappa^{-1}z \in \mathbb{K}$. Define $\kappa_0 := \kappa^{-1} \in \Bbbk$, then $\kappa_0 z \in \mathbb{K}$ and by weak primivity we get $\kappa_0 \in \mathfrak{o}$, which is equivalent to $\kappa \in \mathfrak{o}^\times$.
weak $\Rightarrow$ strong:
First we note that $\mathcal{O}$ has *class number* one, which results in $\mathfrak{o}$ being a *PID*. Let $\kappa \in \Bbbk$ and write it again as $\kappa = \tau_0/\tau_1$ with coprime $\tau_0, \tau_1 \in \mathfrak{o}$. Since *Bézout's identity* holds in a PID (a PID is also a Bézout domain, see [17]) we find $\sigma_0, \sigma_1 \in \mathfrak{o}$ such that $\sigma_0\tau_0 + \sigma_1\tau_1 = 1$. Multiplication with $\frac{z}{\tau_1}$ yields

$$\sigma_0\frac{\tau_0}{\tau_1}z + \sigma_1 z \;=\; \frac{1}{\tau_1}z \,.$$

By assumption, $\frac{\tau_0}{\tau_1}z \in \mathcal{O}$, but then also $\frac{1}{\tau_1}z \in \mathcal{O}$. Using weak primitivity, we obtain $\tau_1 \in \mathfrak{o}^\times$, which then gives $\frac{\tau_0}{\tau_1} \in \mathfrak{o}$. ■

Procedure 4.8
To implement the algorithm to determine visibility of vertices, we need to decide whether a vertex is primitive. For this, we apply a generic Euclidean algorithm whose core is the modulo operation in the corresponding ring of integers.

```
input  : integers a, b
output : integer c
$x \leftarrow \mathsf{a}$;
$y \leftarrow \mathsf{b}$;
while $y \neq 0$ do
    $z \leftarrow y$;
    $y \leftarrow x \bmod y$;
    $x \leftarrow z$;
end
$\mathsf{c} \leftarrow x$;
```

Algorithm 2: Generic Euclidean algorithm.

The basis for the modulo is a division operation. For $n = 8$, we write

$$a \;=\; a_0 + a_1 \cdot \sqrt{2} \quad \text{and} \quad b \;=\; b_0 + b_1 \cdot \sqrt{2}$$

for the input integers from $\mathbb{Z}[\sqrt{2}]$. Assume a non-zero b, let $n := \mathrm{N}(b)$, and compute

$$\alpha \;=\; [(a_0 b_0 - 2a_1 b_1) \cdot n^{-1}] \quad \text{and} \quad \beta \;=\; [(a_1 b_0 - a_0 b_1) \cdot n^{-1}]$$

where $[\,\cdot\,]$ means rounding to the nearest integer in $\mathbb{Z}$. Consider the evaluation of the fraction $x := \frac{a}{b} = \frac{ab'}{bb'}$ in $\mathbb{Q}(\sqrt{2})$, then $y := \alpha + \beta \cdot \sqrt{2}$ gives us the closest integer result, i.e. $|x - y|$ is minimal with $y \in \mathbb{Z}[\sqrt{2}]$. To recover the remainder of the division operation, we compute $c := a - y \cdot b$. Then, c is the result of $a \bmod b$ in $\mathbb{Z}[\sqrt{2}]$. We can now apply the operation in Algorithm 2 to determine the GCD of the coordinates of the vertex, hence determining gcd-primitivity of the vertex.

This approach works the same way whenever $\mathfrak{o}$ is Euclidean by using the proper modulo operation. In case that $\mathfrak{o} = \mathbb{Z}$, we can apply faster algorithms, like the binary GCD; see [18] for reference.

Theorem 4.9
Let T_{AB} be vertices of the AB tiling, as introduced in Section 2.2. We consider a configuration where the origin $0_{\mathbb{R}^2}$ is a vertex and the tiling is D_8 symmetric with respect to the origin. The visible vertices with respect to the reference point $x_0 = 0_{\mathbb{R}^2}$ are given by

$$V_{\mathsf{AB}} \;=\; \{z \in T_{\mathsf{AB}} \;:\; z \text{ is } \mathfrak{o}\text{-primitive} \;\wedge\; \epsilon \cdot z^{\star} \notin W_{\mathsf{AB}}\}$$

where W_{AB} is the window in internal space and $\epsilon = 1 + \sqrt{2}$; compare Remark 4.4. We call ϵ the *critical* scaling factor.

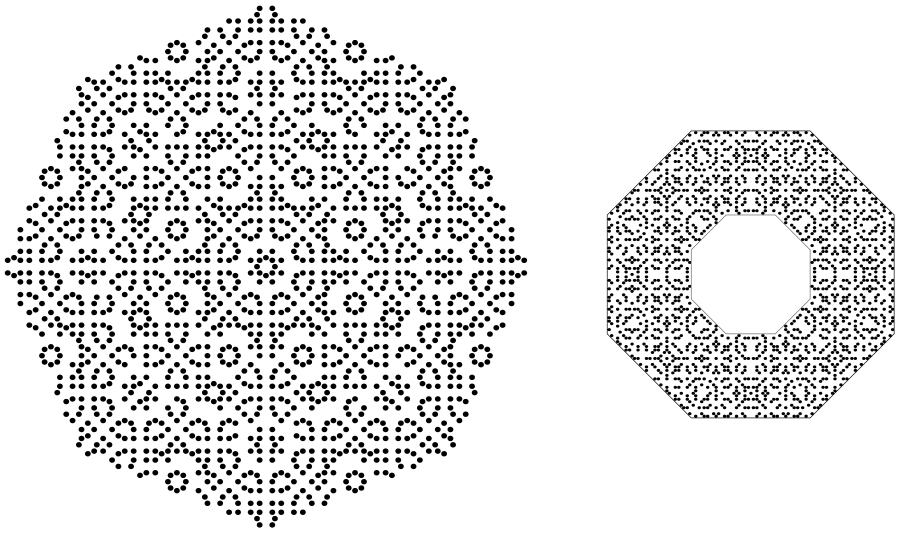

Figure 4.1. Visible vertices of the D_8 symmetric AB tiling in physical (left) and internal (right) space.

The second part of the visibility condition in Theorem 4.9 is really just a geometric condition in internal space. If a vertex is visible, then it lives on a “belt” of the window, which results from cutting out a scaled-down copy from the original window. Both windows are indicated on the right hand side of Fig. 4.1.

Before presenting the proof of Theorem 4.9, we formulate some preliminary properties.

Corollary 4.10
Let $z \in T_{\mathsf{AB}}$ be a non-primitive element, i.e. there exists $\kappa \in \mathfrak{o} \setminus \mathfrak{o}^{\times}$ such that $\frac{z}{\kappa} \in \mathcal{O}$. Assume that we can choose an $u \in \mathfrak{o}^{\times}$ such that $|(u\kappa)'| \geqslant 1$ holds. If we let $z_0 := z/(u\kappa)$, then $z_0 \in T_{\mathsf{AB}}$.

Proof. Since $z \in \mathcal{O}$ we also have $z_0 \in \mathcal{O}$. Applying the star map to z_0 yields

$$z_0^{\star} = \left(\frac{z}{u\kappa}\right)^{\star} = \frac{z^{\star}}{(u\kappa)'} \in W$$

since the window W is invariant under $x \mapsto -x$ and star-shaped with respect to the origin. Hence we see that $z_0 \in \curlywedge(W) = T_{\mathsf{AB}}$. ■

Lemma 4.11
Let $z \in T_{\mathsf{AB}}$ be a visible vertex. Then, z is primitive.

Proof. We assume to the contrary that there exists a non-primitive z that is visible. Since Corollary 4.10 holds for non-primitive elements, we need to construct an element u for the κ given there. We show that we can always construct a u such that $\kappa u > 1$. With this, z_0 occludes our initial element z which contradicts that z is visible.

construction of u:

We want to exploit the structure of the unit group $\mathfrak{o}^{\times} \subset \mathfrak{o}$ by moving the elements into a logarithmic space, see [11, Ch. 2.3.3] for details. Let $\tilde{\mathfrak{o}} := \mathfrak{o} \setminus \{0\}$ and define the map

$$\mathfrak{log} : \tilde{\mathfrak{o}} \longrightarrow \mathbb{R}^2 \quad \text{by} \quad \kappa \longmapsto \left(\log|\kappa|, \log\left|\kappa'\right|\right) .$$

The corresponding logarithmic space is then just the image $\Im(\mathfrak{log})$. If we only consider the units of $\mathfrak{o}$, then there exists some $\mathfrak{u} \in \mathbb{R}^2$, which turns the subset

$$\{\mathfrak{log}(u) \ : \ u \in \mathfrak{o}^{\times}\} \ = \ \mathbb{Z} \cdot \mathfrak{u} \, , \tag{4.5}$$

into a lattice inside $\mathbb{R} \cdot (1, -1)$. Since $\mathfrak{o}^{\times} = \{\pm\epsilon^k : k \in \mathbb{Z}\}$, the lattice basis vector can be written as $\mathfrak{u} := (\log(\epsilon), \log|\epsilon'|)$. We keep in mind that, as a line in $\mathbb{R}^2$, it has slope -1.

By our assumptions, we have $\kappa \in \mathfrak{o} \setminus \mathfrak{o}^{\times}$, which translates to

$$\mathfrak{log}(\kappa) \in \mathbb{R} \cdot (1, -1) + \mathfrak{s}$$

in logarithmic space, i.e. the corresponding line is shifted by some translation. We denote this object as the κ-line in the rest of the proof. We can now further quantify the *shift* $\mathfrak{s}$ by writing

$$\mathfrak{log}(\kappa) \in \mathbb{R} \cdot (1, -1) + (0, \log(m)) \tag{4.6}$$

with $m := |\mathrm{N}(\kappa)|$. Since κ is not a unit, we in particular have $m = |\kappa\kappa'| \in \mathbb{N}_{\geqslant 2}$. That Eq. (4.6) is true can be seem from the following calculation.

$$\begin{aligned}
\mathfrak{log}(\kappa) = r \cdot (1, -1) + (0, \log(m)) \quad &\text{with} \quad r \in \mathbb{R} && \Longleftrightarrow \\
r = \ \log|\kappa| \quad \wedge \quad \log\left|\kappa'\right| &= -r + \log(m) && \Longleftrightarrow \\
r = \ \log|\kappa| \quad \wedge \quad \log\left|\kappa'\kappa\right| &= \log(m)
\end{aligned}$$

The numerical value of $\log(2)$ is roughly 0.693 which maps to a shift of the κ-line to the upper right quadrant.

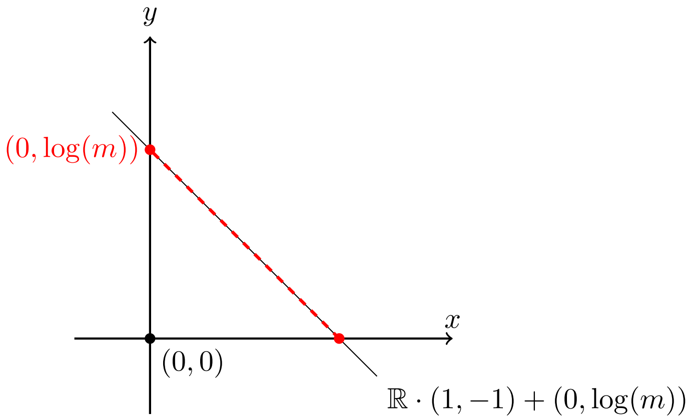

Figure 4.2. First quadrant of the logarithmic space.

The necessary unit u has to move κ onto the dashed line segment L, i.e. we want to have

$$\mathfrak{log}(\kappa u) \in \{(x, y) \ : \ x, y > 0\} \, .$$

First, consider $m \geqslant 3$. In this case, $\epsilon \approx 2.4 < m$ and hence also $\log(\epsilon) < \log(m)$. By repeated application of units, κ can therefore be moved onto L, i.e. there exists $u \in \mathfrak{o}^{\times}$ such that $|\kappa u| > 1$ and $|(\kappa u)'| > 1$. Potentially, we have to replace u by $-u$ here, but this does not affect the second property.
For the remaining case, we consider $m = 2$, but then κ is of the form $\kappa = \sqrt{2}v$, $v \in \mathfrak{o}^{\times}$, using the prime factorization in $\mathfrak{o}$. Define $u := v^{-1}$. Then, we have $u \in \mathfrak{o}^{\times}$, $\kappa u = \sqrt{2} > 1$, and $|(\kappa u)'| = |\sqrt{2}'| = \sqrt{2} > 1$. ■

We want to point out that the number of steps in this proof, in terms of handling of special cases (here $m = 2$), is tied to the magnitude of the fundamental unit. If the unit is “small”, then we have more fine-grained control about where we can move elements to in logarithmic space. This is going to become more apparant once we inspect the GS tiling later in this chapter.

Lemma 4.12
Let $z \in \mathcal{O} \setminus \{0\}$, then z is primitive iff $\mathbb{R}z \cap \mathcal{O} = \mathfrak{o}z$.

Proof. For the $\subseteq$ direction, let $r \in \mathbb{R}$ such that $rz \in \mathcal{O}$. But then we already see that $r \in \Bbbk$ holds and, by an application of strong primitivity, $r \in \mathfrak{o}$ follows. The other $\supseteq$ direction is trivial since $\mathfrak{o} \subset \mathbb{R}$ and $\kappa\mathcal{O} \subset \mathcal{O}$ for all $\kappa \in \mathfrak{o}$. ■

Lemma 4.13 (Critical scaling factor for AB)
We can quantify the magnitude of scaling factors in internal space as

$$\min \{ |\kappa'| \ : \ \kappa \in \mathfrak{o} \cap (0,1) \} \ = \ \epsilon \ = \ 1 + \sqrt{2} \, .$$

Proof. This result follows from another application of logarithmic space. Since $\log((0,1)) = (-\infty, 0)$, we operate on the following subset

$$\{\mathfrak{log}(\kappa) \ : \ \kappa \in \mathfrak{o} \cap (0,1)\} \ \subseteq \ (-\infty, 0) \times \mathbb{R} \subset \mathbb{R}^2 \, .$$

From Eq. (4.6) in the proof of Lemma 4.11, we know that

$$\mathfrak{log}(\kappa) \ \in \ \mathbb{R} \cdot (1, -1) + (0, \log{(m)})$$

with $m := |\mathrm{N}(\kappa)|$. Hence, we need to show that

$$\{\mathfrak{log}(\kappa) \ : \ \kappa \in \mathfrak{o} \cap (0,1)\} \ \subseteq \ (-\infty, 0) \times [\log \epsilon, \infty) \tag{4.7}$$

holds. If κ is a unit, we have $\log(m) = 0$ and using $\kappa \in (0,1)$ we see that $\kappa = \epsilon^{-k}$ for some $k \in \mathbb{N}$. Then, $\log|\kappa'| \geqslant \log(\epsilon)$ follows since $k \log{(\epsilon)} \geqslant \log{(\epsilon)}$.
Now, consider $\mathfrak{log}(\kappa)$ where κ is not a unit. Then, there exists $r < 0$ such that $\mathfrak{log}(\kappa) = (r, -r + \log{(m)})$. Since $1 + \sqrt{2} \approx 2.4$, we have $2 < \epsilon < 3$ and it suffices to show Eq. (4.7) for κ with $m = 2$. These κ are of the type $\sqrt{2}u$ with $u \in \mathfrak{o}^{\times}$.

Once again, we use $\kappa \in (0,1)$ and write $u = \epsilon^{-k}$ with $k \in \mathbb{N}$. With this, the following inequality

$$\log\left|\kappa'\right| = \log\left(\sqrt{2}(-\epsilon')^{-k}\right) \geqslant \log\left(2+\sqrt{2}\right) > \log\left(1+\sqrt{2}\right) = \log\epsilon$$

holds. Here, we have used $-\epsilon' = \epsilon^{-1}$ and $(-\epsilon')^k \leqslant -\epsilon'$ since $0 < \epsilon^{-1} < 1$. ■

Proof of Theorem 4.9. We start with the initial geometric meaning of visibility from Definition 4.1. If $z \in T_{\mathsf{AB}}$ is a visible vertex, we have

$$\begin{aligned} &\forall\, \lambda \in (0,1) \quad \forall\, y \in T_{\mathsf{AB}} \ : \ \lambda \cdot z \neq y && \Longleftrightarrow \\ &\forall\, \lambda \in (0,1) \ : \ \lambda \cdot z \in \mathcal{O} \implies \lambda \cdot z \notin T_{\mathsf{AB}} \,. \end{aligned}$$

By Lemma 4.11, we see that z has to be primitive. By an application of Lemma 4.12, the condition can be rewritten as

$$\forall\, \kappa \in \mathfrak{o} \cap (0,1) \ : \ \kappa \cdot z \notin T_{\mathsf{AB}} \,.$$

Next, we focus on the window condition of the tiling. Since $\kappa \cdot z \in \mathcal{O}$ always holds, we can replace the condition $\kappa \cdot z \notin T_{\mathsf{AB}}$ by $(\kappa \cdot z)^\star \notin W_{\mathsf{AB}}$. To further simplify this property, we introduce

$$\ell \ := \ \ell(z) \ := \ \operatorname{diam}(W \cap \mathbb{R}_+ z^\star)$$

where $W = W_{\mathsf{AB}}$.

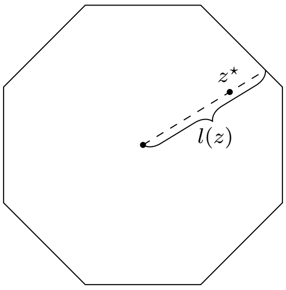

Figure 4.3. Example for $\ell(z)$ in the case of the AB tiling which has a regular octagon as its window.

Because our W is star-shaped and invariant under inversion, i.e. replacing z by $-z$, we have $(\kappa \cdot z)^\star \notin W$ iff $|\kappa' \cdot z^\star| > \ell$. So, the visibility condition turns into

$$\forall\, \kappa \in \mathfrak{o} \cap (0,1) \ : \ \left|\kappa'\right| \cdot |z^\star| > \ell \,.$$

By Lemma 4.13, we see that it suffices to test this inequality for a single κ, which satisfies $|\kappa'| = \epsilon$ here. With this, the condition reduces to $\epsilon \cdot z^\star \notin W$.

For the other direction, consider a primitive $z \in T_{\mathsf{AB}}$ such that $\epsilon \cdot z^\star \notin W$ holds and assume that z is invisible. Then, there exists a visible vertex that occludes z, i.e.

$$\exists\, \kappa \in \mathfrak{o} \cap (0,1) \ : \ \kappa \cdot z \in V_{\mathsf{AB}} \,,$$

where we have used primitivity of z through Lemma 4.12. If $\kappa \cdot z$ is visible, then it is also primitive by Lemma 4.11 and κ has to be a unit, i.e. $\kappa \in \mathfrak{o}^{\times}$. By using $\kappa \in (0,1)$, we see that κ has to be of the form $(-\epsilon')^k = (\sqrt{2}-1)^k$ which leads to the following inequality

$$|(\kappa \cdot z)^{\star}| \;=\; \left|\kappa' \cdot z^{\star}\right| \;=\; \epsilon^k \cdot |z^{\star}| \;\leqslant\; \ell(z) \;,$$

where we have used $(\kappa \cdot z)^{\star} \in W$. But since $\epsilon > 1$, we also have

$$\epsilon^k \cdot |z^{\star}| > \epsilon \cdot |z^{\star}| > \ell(z) \;,$$

where we have used $\epsilon \cdot z^{\star} \notin W$. This is a contradiction, hence z has to be visible. ∎

Theorem 4.14
Let T_{TT} be vertices of the TT tiling. Again, we assume that $0_{\mathbb{R}^2} \in T_{\mathsf{TT}}$ with the tiling having maximal symmetry with respect to the origin. Then, the visible vertices with respect to the reference point $x_0 = 0_{\mathbb{R}^2}$ are given by

$$V_{\mathsf{TT}} \;=\; \{z \in T_{\mathsf{TT}} \;:\; z \text{ is } \mathfrak{o}\text{-primitive},\; \epsilon \cdot z^{\star} \notin W_{\mathsf{TT}} - s\}$$

where W_{TT} is the centred (unshifted) window in internal space and $\epsilon = \tau$ the critical scaling factor; also compare Remark 4.4.

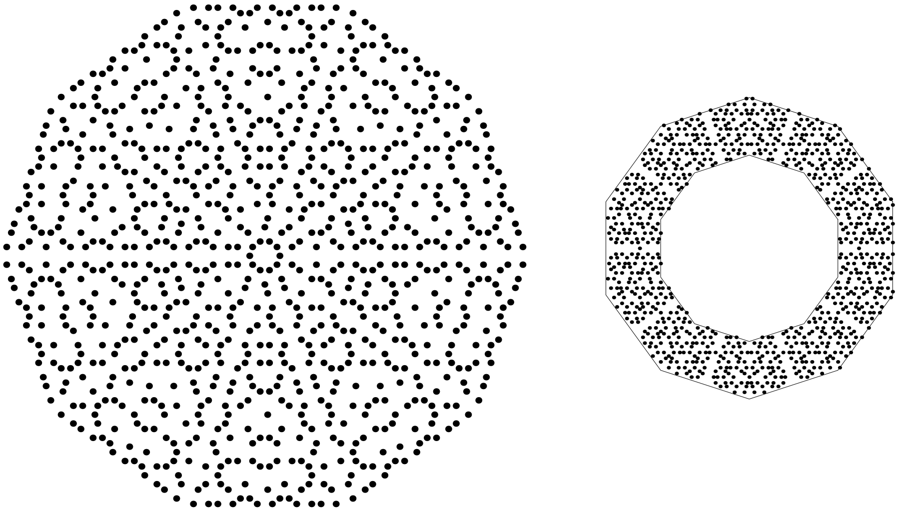

Figure 4.4. Visible vertices of a TT tiling in physical (left) and internal (right) space.

Remark 4.15
We pointed out in Section 2.3 that a shift s has to be applied to the window of the TT tiling to avoid singular vertices. We did not quantify s at that point, but its size is going to become crucial for properly describing the visible vertices. In particular, we are slightly cheating in Theorem 4.14, since the description is only

valid as long as we consider finite patches of the tiling. We refer to the proof of Theorem 4.14 for details.

Note that this issue also applies to the GS tiling. A solution to the problem would be, instead of shifting the window, to declare only one half of the boundary as part of the window. Obviously, this then brings back the peculiarities of some numerical test for vertices on the boundary of the window.

We again start by collecting some preliminary properties. In particular, we want to point out that we can adapt the proof for the AB tiling here. The main difference is the shifted window, which breaks the property that $W = W_{\mathsf{TT}} + s$ is invariant under the transformation $x \mapsto -x$. We can however show that this does not pose a problem if we keep track of sign changes caused by algebraic conjugation.

We recall that the vertex set T_{TT} is given by

$$T_{\mathsf{TT}} \;=\; \{z \in \mathcal{O} \;:\; z^{\star} \in W_{\mathsf{TT}} + s\} \;,$$

where the shift s of W is in positive direction, in contrast to the negative shift for V_{TT}.

We first adapt Corollary 4.10 as follows.

Corollary 4.16

Let $z \in T_{\mathsf{TT}}$ again be a non-primitive element with $\kappa \in \mathfrak{o} \setminus \mathfrak{o}^{\times}$ such that $\frac{z}{\kappa} \in \mathcal{O}$. Under the assumption that a $u \in \mathfrak{o}^{\times}$ exists with the properties $u\kappa > 1$ and $|(u\kappa)'| \geqslant 1$, we define $z' := z/(u\kappa)$ and obtain $z' \in T_{\mathsf{TT}}$.

Proof. The proof works in the same way as for Corollary 4.10 except that we have to rule out the case $|(u\kappa)'| = 1$. The window now only satisfies

$$-W \;=\; -(W_{\mathsf{TT}} + s) \;=\; -W_{\mathsf{TT}} - s \;=\; W_{\mathsf{TT}} - s \;=\; W - 2s$$

which would conflict with elements of absolute value 1. Assume that we have a pair u, κ such that $(u\kappa)' \in \{\pm 1\}$. Applying the norm gives us $\mathrm{N}(u\kappa) = 1$ but $\mathrm{N}(\kappa) \neq 1$ and $|\mathrm{N}(u)| = 1$, which leads to a contradiction.

Hence, we only encounter the case $|(u\kappa)'| < 1$ and with the shift s sufficiently small, we can complete the proof. ■

We refer to the proof of Theorem 4.14 for a quantification of the shift s.

Lemma 4.17

Let $z \in T_{\mathsf{TT}}$ be a visible vertex. Then z is primitive.

Proof. In the proof of Lemma 4.11, we have seen that the magnitude of the fundamental unit ϵ plays a crucial role. In this case, we have $\epsilon \approx 1.61$ and since we only consider $m \geqslant 2$ (see the end of the proof of Lemma 4.11), we automatically have $\log(\epsilon) < \log(m)$. Some additional special case as for AB therefore is not

necessary here.
The rest of the proof works analogously. ■

Remark 4.18
Consider any star-shaped window W_{std} which is invariant under the inversion map $x \mapsto -x$, and let $s := (s_0, s_0)$ with $s_0 > 0$ small. Let $W := W_{\mathsf{std}} + s$ and define

$$I_\pm \;:=\; I_\pm(z) \;:=\; z^\star \mathbb{R}_\pm \cap W$$

for z some vertex in physical space. Here, $\mathbb{R}_\pm$ is defined as $\mathbb{R}_{\geqslant 0}$ and $\mathbb{R}_{\leqslant 0}$, respectively. Using these two sets, define lengths

$$\ell_\pm \;:=\; \ell_\pm(z) \;:=\; \operatorname{diam}(I_\pm)$$

and another two sets $I^0_\pm := \mathbb{R}_\pm z^\star$. For $\kappa \in \mathfrak{o}$, we can encounter two sitations,

(1) $z^\star \in I_+$ and $\kappa' \cdot z^\star \in I^0_+$,
(2) $z^\star \in I_+$ and $\kappa' \cdot z^\star \in I^0_-$.

Now, consider only $0 < \kappa < 1$. Then, in the first case, the sign of κ stays unchanged under algebraic conjugation, whereas it does change in the second case.
We want to study the magnitude of $|\kappa'|$ for both cases.

As we have seen in Remark 4.18, we need to consider both sign-changing elements and non-sign-changing ones.

Lemma 4.19 (Critical scaling factors for TT)
We have

$$\min\{\kappa' \;:\; \kappa \in \mathfrak{o} \cap (0,1) \;\wedge\; \kappa' > 0\} = 1 + \epsilon$$

and

$$\min\{-\kappa' \;:\; \kappa \in \mathfrak{o} \cap (0,1) \;\wedge\; \kappa' < 0\} = \epsilon\ .$$

Hence, the absolute value minimum over all $\mathfrak{o} \cap (0,1)$ is ϵ.

Proof. Here, we can again apply the procedure from the proof of Lemma 4.13, with the addition of a case-by-case analysis depending on the sign of κ'.
First, we note that, since $1 < \epsilon < 2$ holds, it suffices to look at $\kappa \in \mathfrak{o}^\times$, i.e. at elements of the form $\kappa = \pm\epsilon^k$ with $k \in \mathbb{Z}$. Using $\kappa \in (0,1)$, we can reduce this to $\kappa = \epsilon^{-k}$, where $k \geqslant 1$. The sign of κ' now just depends on the parity of k, hence we obtain $\kappa' > 0$ for k even and $\kappa' < 0$ for k odd. The minimum of the first set is then computed by taking the smallest even k, resulting in $\kappa' = \epsilon^2 = \epsilon + 1$. The second set works analogously, where we have $k = 1$ and therefore $\kappa' = \epsilon$. ■

Lemma 4.20
Let $z \in \mathcal{O} \setminus \{0\}$. Then, z is primitive iff $\mathbb{R}z \cap \mathcal{O} = \mathfrak{o}z$.

Proof. This is a step-by-step repetition of the proof of Lemma 4.12. ■

Proof of Theorem 4.14. This proof is similar to the one of Theorem 4.9, hence we focus on the steps that are different.
We begin by restating the geometric condition for a visible vertex $z \in T_{\mathsf{TT}}$,

$$\forall\, \lambda \in (0,1) \quad \forall\, y \in T_{\mathsf{TT}} \;:\; \lambda \cdot z \neq y \;.$$

We know from Lemma 4.17 that z has to be primitive, hence we can reformulate the condition as

$$\begin{aligned} \forall\, \kappa \in \mathfrak{o} \cap (0,1) \;&:\; (\kappa \cdot z)^\star \notin W \iff \\ \forall\, \kappa \in \mathfrak{o} \cap (0,1) \;&:\; \big(\kappa' > 0 \;\Rightarrow\; \kappa' \cdot z^\star \notin W\big) \;\wedge \\ &\;\; \big(\kappa' < 0 \;\Rightarrow\; \kappa' \cdot z^\star \notin W\big) \;. \end{aligned}$$

Using the definitions from Remark 4.18 and the fact that W is star-shaped with respect to x_0, we can write this as

$$\begin{aligned} \forall\, \kappa \in \mathfrak{o} \cap (0,1) \;:\; &\big(\kappa' > 0 \;\Rightarrow\; +\kappa' \cdot |z^\star| > \ell_+(z)\big) \;\wedge \\ &\big(\kappa' < 0 \;\Rightarrow\; -\kappa' \cdot |z^\star| > \ell_-(z)\big) \;. \end{aligned}$$

Now, apply Lemma 4.19 which further reduces the condition to

$$(1+\epsilon) \cdot |z^\star| > \ell_+ \quad \wedge \quad \epsilon \cdot |z^\star| > \ell_- \;.$$

Let P be a finite patch of the tiling around the reference point $x_0 = 0$. Define

$$s_0 \;:=\; \frac{1}{\sqrt{2}} \min_{z \in P \setminus \{0\}} |z^\star| \;,$$

so we have $\|s\| = s_0$ and furthermore $|\ell_+ - \ell_-| \leqslant s_0$. With this relation, we can show that

$$\epsilon \cdot |z^\star| > \ell_- \;\Rightarrow\; (1+\epsilon) \cdot |z^\star| = |z^\star| + \epsilon \cdot |z^\star| > \ell_- + |z^\star| \overset{(*)}{>} \ell_+ \;,$$

where we have used $|z^\star| > s_0 \geqslant |\ell_+ - \ell_-|$ for all $z \in P$ in the last estimate $(*)$. This shows that the condition for $\ell_-(z)$ already implies the condition for $\ell_+(z)$. Since we have

$$\epsilon \cdot |z^\star| > \ell_- \quad \iff \quad \epsilon \cdot z^\star \notin W_{\mathsf{TT}} - s \;,$$

this gives us the sought-after condition. ■

4.1.2. Twelve-fold case – the shield tiling.

The algebraic structure of the twelve-fold case, i.e. choosing $\mathbb{K} = \mathbb{Q}(\zeta_{12})$, is slightly more complicated. Therefore, we need to modify some definitions.

Remark 4.21
For $n = 12$, we have $\Bbbk = \mathbb{Q}(\sqrt{3})$, $\mathfrak{o} = \mathbb{Z}[\sqrt{3}]$, $\epsilon = 2 + \sqrt{3}$ and the algebraic conjugate $a - b \cdot \sqrt{3}$ for an element $a + b \cdot \sqrt{3} \in \mathfrak{o}$. The norm can be written as

$$x \;=\; a + b \cdot \sqrt{3} \quad \longmapsto \quad \mathrm{N}(x) \;=\; x \cdot x' \;=\; a^2 - 3b^2 \;.$$

The group of units is given by

$$\mathfrak{o}^{\times} \;=\; \{\pm\epsilon^{k} \;:\; k \in \mathbb{Z}\}\;.$$

Definition 4.22
We construct a map $n\colon \mathcal{O} \to \mathbb{N}_{\geqslant 1}$ by

$$n(z) \;:=\; |\mathrm{N}(\gcd(z))|\;,$$

which is well-defined as explained in Definition 4.5. In addition to the fundamental unit ϵ from Remark 4.21, we need another special element

$$\gamma \;:=\; 1+\sqrt{3}\,, \tag{4.8}$$

which has norm $\mathrm{N}(\gamma) = -2$.

Remark 4.23
The element γ above generates the subset of absolute norm 2 elements from $\mathfrak{o}$ in the following sense

$$\{x \in \mathfrak{o} \;:\; |\mathrm{N}(x)| = 2\} \;=\; \gamma \cdot \mathfrak{o}^{\times}\;.$$

This can be seen from the fact that 2 ramifies in $\mathfrak{o}$, i.e. we have

$$2 \;=\; (1+\sqrt{3})^{2}\cdot(2-\sqrt{3}) \;=\; \gamma^{2}u \quad \text{with } u \text{ some unit.}$$

These elements play a special role for determining visibility in the twelvefold case.

We now describe a modified version of primitivity as given in Definition 4.5.

Definition 4.24
Let $z \in \mathcal{O}$ be non-zero. We say that z is *strongly* $\mathfrak{o}$-primitive when

$$\forall\, \kappa \in \mathbb{k} \;:\; \kappa z \in \mathcal{O} \implies \gamma\kappa \in \mathfrak{o}$$

with γ as defined in Eq. 4.8. We call z *weakly* $\mathfrak{o}$-primitive if

$$\forall\, \kappa \in \mathfrak{o} \;:\; z \in \kappa\mathcal{O} \implies |\mathrm{N}(\kappa)| \leqslant 2$$

and 2-coprime if $n(z) \leqslant 2$.

Lemma 4.25
Let $\kappa \in \mathfrak{o}$ be non-zero and consider κ^{-1} as an element in $\mathbb{k}$. Then, one has

$$|\mathrm{N}(\kappa)| \leqslant 2 \quad\Longleftrightarrow\quad \kappa^{-1} \in \frac{1}{\gamma}\mathfrak{o}\;.$$

Proof. We have two cases for the first direction. If $|\mathrm{N}(\kappa)| = 1$, then κ already is a unit and hence $\kappa \in \mathfrak{o}^{\times} \subseteq \frac{1}{\gamma}\mathfrak{o}$. If $|\mathrm{N}(\kappa)| = 2$, we have $\kappa = \gamma u$ with $u \in \mathfrak{o}^{\times}$. The inverse can therefore be written as $\kappa^{-1} = \frac{1}{\gamma}u^{-1} \in \frac{1}{\gamma}\mathfrak{o}$.
For the other direction, let $t \in \mathfrak{o}$ such that $\gamma = \kappa t$. It follows that

$$-2 \;=\; \mathrm{N}(\gamma) \;=\; \mathrm{N}(\kappa)\,\mathrm{N}(t) \quad\implies\quad \mathrm{N}(\kappa) \in \{\pm 1, \pm 2\}\;,$$

which implies our claim. ■

Like in the two simpler cases (AB and TT), we also have equivalence of primitivity here.

Theorem 4.26
For $\mathbb{K} = \mathbb{Q}(\zeta_{12})$, all three types of primitivity from Definition 4.24 are equivalent.

Proof. This proof mimics that of Theorem 4.7.
strong $\Rightarrow$ weak:
Let $\kappa \in \mathfrak{o} \setminus \{0\}$, $z \in \kappa\mathcal{O}$ and define $\kappa' := \kappa^{-1}$. Then, $\kappa' x \in \mathcal{O}$ follows and, using the strong primitivity, we get $\kappa' \in \frac{1}{\gamma}\mathfrak{o}$. In other words, we have $\gamma = \kappa t$ for some $t \in \mathfrak{o}$. Using Lemma 4.25, we see that $|\mathrm{N}(\kappa)| \leqslant 2$.
weak $\Rightarrow$ strong:
Let $\kappa \in \mathbb{k}$ and write is as $\kappa = \frac{\tau}{\tau'}$ with coprime τ and τ'. With Bézout, we construct σ, σ' such that $\sigma\tau + \sigma'\tau' = 1$. Multiplication of the equation with $\frac{z}{\tau'}$ yields

$$\begin{aligned} \sigma \cdot \frac{\tau}{\tau'} z + \sigma' \cdot z = \frac{z}{\tau'} \quad &\Longleftrightarrow \\ \sigma\kappa \cdot z + \sigma' \cdot z = \frac{z}{\tau'} \; . \end{aligned} \tag{4.9}$$

Since $\sigma\kappa z \in \mathcal{O}$ and $\sigma' z \in \mathcal{O}$, Eq. (4.9) shows us that $\frac{z}{\tau'} \in \mathcal{O}$ or equivalently $z \in \tau'\mathcal{O}$. Weak primitivity now implies $|\mathrm{N}(\tau')| \leqslant 2$ and, by Lemma 4.25, we conclude that $\frac{1}{\tau'} \in \frac{1}{\gamma}\mathfrak{o}$. Multiplication with τ brings us to $\frac{\tau}{\tau'} = \kappa \in \frac{1}{\gamma}\mathfrak{o}$, which completes this implication.
weak $\Leftrightarrow$ 2-coprime:
We write z as $\alpha + \beta \cdot \zeta$ and define $g := \gcd(\alpha, \beta)$. Since $\frac{\alpha}{g} \in \mathfrak{o}$ and $\frac{\beta}{g} \in \mathfrak{o}$, we know that $\frac{z}{g} \in \mathcal{O} \Leftrightarrow z \in g\mathcal{O}$. Using weak primitivity, this implies $|\mathrm{N}(g)| \leqslant 2$. Since $n(z)$ is defined through $|\mathrm{N}(z)|$, this already shows the implication. The other direction follows analogously. ■

Theorem 4.27
Let T_{GS} be the vertices of the GS tiling. Again, we assume that $0_{\mathbb{R}^2} \in T_{\mathsf{GS}}$ with the tiling having maximal symmetry with respect to the origin; see Section 2.4 for the parameter of the CPS construction, which yields such a configuration. Then, the visible vertices with respect to the reference point $x_0 = 0_{\mathbb{R}^2}$ are given by

$$\begin{aligned} V_{\mathsf{GS}} \; &= \{z \in T_{\mathsf{GS}} \; : \; n(z) = 1 \; \wedge \; \lambda_1 \cdot z^\star \notin W_{\mathsf{GS}} - s\} \; \cup \\ &\quad \{z \in T_{\mathsf{GS}} \; : \; n(z) = 2 \; \wedge \; \lambda_2 \cdot z^\star \notin W_{\mathsf{GS}} - s\} \end{aligned}$$

where W_{GS} is the centred (unshifted) window in internal space with $\epsilon = 2 + \sqrt{3}$. The two scaling factors are

$$\lambda_1 \; := \; \sqrt{\epsilon \cdot 2} \; = \; \gamma \quad \text{and} \quad \lambda_2 \; := \; \sqrt{\epsilon/2} = \frac{1}{2}\gamma \; .$$

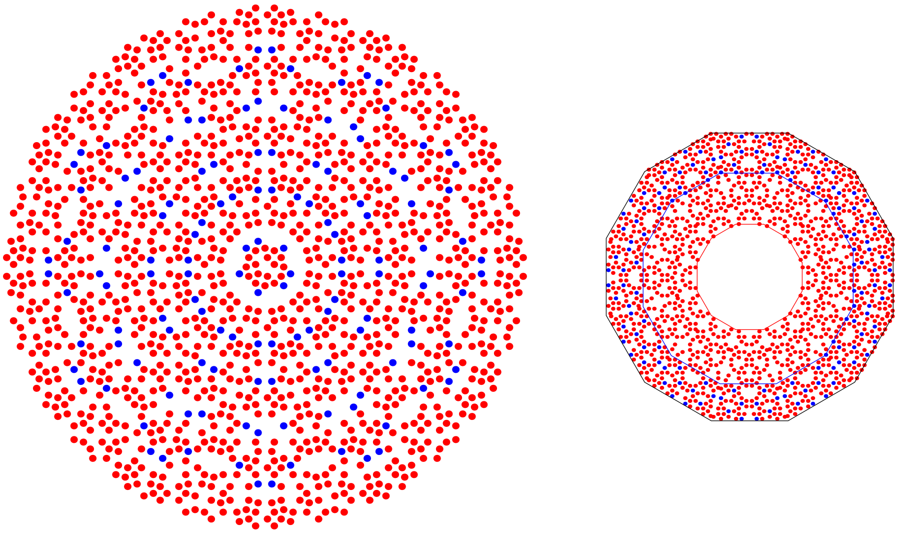

Figure 4.5. Visible vertices of a GS tiling in physical (left) and internal (right) space. See text for the colour coding.

Compared to AB and TT, we now have two types of vertices here. The elements with $n(z) = 1$ are displayed in red in Fig. 4.5, while the exceptional elements, i.e. these with $n(z) = 2$, are indicated in blue. The two different windows can be distinguished by their border color.

Once again, we collect some preliminary properties first. We re-use Corollary 4.16 and Remark 4.18.

Lemma 4.28

Let $z \in T_{\mathsf{GS}}$ be a visible vertex. Then, z is primitive.

Proof. We know from the previous proofs that the magnitude of the fundamental unit determines the cases we have to look at. Here, we have $\epsilon \approx 3.732$, so the construction from Theorem 4.9 works for all $m \geqslant 4$. This leaves just the case $m = 3$, since $m = 2$ is allowed now, due to our modified definition of primitivity. Using prime factorization in $\mathfrak{o}$, we can write a κ with $m = 3$ as

$$\kappa \;=\; \sqrt{3}u, \quad u \in \mathfrak{o}^{\times},$$

where we have $\sqrt{3} \approx 1.732$. Since $|\sqrt{3}'| = \sqrt{3}$, we can apply the same procedure as for the special case $m = 2$ in the proof of Theorem 4.9.

In particular, we can see also here why this does not work for any κ with $m = 2$. These elements are of the type γu (see Definition 4.22) and despite $\gamma \approx 2.732 > 1$ we have $\gamma' \approx -0.732$, so the absolute value is strictly smaller than one. ∎

We have to consider four critical scaling factors for the GS tiling. Like for the TT tiling, we have to distinguish between sign-changing and non-sign-changing elements. Additionally, we differentiate between elements coming from vertices z with $n(z) = 1$ and $n(z) = 2$.

Lemma 4.29 (Critical scaling factor for GS)
The factors for the GS tiling are given by computing the minima

$$\begin{aligned} \min\{\kappa' \;:\; \kappa \in \mathfrak{o} \cap (0,1) \;\wedge\; \kappa' > 0\} &= \epsilon \\ \min\{-\kappa' \;:\; \kappa \in \mathfrak{o} \cap (0,1) \;\wedge\; \kappa' < 0\} &= \gamma \,. \end{aligned}$$

for $n(z) = 1$, where the minimum is achieved by $\kappa = 2 - \sqrt{3}$ and $\kappa = -1 + \sqrt{3}$, respectively, and

$$\begin{aligned} \min\{\kappa' \;:\; \kappa \in \frac{1}{\gamma}\mathfrak{o} \cap (0,1) \;\wedge\; \kappa' > 0\} &= \frac{\gamma}{2}\sqrt{3} \\ \min\{-\kappa' \;:\; \kappa \in \frac{1}{\gamma}\mathfrak{o} \cap (0,1) \;\wedge\; \kappa' < 0\} &= \frac{\gamma}{2} \,. \end{aligned}$$

for $n(z) = 2$. Here, the minimum is achieved by $\kappa = \sqrt{3}/\gamma$ and $\kappa = 2/\gamma$. The fractions come from the relation $\gamma\gamma' = -2$ which gives rise to writing the inverse of γ as

$$\gamma^{-1} = -\frac{\gamma'}{2} \,.$$

Proof. We have seen in the proof for Lemma 4.19 how to handle sign-changes. Here we just repeat these steps, while also discerning between the cases $n(z) = 1$ and $n(z) = 2$. ■

Lemma 4.30
Let $z \in \mathcal{O} \setminus \{0\}$. Then, z is primitive iff

$$\mathbb{R}z \cap \mathcal{O} = \begin{cases} \frac{1}{\gamma}\mathfrak{o}z & : \text{ if } n(z) = 1 \,, \\ \mathfrak{o}z & : \text{ if } n(z) = 2 \,. \end{cases}$$

Proof. Both cases are another step-by-step repetition of the proof of Lemma 4.12, using the modified primitivity from Definition 4.24. ■

Proof of Theorem 4.27. As usual, we first restate our initial geometric condition for $z \in T_{\mathsf{GS}}$ being a visible vertex,

$$\forall\, \lambda \in (0,1) \quad \forall\, y \in T_{\mathsf{GS}} \;:\; \lambda \cdot z \neq y \,.$$

By Lemma 4.28, we know that only primitive z are to be examined, i.e. z with either $n(z) = 1$ or $n(z) = 2$. Not using this information yet, we rewrite the condition as

$$\forall\, \lambda \in (0,1) \;:\; \lambda \cdot z \in \mathcal{O} \implies \lambda \cdot z \notin T_{\mathsf{GS}} \,,$$

where we now like to replace the first part with $\forall\, \kappa \in \frac{1}{\gamma}\mathfrak{o} \cap (0,1)$. We still have the property that

$$\kappa \cdot z \in \mathcal{O} \implies \kappa \in \frac{1}{\gamma}\mathfrak{o} \,,$$

but the converse need not be true in general. This is different to the proof for the AB and TT tiling, where we could always assume that the equivalence

$$\kappa \cdot z \in \mathcal{O} \quad \Longleftrightarrow \quad \kappa \in \mathfrak{o}$$

holds. We consider the two types of z separately.
Let $n(z) = 1$. Then, we need to determine for which κ (as a subset of $\frac{1}{\gamma}\mathfrak{o}$) the statement $\kappa \cdot z \in \mathcal{O}$ is true. If $\kappa \in \mathfrak{o}$, it is obviously correct, so let $\kappa \in \frac{1}{\gamma}\mathfrak{o} \setminus \mathfrak{o}$ and write $\kappa = \beta/\gamma$ as a maximally reduced fraction (note that γ is not a unit). In particular, $\mathrm{N}(\kappa)$ is also a fractional value. Since we have $n(z) = 1$, the GCD of z has absolute norm 1, i.e.

$$z = \alpha + \beta \cdot \zeta, \quad g = \gcd(\alpha, \beta) \in \mathfrak{o}^{\times} \ .$$

If $\kappa \cdot z \in \mathcal{O}$ should hold, we also need $\kappa\alpha, \kappa\beta \in \mathfrak{o}$, which is impossible since $\mathrm{N}(\kappa\alpha)$ and $\mathrm{N}(\kappa\beta)$ are still fractional due to their GCD being a unit. The statement is therefore only satisfied for $\kappa \in \mathfrak{o}$.
For any z with $n(z) = 2$, we can always find a $g \in \mathfrak{o}$ with $|\mathrm{N}(g)| = 2$ such that $\frac{z}{g} \in \mathcal{O}$ holds. From Definition 4.22, we know how such g looks like and it immediately follows that $\kappa \cdot z \in \mathcal{O}$ is true for all $\kappa \in \frac{1}{\gamma}\mathfrak{o}$.
This way, we see that

$$\begin{aligned} n(z) = 1 \ &: \ \kappa \cdot z \in \mathcal{O} \quad \Longleftrightarrow \quad \kappa \in \mathfrak{o} \quad \text{and} \\ n(z) = 2 \ &: \ \kappa \cdot z \in \mathcal{O} \quad \text{is always satisfied} \end{aligned}$$

holds. Using this information together with Lemma 4.30, we can reformulate the visibility condition as

$$\begin{aligned} \forall\, \kappa \in \frac{1}{\gamma}\mathfrak{o} \cap (0,1) \ &: \ \kappa \cdot z \notin T_{\mathsf{GS}} \quad \text{if } n(z) = 1 \ , \\ \forall\, \kappa \in \mathfrak{o} \cap (0,1) \ &: \quad \kappa \cdot z \notin T_{\mathsf{GS}} \quad \text{if } n(z) = 2 \ . \end{aligned} \tag{4.10}$$

Now, we can proceed as usual by transforming the condition $\kappa \cdot z \notin T_{\mathsf{GS}}$ to internal space and using the properties of the window W_{GS}. The same argument as for the TT tiling gives us

$$\gamma \cdot |z^{\star}| > \ell_{-} \quad \Longrightarrow \quad \epsilon \cdot |z^{\star}| > \ell_{+}$$

and

$$\frac{\gamma}{2} \cdot |z^{\star}| > \ell_{-} \quad \Longrightarrow \quad \frac{\gamma}{2}\sqrt{3} \cdot |z^{\star}| > \ell_{+} \ ,$$

leaving only the conditions for ℓ_{-}. Plugging this condition in Eqs. 4.10 yields

$$\begin{aligned} \gamma \cdot |z^{\star}| > \ell_{-} \quad &\text{if } n(z) = 1 \ , \\ \frac{\gamma}{2} \cdot |z^{\star}| > \ell_{-} \quad &\text{if } n(z) = 2 \ , \end{aligned}$$

which becomes our final condition after transforming everything back to physical space. In particular, we want to point out that, while the scaling factors for the two types of z are different, the direction in which the window is shifted is the same on both cases. ∎

Remark 4.31
We already explained in Remark 3.16 how the star map can be described as linear transformation of our integer coordinates. Another important map implements the change of coordinates from $\mathcal{O}$ to the direct-sum decomposition $\mathfrak{o} \cdot 1 \oplus \mathfrak{o} \cdot \zeta$; see Definition 4.3. If $\mathcal{O} = \mathbb{Z}[\zeta_n]$, $m = \phi(n)$, we can write an element from $\mathfrak{o}$ with $k := \frac{m}{2}$ integer coordinates, i.e.

$$\mathfrak{o} \;=\; \left\{ \sum_{i=0}^{k} \alpha_i \omega^i \;:\; \alpha_i \in \mathbb{Z} \right\}$$

for some ω. This approach is somewhat generic, but in the end we only applied to to the n with $\phi(n) = 4$ and $n = 7$; see the heptagonal case in Section 2.8. We start with $x \in \mathcal{O}$, write

$$x \;=\; \sum_{i=0}^{m-1} \beta_i \zeta_n^i \;=\; \sum_{i=0}^{k-1} \alpha_i \omega^i + \left(\sum_{i=0}^{k-1} \alpha_{i+k} \omega^i \right) \cdot \zeta_n$$

and derive a linear map h, such that

$$h((\beta_0, \ldots, \beta_{m-1})) \;=\; (\alpha_0, \ldots, \alpha_{m-1}) \; .$$

The corresponding matrices for our three cases look as follows.

$$h_{\mathsf{AB}} := \begin{pmatrix} 1 & 0 & -1 & 0 \\ 0 & 0 & 0 & -1 \\ 0 & 1 & 0 & 1 \\ 0 & 0 & 1 & 0 \end{pmatrix}, \; h_{\mathsf{TT}} := \begin{pmatrix} 1 & 0 & -1 & 1 \\ 0 & 0 & 0 & -1 \\ 0 & 1 & -1 & 1 \\ 0 & 0 & 1 & -1 \end{pmatrix}, \; h_{\mathsf{GS}} := \begin{pmatrix} 1 & 0 & -1 & 0 \\ 0 & 0 & 0 & -1 \\ 0 & 1 & 0 & 2 \\ 0 & 0 & 1 & 0 \end{pmatrix},$$

The generator element ω is given by $\sqrt{2}$, τ and $\sqrt{3}$ for AB, TT, and GS respectively. We derived h_{AB}, h_{TT}, h_{GS} and also the maps for the heptagonal case in Section 2.8 by hand. A general algorithm to compute these matrices for arbitrary n, or even just for n prime, would be desirable to explore the effect of rotational symmetry on the radial projection. This possible by observing that $\mathcal{O}$ is a $\mathbb{Z}$-module of rank m, but an $\mathfrak{o}$-module of rank 2. We left this for future work.

Remark 4.32
The approach for the AB, TT, and GS case can in principle be extended to any configuration with a star-shaped, symmetric (around $0_{\mathbb{R}^2}$) window.

4.2. Inflation tilings

If the input vertices belong to a tiling which does not admit a description as in the the previous section, we also need to consider all other vertices of the patch when determining the visibility of a specific vertex. However, if we organise our vertex data appropriately, we can avoid using a brute-force approach.
This visibility test of "non-local" type in particular applies to these cases.

(1) The chiral LB tiling. We use this case to explain the procedure.

(2) The RP tiling, which is a union of cyclotomic model sets with different windows.
(3) All tilings described in Section 4.1 with an origin different from zero.

We assume again that coordinates of the underlying set can be encoded exactly by integer arithmetic. A short remark about the general case can be found at the end of this section.

Procedure 4.33
Consider the LB tiling where the vertices live in $\mathcal{O} = \mathbb{Z}[\zeta_5]$ with origin $x_0 = 0_{\mathbb{R}^2}$. Let $x, y \in \mathcal{O}$ both be non-zero and write

$$x \;=\; x_1 + x_2 \cdot \zeta_5, \quad y \;=\; y_1 + y_2 \cdot \zeta_5$$

with $x_i, y_i \in \mathbb{Z}[\tau]$. We want to determine whether x and y are located on the same ray starting from x_0; see Definition 4.1 for reference. Some preliminary checks are applied first.

(1) If $(\mathrm{sgn}(x_1), \mathrm{sgn}(x_2)) \neq (\mathrm{sgn}(y_1), \mathrm{sgn}(y_2))$ then our statement ("x and y on the same ray") is false.
(2) If $x_1 = 0$, then the statement is only true iff $y_1 = 0$.
(3) The same applies for the combinations (y_1, x_1), (x_2, y_2) and (y_2, x_2).

Assume that some $\lambda > 0$ exists which satisfies $\lambda \cdot x = y$, so

$$\lambda \cdot x_1 \;=\; y_1 \;\wedge\; \lambda \cdot x_2 \;=\; y_2 \;.$$

But after the preliminary checks, we can rewrite this as

$$x_1 \cdot y_2 \;=\; x_2 \cdot y_1 \;,$$

which gets rid of the λ. Since this is multiplication in $\mathbb{Z}[\tau]$, the visibility test only relies on integer arithmetic and hence is exact.
Unfortunately, we would still need to consider all possible combinations of x and y in our patch and apply this test.

Procedure 4.34
The fundamental problem with a test that only uses the angle of a vertex is that the angle φ, as a value in $\mathbb{R}$, can not be encoded exactly. If we have non-zero vertices x and y, the following two situations can therefore happen.

(1) $\varphi(x)$ and $\varphi(y)$ match numerically, but x and y are not on the same ray;
(2) x and y are on the same ray, but $\varphi(x) \neq \varphi(y)$ numerically.

Still, we can use that, if $\varphi(x) \approx \varphi(y)$, x and y are likely candidates to lie on the same ray. Since we only apply a limited amount of steps with approximate arithmetic to compute the angle from our vertex, the error introduced is small. Hence, if $\varphi(x)$ differs from $\varphi(y)$ more than an ϵ depending on the machine precision, we can omit the pair (x, y) for the test described in Procedure 4.33. Taking this into account, we can derive the following algorithm.
We start wit the vertices $X \subset \mathcal{O}$ of our patch and an empty list L. Computational

complexity for insertion and removal of elements in L is $\mathcal{O}(1)$. For each $x \in X$, we compute $\varphi(x)$ and insert the x such that L is ordered with respect to the (approximate) angle.
Now, we iterate over L to remove invisible vertices. For each $\ell \in L$, we collect neighbouring nodes of ℓ which differ at most ϵ for the corresponding angle, i.e.

$$M_\ell \;:=\; \{m \in L \;:\; |\varphi(m) - \varphi(\ell)| \leqslant \epsilon\} \;.$$

Since L is ordered, this amounts to going forward/backward from ℓ a few steps until the difference becomes larger than ϵ. For each pair (ℓ, m), $m \in M_\ell$, we apply the test from Procedure 4.33. If the test is *true* and $\|m\| \geqslant \|\ell\|$ holds, the node m is removed. In case we have $\|m\| < \|\ell\|$, the vertex corresponding to the node m is closer to the origin than ℓ, and therefore should not the removed.
In case we only want to use the vertices as input for radial projection, we can omit the step that uses the length $\|m\|$, since any vertex on the ray is fine. Also note that we only base the insert position on the angle, i.e. L is not radially sorted. It might be worthwhile to explore the performance implications when adding such step.

Remark 4.35
While double-linked lists have constant $\mathcal{O}$-complexity in theory, they come with several drawbacks.

(1) Neighbouring elements of the list can be located at arbitrary positions in (linear) system memory. This becomes a problem, especially when the list grows larger, as we explain in Section 4.3 below.
(2) There is some overhead for linking together nodes in the list. If the user data, for us the coordinates of an element $x \in X$, is small in comparison to the link data, performance begins to suffer.

The latter point became critical in Chapter 6 where we saw a quadratic increase in vertex count to obtain good histogram quality.
In Example 3.23, we concluded that each vertex can be encoded with 8 bytes. On the typical *x86-64* [1] architecture, the aforementioned link data is already $2 \times 8 = 16$ bytes, which makes it obvious that the overhead is significant. While the approach in Procedure 4.34 certainly works and is robust, it also is vastly slower than the local tests.

Remark 4.36
In principle the approach from Procedure 4.33 also gives us a test for the most general case of $\mathbb{R}^2 \simeq \mathbb{C}$. Let $x, y \in \mathbb{C}$, then write $x = x_1 + x_2 \cdot \mathrm{i}$, same of y, apply the preliminary checks and again reformulate the condition to

$$x_1 \cdot y_2 \;=\; x_2 \cdot y_1 \;.$$

---

[1] The 64-bit version of the `x86` processor instruction set. It is present on all modern desktop personal computers since around 2005. Native data size is 8 bytes.

However, now all values in this equation are reals, which we can not encode exactly in general. It might be possible, with details depending on the tiling considered, to derive some error treshold ϵ for which the above check works, i.e.

$$|x_1 \cdot y_2 - x_2 \cdot y_1| \ < \ \epsilon \ ,$$

as long as the patch size does not exceed a critical size.
With the abundance of tilings which admit integer coordinisation, we left this problem for future work.

4.3. Fundamental domain reduction

We have seen the two extreme cases of visibility computation in Sections 4.1 and 4.2. The first one is fast, while the second one is slower, usually by several orders of magnitudes. We want to briefly discuss some techniques to optimise the algorithms in the previous section. In particular we want to make them more "friendly" for the cache prefetcher; see below.
Current computer architectures feature a multitude of storage facilities which can be ordered by latency. Processor registers can be accessed in one cycle, cache usually takes around 10 cycles, while system memory access takes several 100 cycles [20, 22]. The cache prefetcher predicts access to system memory and preloads data into the cache while the processor is busy with computations. Our goal here is to improve the prediction rate of the prefetcher by using a linear access pattern in the algorithm, opposed to a random access pattern.

Procedure 4.37
We assume that our vertices live in the ring of cyclotomic integers with parameter $n = 8$, i.e. we can decompose $\mathcal{O}$ into

$$\mathcal{O} \ = \ \mathfrak{o} \cdot 1 \oplus \mathfrak{o} \cdot \zeta \quad \text{with} \quad \mathfrak{o} \ = \ \mathbb{Z}[\sqrt{2}].$$

The fundamental unit in this case is $\epsilon = 1 + \sqrt{2}$. Let $x \in \mathfrak{o}$ with $x > 0$, then we can further decompose x into

$$x \ = \ x_{\mathsf{fund}} \cdot \epsilon^k \quad \text{where} \quad x_{\mathsf{fund}} \in [1, \epsilon) \cap \mathfrak{o}, \ k \in \mathbb{Z}.$$

We call $[1, \epsilon)$ the fundamental domain of $\mathfrak{o}$ (we omit the $- \cap \mathfrak{o}$ part for simplicity). Now take $z \in \mathcal{O}$ and consider its coordinates x and y. We ignore the signs of the coordinates for now and assume everything is positive. First, choose a positive (always possible since -1 is a unit in $\mathfrak{o}$) GCD g of x and y, i.e. $g := \gcd_{\mathfrak{o}}(x, y)$ with $g > 0$, and define

$$\tilde{x} \ := \ \frac{x}{g}, \qquad \tilde{y} \ := \ \frac{y}{g} \ .$$

Proceed by computing $x_0 := \tilde{x}_{\mathsf{fund}}$ and the corresponding k and apply the transformation to $\tilde{y}$ as well, i.e.

$$\tilde{y} \ \mapsto \ \tilde{y} \cdot \epsilon^{-k} =: y_0 \ .$$

This procedure yields a new element z_{can} in $\mathcal{O}$ with coordinates x_0 and y_0, which is just a rescaled copy of z, i.e. $z_{\mathsf{can}} \cdot (\epsilon^k g) = z$. We call z_{can} the *canonical representative* (crep) of the $\mathcal{O}$-ray spanned by z.
If one of the coordinates x, y should be negative, we store the sign, work with the absolute value and restore the sign at the end. The reason for this is to avoid changing the direction of the ray defined by z.

Remark 4.38
To compute the values $\tilde{x}, \tilde{y}$ above, we only need integer arithmetic. Given $a + b\sqrt{2}$ and $c + d\sqrt{2}$, we compute

$$\frac{a + b\sqrt{2}}{c + d\sqrt{2}} = \frac{ac - 2bd}{c^2 - 2d^2} + \frac{bc - ad}{c^2 - 2d^2}\sqrt{2} \,.$$

Since we divide with the GCD in $\tilde{x}$, $\tilde{y}$, the fractions above are again integers. In particular, this gives us an efficient division in $\mathfrak{o}$, a procedure we need later in Chapter 7.

Lemma 4.39
The decomposition for $\mathfrak{o}$ given in Procedure 4.37 always exists and is unique, i.e. $x_{\mathsf{fund}}, y_{\mathsf{fund}}$ and k_x, k_y match iff x and y are equal.
Since distinct GCDs g only differ by multiplication of a unit, the same properties hold for the crep z_{can}.

Proof. Let again $x \in \mathfrak{o}$ with $x > 0$. Then, obviously, there always exists a decomposition $x = x_{\mathsf{fund}} \cdot \epsilon^k$, without further conditions on x_{fund}. Applying the logarithm yields the equation

$$\log(x) = \log(x_{\mathsf{fund}}) + k \cdot \log(\epsilon) \,,$$

from which we can recover $\log(x_{\mathsf{fund}})$ as the remainder of a modulo operation. The exponent k then computes as

$$k = \lfloor \frac{\log(x)}{\log(\epsilon)} \rfloor \,,$$

which leaves $\log(x_{\mathsf{fund}})$ in the interval $[0, \log(\epsilon))$. Removing the logarithm, we end up with $x_{\mathsf{fund}} \in [1, \epsilon)$ as intended. By construction x_{fund} is an element in $\mathfrak{o}$. In particular, this shows that the decomposition is unique. ■

Remark 4.40
For actual implementation, it is advantageous to catch the case $x \in \mathfrak{o}^\times$ early and to compute k by rounding to the nearest integer instead of using the floor function, improving numerical stability in the process.

Remark 4.41
The fundamental domains for the other cyclotomic cases are $[1, \tau)$ and $[1, 2 + \sqrt{3})$ for $\mathbb{Z}[\tau]$ and $\mathbb{Z}[\sqrt{3}]$, respectively.

Lemma 4.42
Let $z, w \in \mathcal{O}$. Then, z and w are located on the same ray (with zero as origin) iff their creps agree, i.e. $z_{\mathsf{can}} = w_{\mathsf{can}}$.

Proof. Being vertices on the same ray amounts to the following property

$$\exists\, \lambda \in \Bbbk \cap (0, \infty) \;:\; \lambda \cdot z = w \;,$$

where we write the scaling factor λ as maximally reduced fraction, i.e. $\lambda = \lambda_1/\lambda_2$ with λ_1, λ_2 coprime elements from $\mathfrak{o}$. Consider the side $\tilde{z} := \lambda_1 \cdot z$ for now. Since $\gcd_{\mathfrak{o}}(ca, cb) \equiv \gcd_{\mathfrak{o}}(a, b)$ we also have $z_{\mathsf{can}} = \tilde{z}_{\mathsf{can}}$. The same applies for the other side of the equation.
$\underline{\Longrightarrow}$: Assume that we have

$$\lambda_1 \cdot z \;=\; \lambda_2 \cdot w \;,$$

then simply apply $(\cdot)_{\mathsf{can}}$ on both sides.
$\underline{\Longleftarrow}$: Here we first write $z_{\mathsf{can}} \cdot (\epsilon^{k(z)} g(z)) = z$ and w analogously. The factor λ is then given by

$$\lambda \;=\; \epsilon^{(k(z)-k(w))} \frac{g(z)}{g(w)} \;.$$

■

Remark 4.43
When working with arrays of data and applying some transformation to each element, we can either create a new array in the process, or replace the processed element with the output. We call the latter option *inplace* transformation.
The inplace approach is only sensible if the size (in bytes) of the output element is equal to or smaller than that of the input element.

Procedure 4.44
Let $X \subset \mathcal{O}$ be the set of vertices we want to process and consider X as an array of elements in system memory, i.e. write

$$X \;=\; \{x_1, \ldots, x_N\} \quad \text{with} \quad N = |X| \;.$$

We create a new array Y by iterating over the $x \in X$ and computing x_{can} together with the GCD g and exponent k as given in Procedure 4.37. The corresponding element that is stored in Y is the tuple (x_{can}, g, k). By defining a lexicographic ordering on Y through

$$(x_{\mathsf{can}}, g(x), k(x)) \leqslant (y_{\mathsf{can}}, g(y), k(y)) \quad \Longleftrightarrow \quad x_{\mathsf{can}} \leqslant_{\mathsf{lex}} y_{\mathsf{can}} \;,$$

we can apply inplace sorting to Y. Then, elements living on the same ray are adjacent in the sorted list. The relation $\leqslant_{\mathsf{lex}}$ is the lexicographic ordering on $\mathbb{Z}$-tuples explained in Procedure 3.18.
Next, we need to determine which element on a given ray is closest to the origin, i.e. is actually visible. We iterate over Y identifying non-trivial rays in the process, i.e. list indices $i < j$ such that the elements y_k with $i \leqslant k \leqslant j$ have the same crep entries. The element in question is the one where $g \cdot \epsilon^k$ is smallest.

Once this "minimal" g and k are found, all elements in the current range are replaced by it. This avoids creating another array to hold the new data. We call this step the *length normalisation.*

The second to last step is inplace removal of duplicate elements in Y, which is again fast since we are already working with a sorted array. Finally, we transform the remaining elements in Y back to their original type, i.e. we map (x_{can}, g, k) to $x_{\mathsf{can}} \cdot (\epsilon^k g)$. Assuming that we no longer need the original data in X, we write the final output to X and deallocate (see Remark 3.1) Y afterwards.

All operations described here access system memory in a linear fashion, providing a good boost of the prefetcher's efficiency.

Remark 4.45
If we are using the visible vertices as input for radial projection, we can skip some fo the steps in Procedure 4.44. Since we are only interested in the angle of a vertex, any vertex on a given ray is fine. Hence, we can omit storing the GCD g and exponent k and skip the length "restoration" step.

In particular, this reduces the memory bandwidth requirements, since elements in X and Y now have the same type (and hence size in bytes). Now, we may apply creps as an inplace transformation.

Remark 4.46
The procedure can also be applied to $\mathcal{O} = \mathbb{Z}[\mathrm{i}]$, which amounts to a more arithmetic way to deal with $\mathbb{Z}^2$. If we have $\mathcal{O} \ni z = x + y \cdot \mathrm{i}$, then we can omit the reduction to the fundamental domain here. We just compute $g := \gcd_{\mathbb{Z}}(x, y)$ and let $x_0 := \frac{x}{g}$, $y_0 := \frac{y}{g}$. The crep of z is now $z_{\mathsf{can}} := x_0 + y_0 \cdot \mathrm{i}$.

Hence, we can also use the algorithm on any subset of $\mathbb{Z}^2$, like the planar chair tiling (see Section 2.7), but also on more general lattice subsets in $\mathbb{R}^2$.

Conclusion 4.47
We have seen that, given a point set with sufficiently nice properties, the description of the subset of visibility points can be done by using only essentially local information of each point. The three tilings which are constructed as a cyclotomic model set, together with the canonical choice of reference point, have this property. As we have seen in Section 2, these cases also show close resemblence to the square lattice on the level of the RPM. We believe that this is not a coincidence, but that the resemblence are "traces" of the higher-dimensions lattice structure (the diagonal embedding in Remark 2.6), that is projected down to $\mathbb{R}^2$.

Since both the algebraic properties of the underlying set, namely the algebraic conjugations, and the shape of the window in internal space determine which points survive after this projection to $\mathbb{R}^2$, the following questions arise naturally.

(1) How robust is the radial projection under deformations, both large and small, of the window?

(2) How important is the symmetry and the star-shape property of the window? Can we generalise our description when dropping e.g. one of the properties?
(3) How does the growing number of conjugations, when increasing the dimensions of the internal space, affect the visibility condition?

In particular, we ask whether there exists a general description of the visible points of a cyclotomic model set, maybe under some restrictions, like a canonical reference point and certain symmetry properties of the window.

CHAPTER 5

Effects of randomisation

As we have seen by now, the structure of the radial projection distribution greatly depends on properties of the input vertex set, which can be algebraic features of underlying inflation rules or also the rotation symmetry with respect to the reference point.
However, all these properties, e.g. the symmetry parameter of the cyclotomic model set, are somehow discrete in nature. In this chapter, we introduce a more continuous degree of freedom into our model and study how the radial projection reacts to changes of the underlying parameter.

Procedure 5.1
Let $p \in (0, 1)$ and consider our basic setup from Procedure 1.1. Assuming that we have constructed the set V_R, we apply the following randomisation procedure to it.
For each $x \in V_R$, we determine via a Bernoulli trial with parameter p (probability of success) if x is kept or removed. We simply write $V_{R,p}$ for a realisation of this procedure. If $n = |V_R|$, then the expected number of points in $V_{R,p}$ is np. We then proceed as usual and project each $x \in V_{R,p}$ to the boundary of the disc $D_R(x_0)$.
We have seen that a fine resolution for the histograms demands a large number of vertices. Therefore, randomisation with small p makes the computations even more demanding, since we have to compensate for the loss of vertices; also compare Remark 3.20.
As the randomisation happens after the visibility computation, we denote this *post*-randomisation procedure as α-thinning (α-thn).

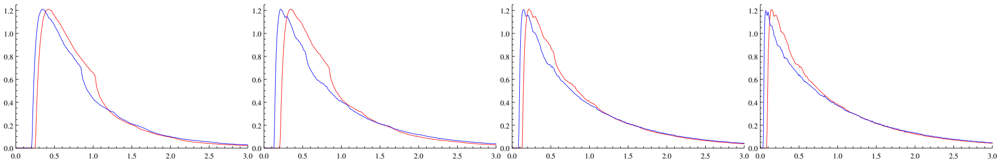

Figure 5.1. Radial projection for α-thn applied to $\mathbb{Z}^2$ with $p \in \{0.85, 0.7, 0.45, 0.3, 0.15\}$ (from left to right).

Thinning is an established operation, usually applied to point process in order to create a new processes; compare [15, Ch. 5.1] for details.

Remark 5.2
We have combined the approximations pairwise in Fig. 5.1 to make it easier for the reader to see the differences. By pairwise combination we mean that the individual frames (from left to right) show $\{0.85, 0.7\}$, $\{0.7, 0.45\}$, $\{0.45, 0.3\}$ and $\{0.3, 0.15\}$ respectively. The first entry is displayed in red, the second entry in blue. We use this visualisation approach for all the coming figures.

Remark 5.3
Choose the $\mathbb{Z}^2$ lattice as the underlying set. Then, with this approach, we expect a transition of the radial projection from $\mathbb{Z}^2$ to Poisson as $p \to 0$. This assumption seems plausible, since we are now essentially looking at a lattice approximation of the Poisson case. Also the numerics, see Fig. 5.1, support this.

We are to going to see that the choice to randomise **after** determination of visibility affects the dependence of the resulting distribution from the parameter p. A different approach is the following one.

Procedure 5.4
Again we start with a $p \in (0, 1)$ and the ingredients from Procedure 1.1, however we move visibility computation back as far as possible.
First, we intersect our disc of radius R and the vertex set

$$S_R \;:=\; S \cap D_R(x_0)$$

and then apply the Bernoulli thinning to it. Denote the resulting set as $S_{R,p}$ and proceed by isolating the visible $x \in S_{R,p}$ and projecting them.
We denote this *pre*-randomisation approach as ω-thinning (ω-thn) for reasons explained in the previous definition.

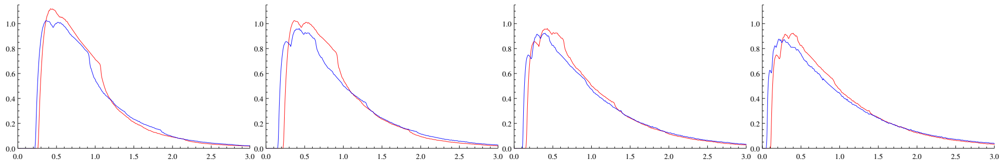

Figure 5.2. Radial projection for ω-thn applied to $\mathbb{Z}^2$ with $p \in \{0.85, 0.7, 0.45, 0.3, 0.15\}$ (from left to right).

The interpolatory behaviour here is obviously different from the one in Fig. 5.1. Notable is that here the histogram height decreases for $p \to 0$, while for α-thn it mostly stays constant.

Remark 5.5
The main difference between the two randomisation approaches is that, in Procedure 5.1, we essentially randomise "directions" in the vertex set, while pre-randomisation introduces some weighting for the directions.

To see this, let $x \in S_R$ and consider all vertices on the ray spanned by x, i.e

$$\vec{x} \;:=\; \{\lambda \cdot x \;:\; \lambda > 0\} \;\cap\; S_R \;.$$

Then, we can define an equivalence relation by

$$x \;\sim\; y \quad \Longleftrightarrow \quad \vec{x} \;=\; \vec{y}\;,$$

where the $\vec{x}$ are the corresponding equivalence classes.
If we apply α-thn, this amounts to selecting one representative from each class and randomising the resulting set. Each representative has the same probability $1 - p$ to be removed.

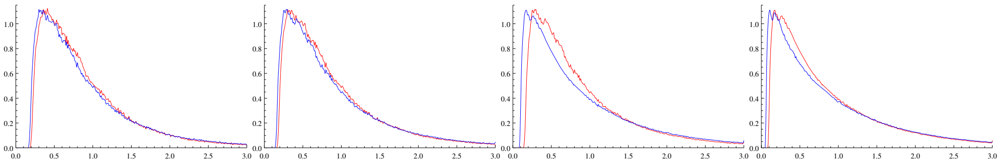

Figure 5.3. Radial projection for α-thn applied to AB with $p \in \{0.85, 0.75, 0.65, 0.4, 0.25\}$ (from left to right).

With ω-thn, we randomise in each class first before a representative is selected. But now a class can end up empty after randomisation, i.e. it does not contribute to the final set of representatives. The probability that a class $\vec{x}$ becomes empty, depends on the number of vertices $|\vec{x}|$ in it. Hence, the ω-thn approach favors directions in our vertex set which feature a high point density. See [43] for a discussion about these high density directions in 2- and 3-dimensional tilings.

Remark 5.6
The ω-thn approach is computationally more expensive since the randomisation destroys the structure that allows for a local visibility test; see Chapter 4.

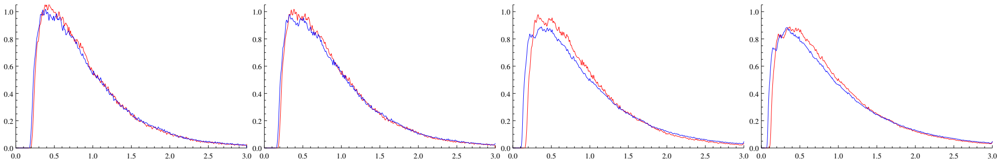

Figure 5.4. Radial projection for ω-thn applied to AB with $p \in \{0.85, 0.75, 0.65, 0.4, 0.25\}$ (from left to right).

We also point out that the radial projection of the randomisations, almost surely in the limit $R \to \infty$, only depends on the parameter p, and not on the individual realisation of our sequence of Bernoulli trials.

A first observation in Figs. 5.1 to 5.4 is that there seems to be a continuous dependence between the thinning parameter p and the resulting histogram. In particular, this applies to some of the key properties, like the size of the gap, the position of the histogram peak and the height of the peak. If we consider just the $\mathbb{Z}^2$ case, it looks plausible, even more by looking at the fine-grained interpolation, see [33], that the bulk-tail transition changes gradually as well.
While extracting the gap size and peak position from our numerical data is unambiguous, tracking the aforementioned transition for the $\mathbb{Z}^2$ case relies on visual inspection. Hence, we focus on gap and peak first.

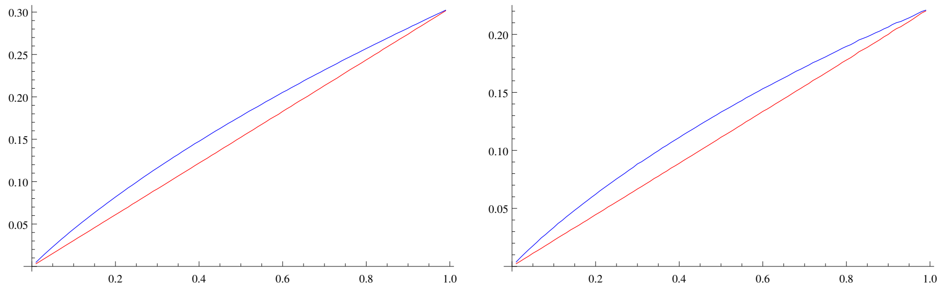

Figure 5.5. Gap position for the $\mathbb{Z}^2$ lattice (left) and the AB tiling (right) as function of p (α-thn in red, ω-thn in blue).

Note that the curves in Fig. 5.5 were created from discrete data points, only applying linear interpolation between the points. No smoothing or filtering was done here.
Our assumption about the continuity of the gap size in p seems to be supported by the data in Fig. 5.5, and also in Fig. 5.6 below. But we can see even more.

Theorem 5.7
Let (S, x_0) be a point set together with a reference point such that the limit measure ν of the radial projection exists and has gap $\tilde{g} > 0$, i.e.

$$\lim_{R \to \infty} \nu_R \;=\; f \cdot \mu, \qquad \text{(weak convergence of measures)}$$

with f a continuous density, μ the Lebesgue measure on $\mathbb{R}_+$ and

$$\tilde{g} \;=\; \inf \{ x > 0 : f(x) > 0 \} \,.$$

We consider the α-thn setup from Procedure 5.1 and assume that for each $p \in (0,1)$ the corresponding measure ν_p exists in the usual "almost sure" sense. By computing the gap for each ν_p, we construct the map

$$\mathrm{g} : (0,1) \longrightarrow \mathbb{R}_+ \,.$$

Then, g is linear, i.e. we have $\mathrm{g}(p) = p \cdot \tilde{g}$, and $\lim_{p \to 1} g(p) = \tilde{g}$, again almost surely.

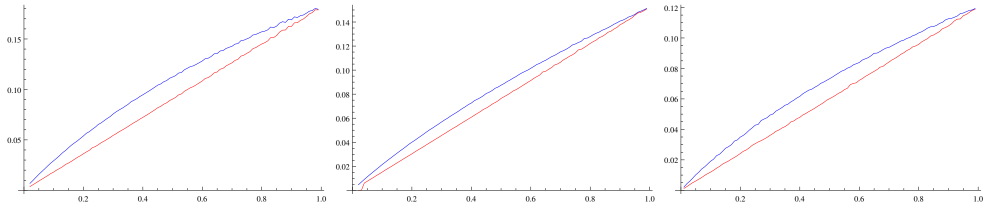

Figure 5.6. Gap position for the TT, GS and RP tiling (from left to right) as function of p (α-thn in red, ω-thn in blue).

Remark 5.8
In Fig. 5.5, we see that for the α-thn setup, the data for $\mathbb{Z}^2$ nicely fit a linear function (with slope $\frac{3}{\pi^2} \approx 0.304$), while for ω-thn the behaviour is more complex. The positions there can be approximated quite well with a cubic polynomial $at^3 + bt^2 + ct$ with coefficients

$$a := 0.0895816, \ b := -0.233757, \ c := 0.450107 \ .$$

A linear behaviour cannot be expected, because of the weighting of high density directions mentioned in Remark 5.5. Still, it would be interesting to find out why the behaviour is approximately cubic – a property that also applies to AB, TT and our other cases.

Table 5.1. Coefficients of the cubic interpolation polynomials for the α-thn setup.

tiling	a	b	c
AB	0.345455	−0.194115	0.0722168
TT	0.302713	−0.18851	0.0683979
GS	0.217939	−0.10497	0.0401906
RP	0.195998	−0.11941	0.0444118

As preparation for the proof of Theorem 5.7, we introduce some additional notation. First we replace the $\mathbb{R}$ indexing of the objects involved, e.g. the measure ν_R with a $\mathbb{N}$ indexing.

Definition 5.9
Consider the set V_R for some $R > 0$ with $N := |V_R|$. Since the underlying set is assumed to be locally finite, there exists $\epsilon > 0$ such that

$$N_\epsilon \ := \ |V_{R+\epsilon}| > N$$

and this ϵ is minimal, i.e. every other $\tilde{\epsilon} < \epsilon$ satisfies $N_{\tilde{\epsilon}} = N$. In other words, if we increase the radius of our disc by a small amount, only a few vertices are added.
Let R_0 be the smallest radius such that $|V_{R_0}| \neq 0$, define $R_1 := R_0 + \epsilon$ with ϵ

constructed as above and iterate.
This construction yields a sequence $(R_i)_{i \geqslant 0}$, which we employ for indexing our sets V_i and consequently also the measures ν_i. We also write $N_i := |V_{R_i}|$. Because of symmetry properties, it might not always be possible to have $N_{i+1} = N_i + 1$.

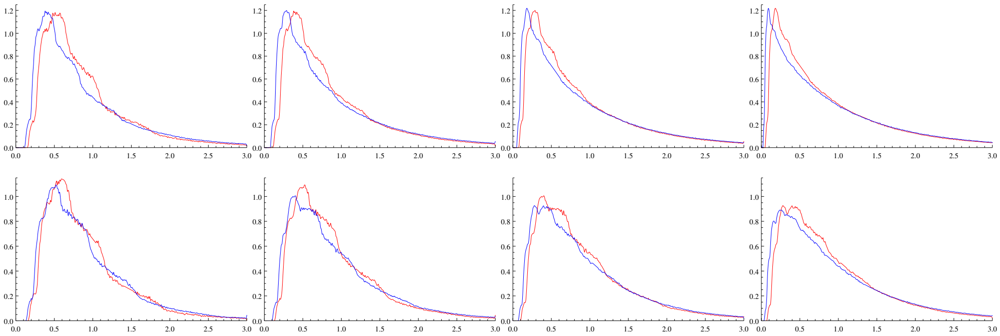

Figure 5.7. Radial projection for α-`thn` (top), ω-`thn` (bottom) applied to `TT` with $p \in \{0.85, 0.65, 0.45, 0.3, 0.15\}$ (left to right).

Remark 5.10

For Theorem 5.7, we assume another mild condition. Define g_i as the minimal spacing of V_i. Then, we assume

$$\lim_{i \to \infty} g_i = \tilde{g}$$

to hold. We also introduce $g_{i,p}$ as the minimal spacing for $V_{i,p}$, the randomised version of V_i.

Proof of Theorem 5.7. Consider the set $V_{i,p}$ again. Then, $\mathbb{E}(|V_{i,p}|) = pN_i$ and hence we encounter an additional factor of p when rescaling the corresponding set of angles, i.e

$$d_j = \overline{\varphi}_{j+1} - \overline{\varphi}_j = c_R \cdot (\varphi_{i+j} - \varphi_j) \approx p \cdot \frac{N_i - 1}{2\pi} \cdot (\varphi_{j+1} - \varphi_j) \ ,$$

where we have highlighted the factor in red. We now show that, by omitting the factor p during this step, we get

$$\lim_{R \to \infty} g_{R,p} = g_0 \quad \text{almost surely} \ .$$

This means that the linear behaviour of the gap is only due to the rescaling applied. The idea now is the following.

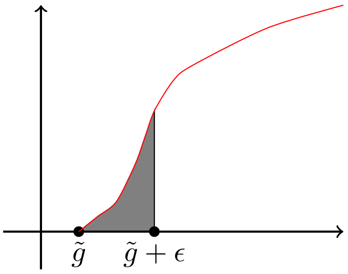

Figure 5.8. Area under the density $f(x)$ that contributes to our gap.

The spacings d_j that comprise the grey area in Fig. 5.8 are the ones that "define" the gap size, in the following sense. Consider a small ϵ and ask when the gap size changes. This is only the case when the thinning process removes all the spacings in the aforementioned area. We show that no matter how small the area is, thinning never removes enough elements to actually change the minimal spacing.

For the first direction, we note that

$$g_{i,p} \geqslant g_i \quad \text{with probability } 1 + \mathrm{o}(c^i)$$

for some constant $c > 0$. Hence, using Remark 5.10, we get

$$\liminf_{i\to\infty} g_{i,p} \geqslant \tilde{g} \quad \text{almost surely} .$$

For the other direction, choose $\epsilon > 0$ and define $G := [\tilde{g}, \tilde{g}+\epsilon]$, the interval from Fig. 5.8. Then, we have

$$\nu_i(G) \;\longrightarrow\; \int_{\tilde{g}}^{\tilde{g}+\epsilon} f(t)\mathrm{d}t \;=:\; C_\epsilon \quad \text{for} \quad i \to \infty . \tag{5.1}$$

Now, rewrite the left-hand side of Eq. (5.1) as

$$\frac{1}{N_i} \left|\{j \;:\; \overline{\varphi}_{j+1} - \overline{\varphi}_j \in [\tilde{g}, \tilde{g}+\epsilon]\}\right| ,$$

where the angles $\overline{\varphi}_j$ emerge from the set V_i. Let us denote this set of indices as $\mathrm{J}(V_i)$ and assume that $\mathrm{J}(V_i)$ contains M_i elements. Choose an index j that contributes to $\mathrm{J}(V_i)$, this j also contributes to $\mathrm{J}(V_{i,p})$, whence with probability p^2.

We now need the following properties.

(1) There exists K_0 such that $M_i \geqslant \frac{1}{2} C_\epsilon N_i$ for all $i \geqslant K_0$.
(2) There exists $\tilde{\mathrm{J}}(V_i) \subset \mathrm{J}(V_i)$ such that

$$j_1, j_2 \in \tilde{\mathrm{J}}(V_i) \implies |j_1 - j_2| \geqslant 2 \quad \text{and} \quad |\tilde{\mathrm{J}}(V_i)| \geqslant \frac{M_i}{2} .$$

The first property is just the convergence in Eq. (5.1), the second one results from thinning out $\mathrm{J}(V_i)$ appropriately.
Using these results, we can write

$$\begin{aligned}\mathbb{P}\left(\mathrm{J}(V_{i,p})=\varnothing\right) &\leqslant \mathbb{P}\left(\forall\, j\in \mathrm{J}(V_i)\ :\ \overline{\varphi}_{j+1} \text{ is removed } \vee\ \overline{\varphi}_j \text{ is removed}\right)\\ &\leqslant \mathbb{P}\left(\forall\, j\in \tilde{\mathrm{J}}(V_i)\ :\ \ldots\right)\\ &= \prod_{j\in\tilde{\mathrm{J}}(V_i)} \mathbb{P}\left(\overline{\varphi}_{j+1} \text{ is removed } \vee\ \overline{\varphi}_j \text{ is removed}\right)\\ &= \prod_{j\in\tilde{\mathrm{J}}(V_i)} (1-p^2) \ = \ (1-p^2)^{\left|\tilde{\mathrm{J}}(V_i)\right|}\ ,\end{aligned}$$

where we have used the independence of the Bernoulli trials on $\tilde{\mathrm{J}}(V_i)$. Hence, we can now bound the probability by

$$\mathbb{P}\left(\mathrm{J}(V_{i,p})=\varnothing\right)\leqslant (1-p^2)^{\frac{M_i}{2}} \leqslant (1-p^2)^{\frac{C_\epsilon N_i}{4}} \text{ for } i\geqslant K_0$$

and apply *Borel–Cantelli* to the series $\sum_{i=0}^{\infty}\mathbb{P}\left\{\mathrm{J}(V_{i,p})=\varnothing\right\}$. This yields

$$\mathbb{P}\left(\mathrm{J}(V_{i,p})=\varnothing \text{ for infinitely many } i\right)=0\ ,$$

or, phrased in terms of the minimal spacing,

$$\mathbb{P}\left(g_{i,p}\geqslant \tilde{g}+\epsilon \text{ for infinitely many } i\right)=0\ .$$

So, almost surely, $\limsup_{i\to\infty} g_{i,p}\leqslant \tilde{g}+\epsilon$ and since $\epsilon>0$ was arbitrary, we have

$$\limsup_{i\to\infty} g_{i,p}\leqslant\tilde{g} \quad \text{with probability } 1\ .$$

Hence $\liminf g_{i,p}$ and $\limsup g_{i,p}$ match, which concludes the proof. ■

Remark 5.11
So far we could only prove that the gap position behaves linear when applying α-thn. The numerical data however suggests that this linearity might also extend to other key positions, in particular the position of the peak of the bulk.

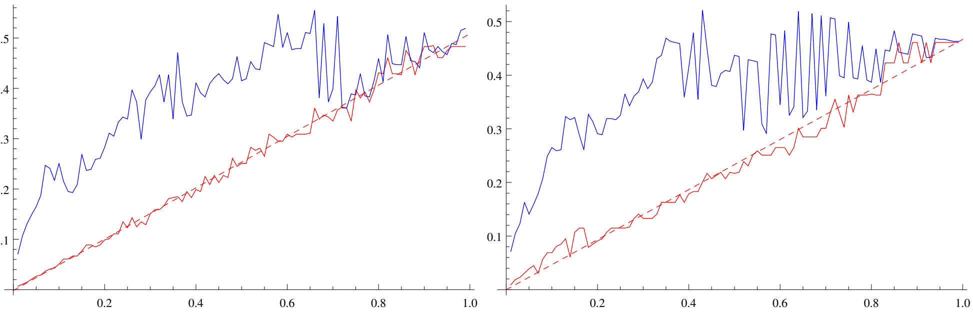

Figure 5.9. Peak position for the $\mathbb{Z}^2$ lattice (left) and the AB tiling (right) as function of p.

In Fig. 5.9 we indicate the α-thn data in red, and the ω-thn data in blue. Also, we include a linear regression for the α-thn data as a dashed line. We believe that the linearity of the peak could be proofed by using a similar, two-sided, argument as in the proof for Theorem 5.7.

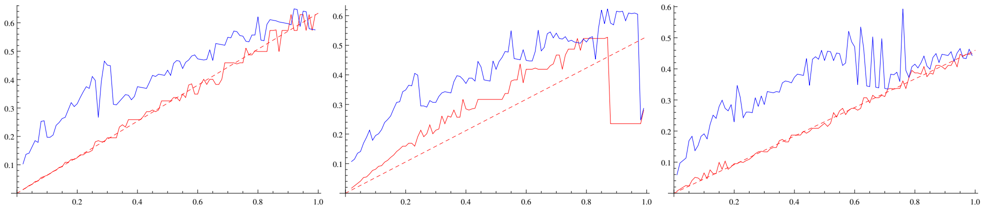

Figure 5.10. Peak position for the TT, GS and RP tiling (from left to right) as function of p.

Again, we can observe that the behaviour for ω-thn is, like the gap position already, much more complex. Also, the quality of the data for the GS tiling quickly deteriorates for $p > 0.9$.

Example 5.12
Before closing this chapter, we compile the interpolation figures for the remaining tilings. One can see that the difference between α-thn and ω-thn is also present here.

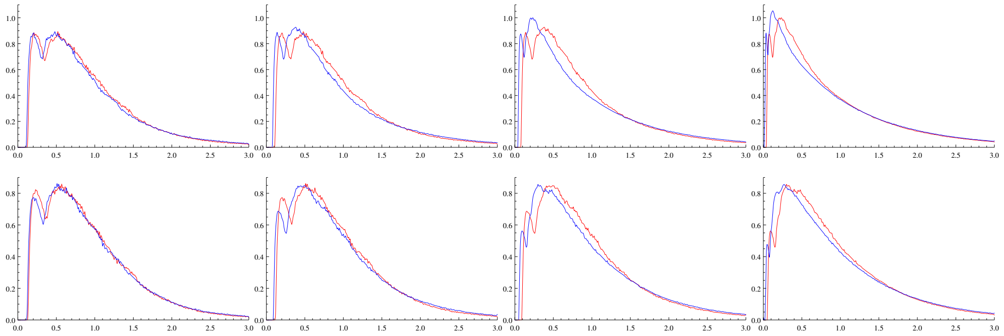

Figure 5.11. Radial projection for α-thn, ω-thn applied to GS with $p \in \{0.85, 0.75, 0.55, 0.3, 0.15\}$ (left to right).

Another somewhat surprising observation is that various structural features of the radial projection seem “immune” to randomisation. A good example is the GS tiling, where we have two local maxima in the bulk section. Even with small values of p (we went as low as $p = 0.05$ and zoomed into the area near zero), this structure is retained.

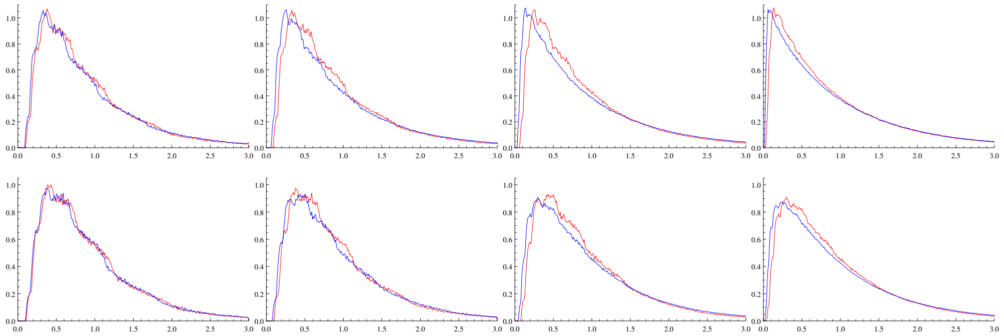

Figure 5.12. Radial projection for α-thn, ω-thn applied to RP with $p \in \{0.85, 0.75, 0.55, 0.3, 0.15\}$ (left to right).

Remark 5.13

One aspect to consider for future investigations is the behaviour of the tail under randomisation. We know that the tail for the $\mathbb{Z}^2$ case is determined by a power law; see Section 2.5. For the Poisson distributed points, we obviously have a exponential tail.

However, if randomisation is universal, in the sense that, no matter which tiling we consider, the limit $p \to 0$ always recovers the radial projection of the Poisson case, the question arises where the power law transitions into an exponential decay. We tried a simple ansatz using linear superposition of the two types, but the behaviour seems to follow a more sophisticated rule.

Also, if the behaviour is universal, then Fig. 5.11 suggests that the transition to Poisson happens quite late in the process, i.e. when $p \approx 0$.

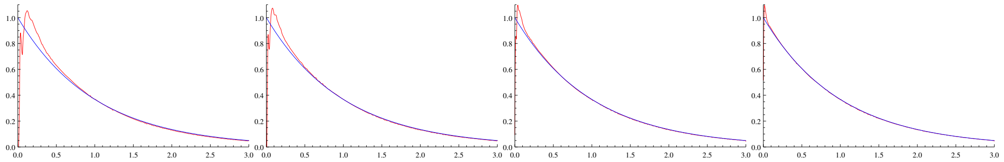

Figure 5.13. Radial projection for α-thn applied to the GS tiling with $p \in \{0.15, 0.10, 0.05, 0.02\}$ (left to right) with $\exp(-t)$ reference overlayed in blue.

Conclusion 5.14

Both the α-thn and ω-thn approach have enabled us to continuously “inject” disorder into the original point sets, hence satisfying our initial goal to introduce another degree of freedom to our model. We have seen that, for both approaches, small changes in the randomisation parameter p also result in small changes of the radial projection. We believe that this is another indicator that RPM is suitable for detecting order properties of a point set. In the case of α-thn we have seen, that the aforementioned changes seem to be mostly linear in nature. A good candidate to check how far this linearity reaches (we suspect that it also governs the position of the regime change), would be $\mathbb{Z}^2$, since all key positions (peak of the bulk, transition between bulk and tail section, etc.) are explicitly known there.

It is still unclear how to quantify the non-linear behaviour of the ω-thn approach. From Remark 5.5, we know that the main argument in the proof of Theorem 5.7, the isolation of the parameter p from the spacings d_j, does not hold anymore. We would first need to understand how $\mathbb{E}(|V_{i,p}|)$ behaves here, and the numerics, see in particular Table 5.1, indicate that this behavior is not universal, but unique to each point set.

CHAPTER 6

Second-order spacings

As we indicated in Procedure 1.1, the choice to inspect the distance between consecutive angles

$$d_i \;=\; \overline{\varphi}_{i+1} - \overline{\varphi}_i$$

is motivated by the concept of two-point correlations. We now want to ask the question how much influence d_i has on its neighbouring spacings.

Procedure 6.1
We re-use the setup from Procedure 1.1, but instead of the probability measure ν_R on $\mathbb{R}$ we consider

$$\sigma_{R,k} \;:=\; \frac{1}{m}\sum_{i=1}^{m} \delta_{(d_{i+k},d_i)}$$

for a fixed $k \in \mathbb{N}$ and $m = n - 1 - k$. Here, $\delta_{(x,y)}$ denotes the Dirac measure at position (x, y). This discrete probability measure on $\mathbb{R}^2$ encodes the "second-order" spacings with step size k. We are mostly going to take a look at the case $k = 1$ which we then simply denote as second-order spacings. From $\sigma_{R,1}$, we can extract the information how the neighbourhood of a radial spacing looks like. For example, we can ask how often it happens that large spacings pair up with a spacing of similar size.
A slightly different version to compute $\sigma_{R,k}$, which is mostly useful for larger k, uses $d_{i+k \bmod n-1}$ instead of d_{i+k} and $m = n - 1$. The wrap-around obviously becomes less interesting for larger radii R.

Remark 6.2
Similar to the first-order spacings, the analysis of $\nu_{R,k}$ requires the computation of histograms with a fine resolution, now resulting in an graph over $\mathbb{R}^2$, i.e. some object in $\mathbb{R}^3$ after visualisation. All meshes from this chapter can also be found online [33].
The meshes are stored as compressed *Wavefront OBJ* files, a format which most mesh viewers should be able to display.

Remark 6.3
Histogram binning is again done using uniform sampling; compare Procedure 2.9. We choose a binning region $[a_x, b_x) \times [a_y, b_y)$ and step sizes s_x, s_y, which then defines the number n_x, n_y of bins in x- and y-direction, respectively,

$$n_x \;:=\; \lfloor (b_x - a_x)/s_x \rfloor \quad\text{and}\quad n_y \;:=\; \lfloor (b_y - a_y)/s_y \rfloor \;.$$

The input to our binning algorithm is the collection Δ of δ measures from Procedure 6.1 and the output is a 2-dimensional array of integers together with the number of input data that fall into the binning region. For the code we interpret Δ as an array containing the positions (x, y) of the measures $\delta_{(x,y)}$. Array indexing starts at 0 as usual.

```
input  : $\Delta$ of Dirac measures
output : integer bins$[n_x][n_y]$, integer catched
initialize all entries of bins to 0;
initialize catched to 0;
foreach $(x, y) \in \Delta$ do
    if $x \notin [a_x, b_x) \ \vee \ y \notin [a_y, b_y)$ then
        skip;
    $i_x \leftarrow (x - a_x)/s_x$;
    $i_y \leftarrow (y - a_y)/s_y$;
    bins$[i_x][i_y] \leftarrow$ bins$[i_x][i_y] + 1$;
    catched $\leftarrow$ catched $+ 1$;
end
```

Algorithm 3: Histogram binning for second-order spacings.

The resulting array can then be e.g. used as input for a 2-dimensional bar diagram visualisation. To end up with an (approximated) density of a probability distribution, we need to rescale with

$$\lambda \ = \ (N \cdot s_x s_y)^{-1} \ ,$$

where $N = |\Delta|$ is the amount of input data. The volume from all bars in the visualisation does not sum up to 1 though, since we almost always have data outside of the binning region.

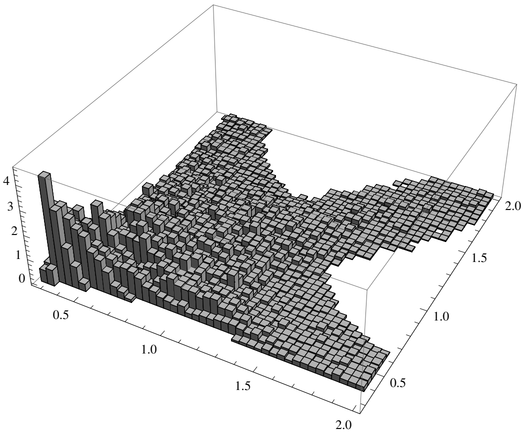

Figure 6.1. Histogram of the second-order spacings for the $\mathbb{Z}^2$ lattice, visualised as 3-dimensional bar diagram.

If the input data allows for a fine sampling resolution, i.e. s_x, s_y small, then visualisation using bars becomes less favorable. Each bar has 6 faces and 12 edges, some of which might be occluded, resulting in a large amount of render primitives as one can see in Fig. 6.1. A more elegant solution is to create a 3-dimensional mesh from the output data by using the midpoint of the bin as (x, y) coordinate and the number of points inside as height, i.e. the z coordinate (after applying rescaling with λ as before).

Remark 6.4
One feature of the distribution of the first-order spacings for model sets of cyclotomic type is the existence of a gap. If d_i are the spacings, we have $g \leqslant d_i$ for some gap value $g > 0$, which is independant of the radius R. If this situation occurs for some input set, then the second-order spacings are going to have some "gap area" as well, since no $\delta_{(d_{i+k}, d_i)}$ exist for $d_{i+k} < g$ or $d_i < g$.

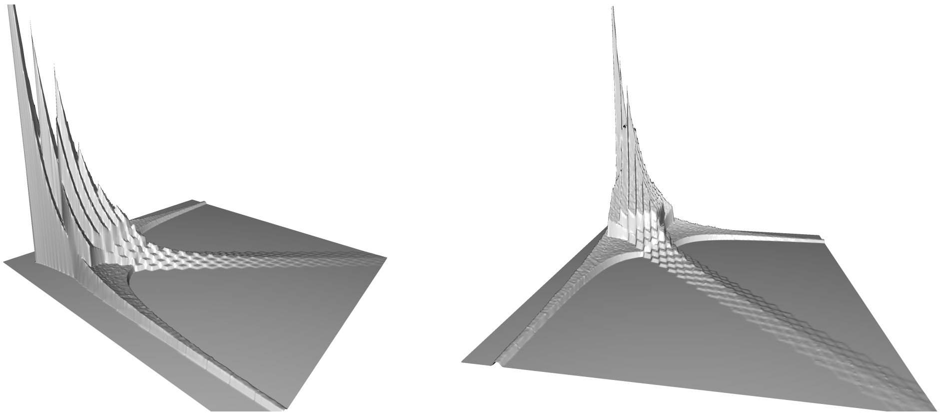

Figure 6.2. High-resolution histogram for the $\mathbb{Z}^2$ lattice, visualised as a 3-dimensional mesh.

In Fig. 6.2, we can see this induced gap as an empty area framing the mesh near the x- and y-axis. But already in this simple example of the $\mathbb{Z}^2$ lattice, we see more area where all mass of the distribution is absent.

If the first-order spacings feature a gap, we denote the induced gap as *outer* gap area. All other areas with no mass are denoted as *inner* gap areas. Obviously, the latter is the more interesting object to study.

We want to point out that identification of inner gap areas from a mesh visualisation can be deceptive. If the number of samples N is sufficiently large, i.e. the factor λ is small, discerning between a zero and an almost-zero point count in some bin is error-prone. Hence, we apply an additional analysis pass to the binning output before constructing the mesh. This pass just consists of marking empty bins and hence also uses the output from Algorithm 3. This gives us a visualisation of the areas with zero mass and can be used to determine “stability” of such areas by computing them with different radii R.

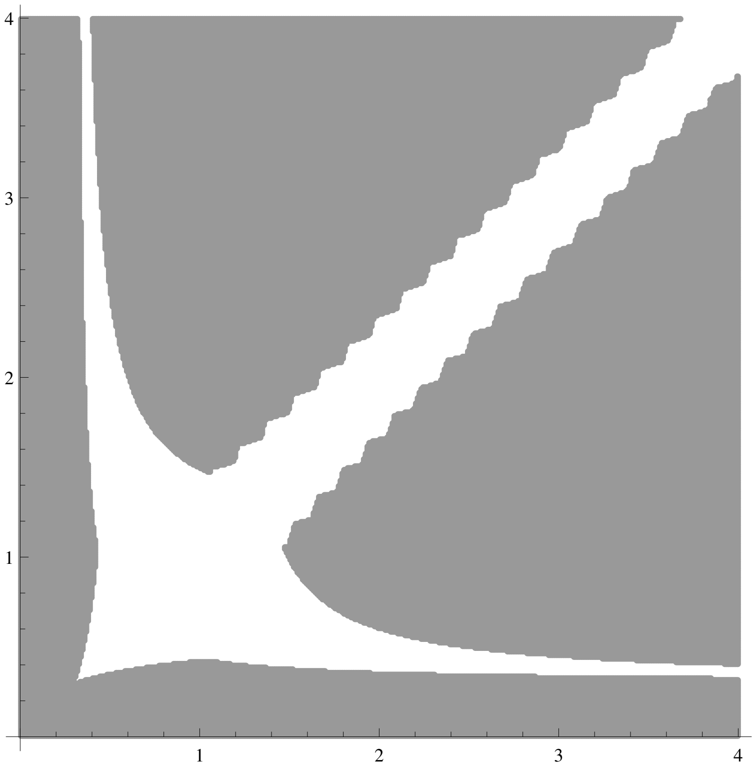

Figure 6.3. Empty histogram bins for the $\mathbb{Z}^2$ lattice, resembling the shape of a swallow.

Remark 6.5
We can see in Fig. 6.2 that the second-order spacings appear to be reflection symmetric with respect to the diagonal. This implies that, for each spacing pair (d_i, d_{i+1}), there exists another pair (d_j, d_{j+1}) with $i \neq j$ such that $d_i = d_{j+1}$ and $d_{i+1} = d_j$. This symmetry property is interesting because the patch used for the computation has no reflection symmetry. Closer inspection reveals that the symmetry property is only approximative, i.e. we have $|d_i - d_{j+1}| \leqslant \epsilon$ and $|d_{i+1} - d_j| \leqslant \epsilon$ for some ϵ depending on the patch size. So, in particular, we do not see the symmetry for small patch sizes.

We pose the question if this is due to the hereditary structure, in the ergodic theoretic sense (see [35, Ch. 3]), of our point set. If we increase the patch size, subpatches with approximate D_4 symmetry appear within the patch, which then contribute to the reflection symmetry we see in the histogram.

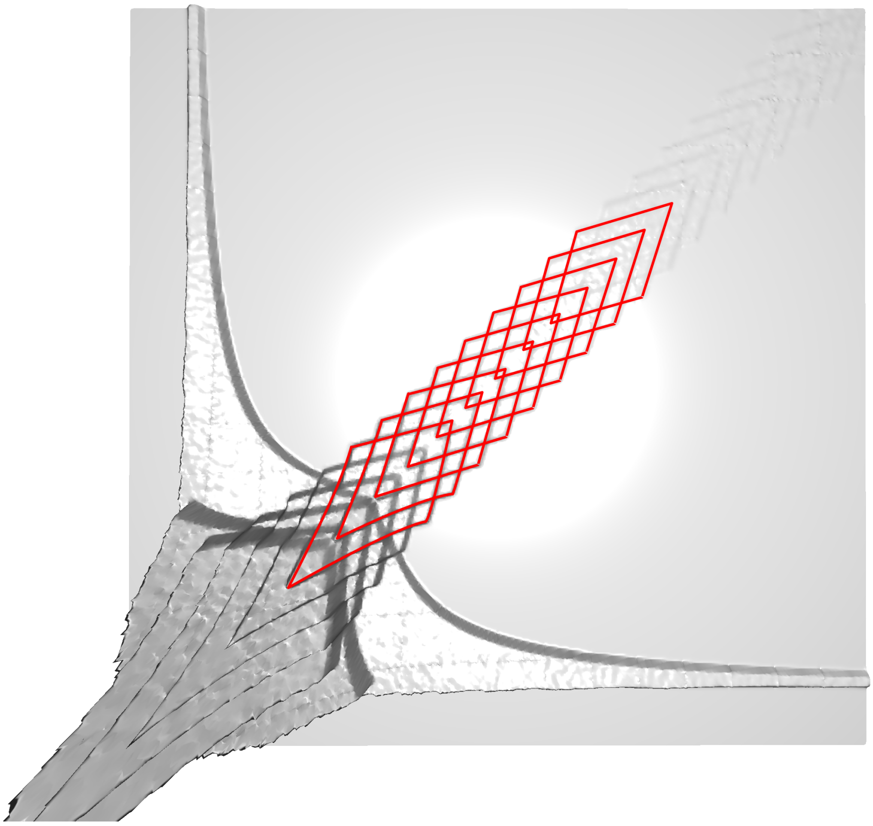

Figure 6.4. Top-down view of the histogram for the $\mathbb{Z}^2$ lattice, with the rhombii structures highlighting in red.

Example 6.6
The second-order spacings of the $\mathbb{Z}^2$ lattice exhibit similar properties as the first-order ones. We again have a pronounced bulk section, see Fig. 6.2, which passes over into a tail section, here forking into three segments. The diagonal segment seems to be constructed from many intersecting rhombii, while the segments in x- and y-direction show no specific structure. See Fig. 6.4 for an illustration from a top-down perspective, where we have highlighted this characterestic structure. The empty bin plot in Fig. 6.3 indicates that the transition between areas with mass and no mass is almost instantaneous, which we attribute to the edge sharpening effect of the arctan, which is applied to compute angles from slopes; compare Remark 1.4.

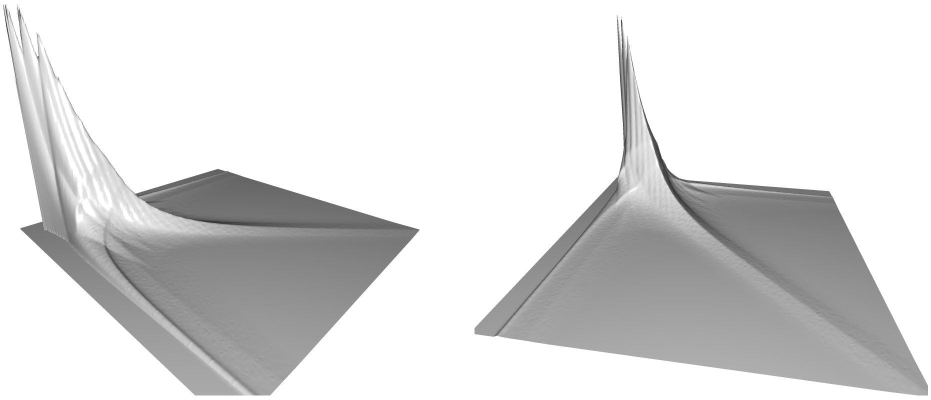

Figure 6.5. Histogram for the slopes of the $\mathbb{Z}^2$ lattice, visualised as a 3-dimensional mesh.

These distinct sharp transitions have only been observed for this case and the related planar chair tiling.

The radius of the patch used to compute the histogram is $R = 20000$, which equals $9.54 \cdot 10^7$ unique vertices after removing redundancy from the D_4 symmetry. Binning was done in the range $[0, 4)^2$ with step sizes $s_x = s_y = 0.01$. We omit s_y in the following examples, since we always used the same step size in each direction.

Remark 6.7

The mesh derived from $\mathbb{Z}^2$ suggests that spacings in the tail follow a dichotomy property. On the one hand, "large" spacings cluster, i.e. it is likely to find another spacing of the same size as neighbour of a large spacing. This is the diagonal tail segment in the mesh, see t_0 in Figure 6.6 below. On the other hand, it is likely to find a small spacing next to a large spacing. These occurences are the tail segments in x and y-direction, denoted as t_1 and t_2.

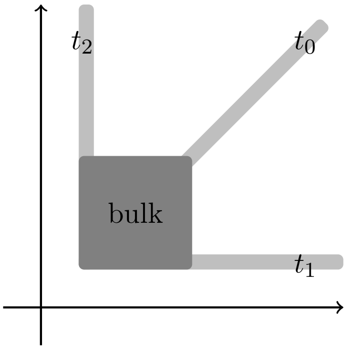

Figure 6.6. Dichotomy of second-order spacings, as observed for the $\mathbb{Z}^2$ lattice. The tail section decomposes into t_0, t_1 and t_2.

So, if we have neighbouring spacings d_i and d_{i+1}, there are only the two configurations $\{d_i \approx d_{i+1}\}$ and $\{d_i \ll d_{i+1}\}$. Any other configuration is suppressed.
What is interesting is that this behaviour not only applies to $\mathbb{Z}^2$, but to other point sets as well. In particular, we see a more complex behaviour there with multiple x, y tail segments, i.e. we have a configuration

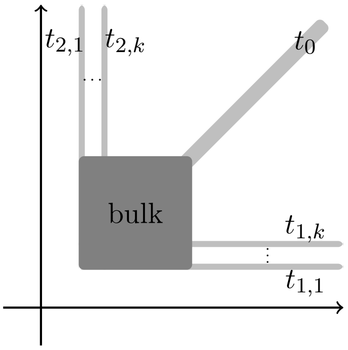

Figure 6.7. Generalised dichotomy pattern of second-order spacings featuring forking tails $t_{i,1}, \ldots, t_{i,k}$ $(i = 1, 2)$.

with $k > 1$ in general. This indicates that the configurations of the type $\{d_i \ll d_{i+1}\}$ are further quantized here in some sense.
We would like to study this in more detail, but the amount of vertices needed to identify segments quickly becomes an issue. See e.g. Fig. 6.13 below for an example where the binning range doesn't allow us to properly count the number of tail segments.

Example 6.8
The planar chair tiling is closely related to the integer lattice in the sense that its vertices are a subset of $\mathbb{Z}^2$. In fact the second-order spacings show a similar behaviour.

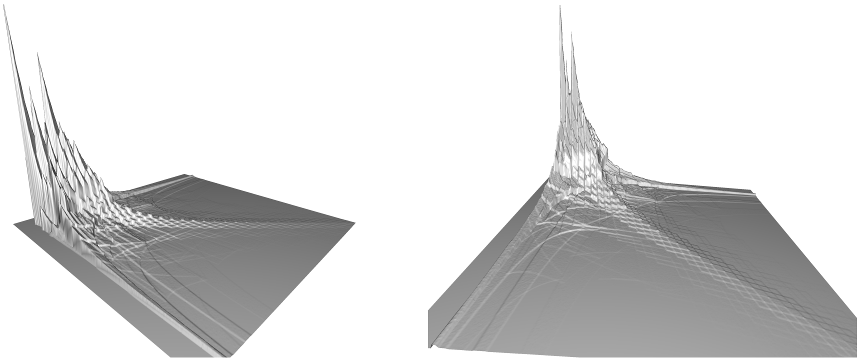

Figure 6.8. Histogram of the second-order spacings for the planar chair tiling.

The meshes in Fig. 6.8 were computed from 15 inflations of the initial seed, see the left side of Fig. 2.20 on page 26. Binning was done with the same parameters as used for the $\mathbb{Z}^2$ lattice.

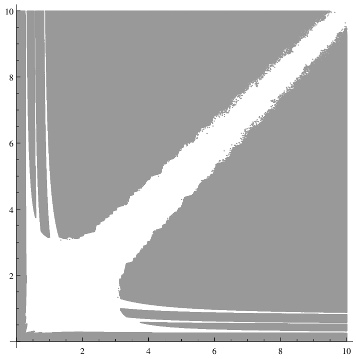

Figure 6.9. Empty histogram bins for the chair tiling.

Even though the plot in Fig. 6.9 is slightly more "noisy" than that of the $\mathbb{Z}^2$ lattice, one can still see that a pronounced inner gap area exists. We have increased the binning range to $[0, 10)^2$ here to show how far the three tail segments extend. In particular, we can see that multiple segments in x/y-direction exist (like we illustrated in Fig. 6.7), three which can be observed at this binning range. It would be interesting to study if one can see another "fork" when further increasing the range.

Also note in Fig. 6.8 that the rhombii shapes in the diagonal tail segment appear again.

Remark 6.9

When we compare the first-order with the second-order spacings, the amount of vertices needed for acceptable histograms is now quadratic. Our analysis shows that, for the bulk section, the vertex count has to at least of the order of 10^7. This still varies with how spread out the mass is. The amount further increases if one is interested in the behaviour of the tail segments.

Table 6.1. Vertex counts (in units of 10^7) for histogram meshes.

tiling	patch	visible	binning
$\mathbb{Z}^2$	–	9.54	9.36
chair	–	85.44	84.03
AB	59.32	34.24	33.66
TT	104.71	55.71	54.74

The *binning* column displays the amount of data inside the binning area. We see that the percentage of data outside the area is usually under 2%.

Example 6.10
We now take a look at the three cyclotomic model sets, AB, TT and GS, from Chapter 2. All are regular model sets with a star-shaped window. We also include the analysis for the RP tiling which can be, as we have seen, described as the union of four disjoint model sets.

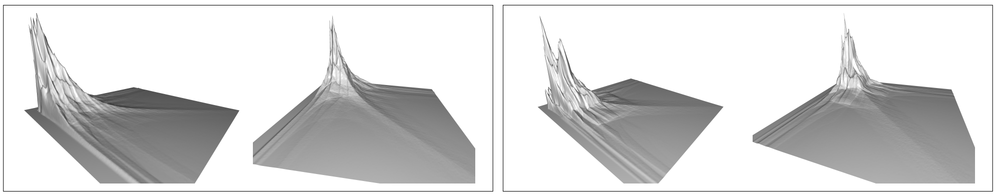

Figure 6.10. Second-order spacings for the AB (left) and the TT (right) tiling.

Similar to the first-order spacings, also here the spacings show a lot of similarity to the $\mathbb{Z}^2$ lattice. A large bulk is present and the tail forks into a diagonal segment and two other ones. Although the histogram resolution is not fine enough to properly tell, Fig. 6.10 suggests that the x/y-segments are composed of two (or more) smaller parallel segments. Compared to $\mathbb{Z}^2$, the sharp contrast between mass and non-mass areas is washed out.

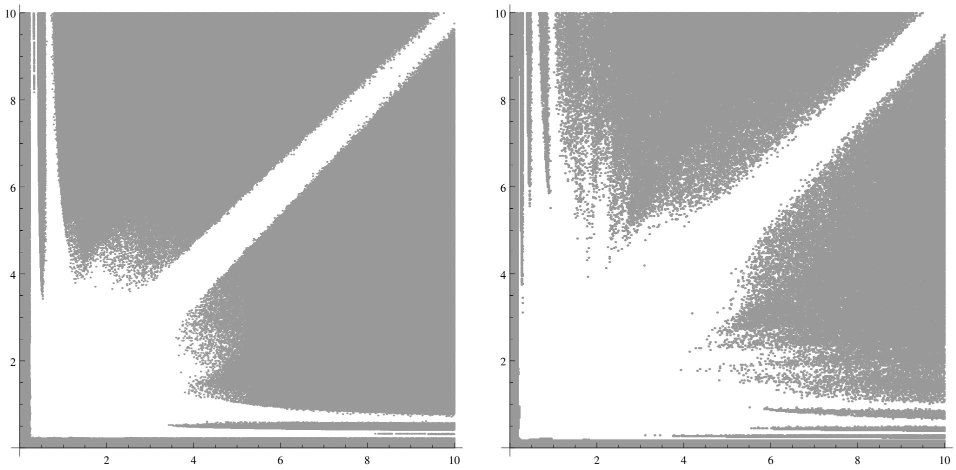

Figure 6.11. Empty histogram bins for the AB (left) and the TT (right) tiling.

The AB patch used for the computation consists of $3.42 \cdot 10^8$ visible vertices, the TT histogram used $5.56 \cdot 10^8$ visible vertices. Due to the larger bulk section, and hence higher patch size requirements, the step size parameter for the meshes was lowered to $s_x = 0.015$ for both tilings. The binning range was kept unchanged.

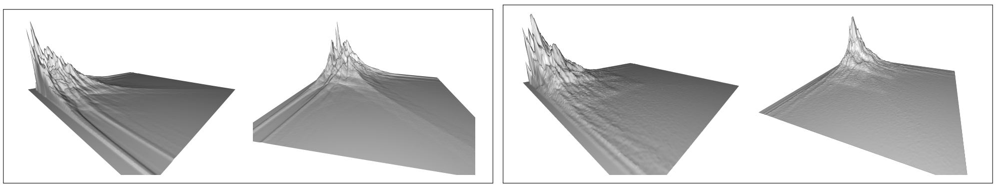

Figure 6.12. Second-order spacings for the GS tiling (left) and the RP tiling (right).

The RP histogram is the only case so far where the diagonal tail segment is absent or very poorly developed. Also Fig. 6.13 poses the question whether an inner gap area exists here, or if going to the limit, i.e. patch size $\to \infty$, also further spreads out the histogram mass. The numerics suggest that the latter is actually the case.
Since the missing tail feature is unique to this case, we also ask whether this is an effect of the more sophisticated window setup that is used to describe the tiling with a CPS.

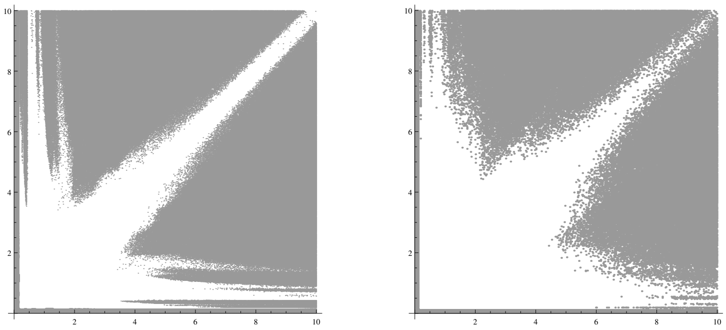

Figure 6.13. Empty histogram bins for the GS (left) and the RP (right) tiling.

At the end of Chapter 4 we already conjectured that the similarity between the $\mathbb{Z}^2$ case and the cyclotomic model set cases is due to the projection of a higher-dimensional lattice, whose order properties survive to some extend in the radial projection. It would be interesting to evaluate how the complexity of the window in internal space factors into this equation. The current results suggest that the second-order spacings are slightly more sensitive to the complexity of the window than the first-order ones.

Table 6.2. Vertex counts (in units of 10^7) for remaining meshes.

tiling	patch	visible	binning
GS	100.73	63.32	62.13
RP	21.05	12.01	11.79

Note that the excess data outside the binning area is again under 2%. In particular, this shows how few data are available when extending the range from 4 to 10 for the empty bin plots.

Example 6.11
The LB tiling has shown strong similarity with Poisson distributed points on the level of the first-order spacings, see Section 2.6, although the corresponding inflation rule impose some order on the vertices. Our initial hope was to more clearly differentiate between the two point sets by moving to the second-order spacings.

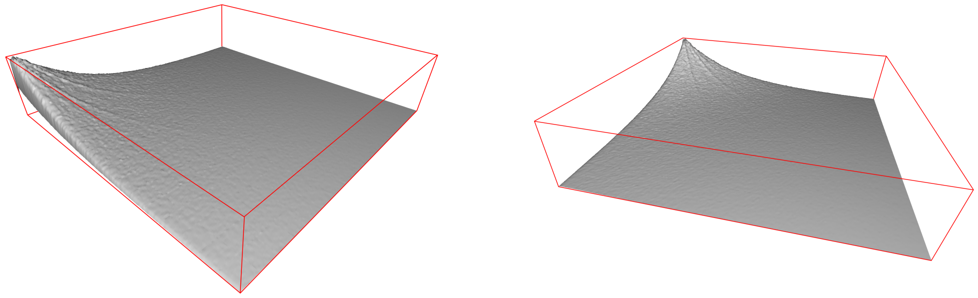

Figure 6.14. Second-order spacings for the LB tiling (bounding box in red).

We see that the histogram approximates the product measure of the exponential distribution, hence neighbouring d_i seem to be uncorrelated. In this respect, we end up with the same picture as in the Poisson case.
Since the histogram in Fig. 6.14 inherits the outer gap area from the first-order spacings, there still is some noticeable discrepancy to the “raw” product measure. A slightly better reference is given by the modified exponential density function

$$f(s,t) = \exp(-|s-\epsilon|) \cdot \exp(-|t-\epsilon|)$$

with $\epsilon \approx 0.2$. This constant obviously depends on the patch size, and was here chosen to minimise error when fitting the data in Fig. 6.14. The same question as for the first-order spacings can be asked here, namely if $\epsilon \to 0$ as the patch size increases.

Remark 6.12
We have seen that both strongly correlated ($\mathbb{Z}^2$, chair, cyclotomic model sets and RP) and essentially uncorrelated (LB) cases occur. One might now ask the question how “far” these correlations in the former cases range. Hence, we consider $\sigma_{R,k}$ from Procedure 6.1 with increasing step size k.

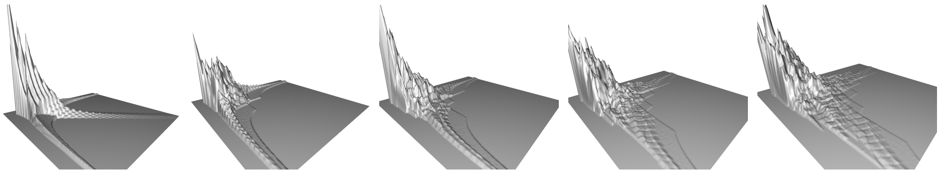

Figure 6.15. Second-order spacings for $\mathbb{Z}^2$ with $1 \leqslant k \leqslant 5$.

The first observation in Fig. 6.15 is that the diagonal tail segment disappears immediately when moving from $k = 1$ to $k \geqslant 2$. The other tail segment breaks down into a low and high part and the bulk section loses the "chiseled" structure. Also note, that while the bulk gives away mass for the step $k = 1 \to 2$, it reclaims it again in the step $k = 2 \to 3$.

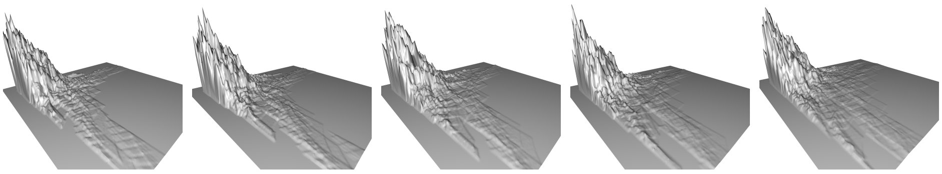

Figure 6.16. Second-order spacings for $\mathbb{Z}^2$ with $6 \leqslant k \leqslant 10$.

The overall structure further collapses when moving to $k = 10$. It appears that the correlations are only short ranged for this examples, and that characteristic features are already absent when moving away from the next-neighbourhood configuration. All ten meshes were computed from the same patch with $5.37 \cdot 10^7$ vertices.

Due to time constraints, we only considered the simplest case here. We therefore pose the question whether there are any long range correlations for the tilings of cyclotomic type.

Remark 6.13

Last, we briefly study how the mass is distributed in the binning area. In all cases, we have chosen a square binning area of the type $[0, a)^2$. Let $k \in \mathbb{N}$, define $s := \frac{a}{k}$, and consider the subsets

$$[0, i \cdot s) \quad \text{for} \quad 1 \leqslant i \leqslant k \; .$$

For each i, we ask how many data points are located in the respective subset. We then rescale this value with the total amount of points available, which yields a value $m_i \in [0, 1]$. By applying interpolation to the m_i, we recover a map $\mathrm{m} : [0, a] \to [0, 1]$ which is similar to the cumulative distribution function of a random variable. For lack of a better term, we just call m the CDF of the second-order spacings.

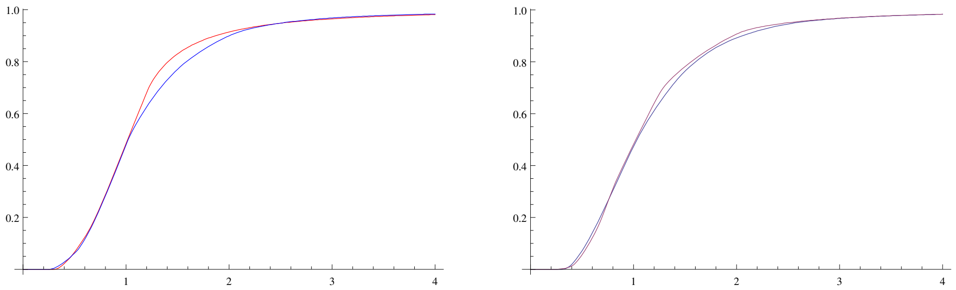

Figure 6.17. CDFs for the $\mathbb{Z}^2$ lattice (red), chair (blue), AB (red) and TT (blue) tiling (from left to right).

The maximum value m(4) is 0.981, 0.983, 0.983 and 0.984 for $\mathbb{Z}^2$, chair, AB and TT, respectively.

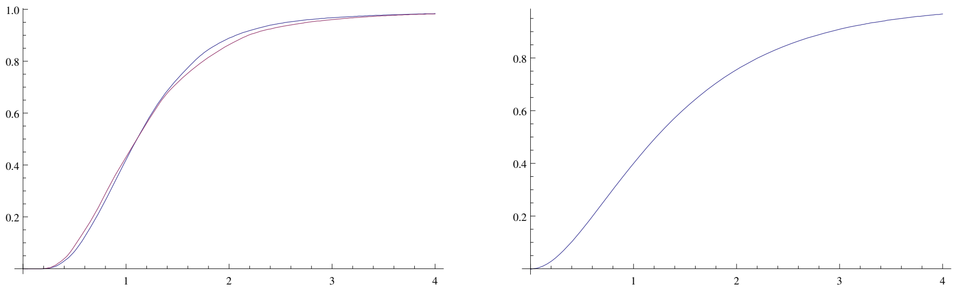

Figure 6.18. CDFs for the GS (red), RP (blue) and LB tiling.

Here, we have $\mathrm{m}(4) = 0.984$, 0.982 and 0.967 for GS, RP and LB respectively. Apart from the LB tiling, there is not much difference between the graphs.

Remark 6.14

A possible generalisation of the second-order spacings is given by the following object. Let $N \in \mathbb{Z}$ and define the discrete probability measure in $\mathbb{R}^N$ by

$$\sigma_{R,N} \ := \ \frac{1}{m} \sum_{i=1}^{m} \delta_{i,N} \ ,$$

where we again work with the setup from Procedure 1.1. The entry $\delta_{i,N}$ is the Dirac measure at the position $(d_{i+N}, d_{i+N-1}, \ldots, d_i)$. Denote the limit $R \to \infty$ of $\sigma_{R,N}$, in the weak sense, as the Nth-order spacings.

While the computation of our histograms does not change significantly, already for $N = 3$ the problem of data visualisation arises. One approach would be to extract “slices” of the histogram, another to apply a suitable projection down to $\mathbb{R}^3$.

Conclusion 6.15

The calculation of the this section are largely experimental, and there are some heuristic explanations at best – even for the case of the square lattice. Hence, while the first-order spacings are well understood for $\mathbb{Z}^2$, the strange features of the spacings of higher order reveal that our understanding of the radial structure of $\mathbb{Z}^2$ is still very limited.

In fact, the analysis of second-order spacings was initially motivated by the linearity properties showing up during the randomisation of the tiling vertices. So, a better understand of the behaviour of the spacings might also give us more insight into the non-linear behaviour observed for the ω-thinning.

CHAPTER 7

Arithmetic visibility in number fields

In Chapter 4, we have explored the geometric visibility in specific point sets. Here, we discuss a different version of visibility in an algebraic sense. A nice property of the examples we consider is that they allow for an elegant computation of the diffraction pattern. The algorithms presented here are based on [6, Ch. 5] and references therein.

Our starting point is an algebraic number field $\Bbbk$, where we denote the corresponding integers as $\mathfrak{o}$; compare Definition 4.2. The geometric visibility is now replaced by the property that an integer x should be square-free, i.e. the factorisation of x contains no square of a prime. In general, one can consider k-free integers, but we restrict our attention to the case $k = 2$. An adaptation of the algorithms to arbitrary k is straightforward.

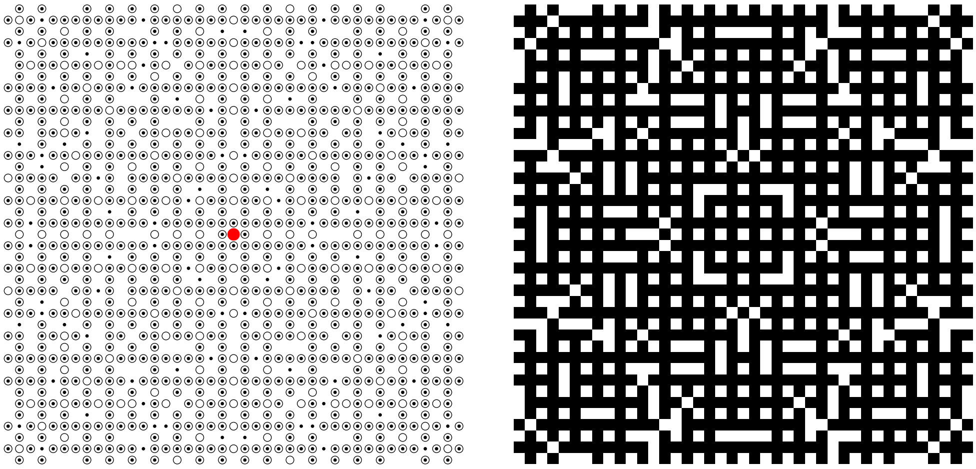

Figure 7.1. Square-free Gaussian integers. Dot with overlay (left) and grid (right) plot of the region $[-20, 20]^2$. The origin is indicated in red.

The left side of Fig. 7.1 shows the difference between the arithmetic and geometric visibility. The geometrically visible vertices are indicated as filled dots, whereas the arithmetically visible ones are drawn as (unfilled) circles. While there certainly is a high overlap here, we are still dealing with different point sets.

We also point out, that despite our claim in the introduction, we are going to explore some examples of "order by diffraction" (pure point diffraction) in this chapter.

7.1. Prime factorisation

Remark 7.1
We only want to consider quadratic number fields as underlying set, i.e. $\mathbb{k}$ has degree 2 over $\mathbb{Q}$. We denote the corresponding ring of integers in $\mathbb{k}$ as $\mathfrak{o}$, and just call elements therein integers. If necessary, we use the term $\mathbb{Z}$-integer for elements from $\mathbb{Z}$.
For our approach, we need to compute the prime factorisation in $\mathfrak{o}$. From Definition 4.3, we know how to coordinatise $\mathfrak{o}$ in terms for $\mathbb{Z}$-integers.

Let $x \in \mathfrak{o}$ be an integer that we want to factorise and denote by $\mathrm{N}(\cdot)$ the algebraic norm in $\mathfrak{o}$.
If $|\mathrm{N}(x)| = 1$, x is a unit and we are done. If x is not a unit, let $\mathfrak{P} := (p_i)_i$ be the prime factorisation of $\mathrm{N}(x)$ in $\mathbb{Z}$ without multiplicities. At this point, we need to know which primes have which type (ramified, splitting and inert). Only finitely many primes $p \in \mathbb{Z}$ can ramify in $\mathfrak{o}$, so we can keep a set of corresponding prime elements $r_p \in \mathfrak{o}$. For our examples, this is especially easy, since the ramified prime is always unique. If a prime $p \in \mathbb{Z}$ is splitting, we can find a $y \in \mathfrak{o}$ such that $\mathrm{N}(y) = yy' = p$, a property which we use in the algorithm below. This operation is essentially well-defined, since the algebraic conjugate y' is the only other element that satisifies the property. We therefore simply write $y = \mathrm{split}(p)$ and consider this as a map.

```
input  : integer $x$ in $\mathfrak{o}$
output : array factorisation of primes in $\mathfrak{o}$
initialize factorisation to $\varnothing$;
$\mathfrak{P} \leftarrow$ factorise $\mathrm{N}(x)$ in $\mathbb{Z}$;
foreach $p \in \mathfrak{P}$ do
    if $p$ ramifies then
        add $r_p$ to factorisation;
    if $p$ is inert then
        add $p$ to factorisation;
    if $p$ is splitting then
        $y \leftarrow \mathrm{split}(p)$;
        if $y$ divides $x$ then
            add $y$ to factorisation;
        if $y'$ divides $x$ then
            add $y'$ to factorisation;
end
```

Algorithm 4: Generic prime factorisation for integers in a quadratic field.

The output of Algorithm 4 is the list of primes in $\mathfrak{o}$ that divide x. To extract also the multiplicities, we have to work a bit harder, but we omit this step since multiplicities are not needed for our purpose.

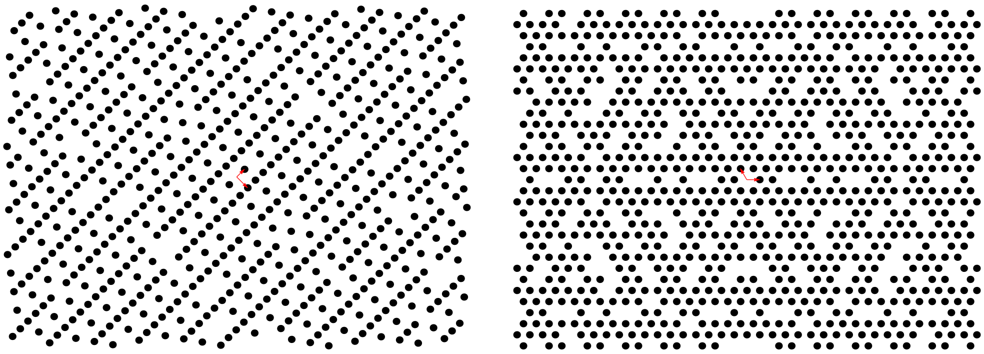

Figure 7.2. Patch of square-free integers in $\mathbb{Z}[\sqrt{2}]$ (left) and $\mathbb{Z}[\omega]$ (right), with $\omega = \exp(\frac{2\pi i}{3})$. Lattice basis displayed in red.

The patches in Fig. 7.2 we created by cropping the vertices with the rectangle $[-31, 31] \times [-22, 22]$ and $[-18, 18] \times [-13, 13]$ respectively.

7.1.1. The integers $\mathbb{Z}[\sqrt{2}]$.

We have already studied $\mathbb{Z}[\sqrt{2}]$ in Chapter 4. Let us restate some properties. Define $\epsilon := 1 + \sqrt{2}$. Then, the units in $\mathbb{Z}[\sqrt{2}]$ are all $\pm\epsilon^k$ with $k \in \mathbb{Z}$. The algebraic norm is given by

$$a + b \cdot \sqrt{2} \;\mapsto\; a^2 - 2b^2 \; .$$

The unique *ramified* prime is $2 = \sqrt{2}^2$. A prime p is *inert* if $p \equiv \pm 3 \bmod 8$, and *splitting* if $p \equiv \pm 1 \bmod 8$.

```
input  : splitting prime $p$ in $\mathbb{Z}$
output : integer out in $\mathfrak{o}$
initialize $x$ to $\lceil \sqrt{p} \rceil$;
while true do
    $y \leftarrow [\sqrt{(x^2 - p)/2}]$;
    if $2y^2 - x^2 + p = 0$ then
        break;
    $x \leftarrow x + 1$;
end
out $\leftarrow x + y \cdot \sqrt{2}$;
```

Algorithm 5: Computation of out = split(p) for $\mathbb{Z}[\sqrt{2}]$.

The temporary variables x, y in Algorithm 5 are $\mathbb{Z}$-integers. The map $\lceil \cdot \rceil$ is the ceiling function, $[\, \cdot \,]$ rounds to the nearest $\mathbb{Z}$-integer. Since we know that, for any splitting prime p, there always exists some out $\in \mathfrak{o}$ with $\mathrm{N}(\mathsf{out}) = p$, the while loop terminates, usually after a few cycles. This is a brute force approach, but it suffices in this context, since the input values are small. By examining the corresponding algebraic norm, one can derive similar algorithms for the other cases.

7.1.2. Gaussian integers.

The Gaussian integers are $\mathbb{Z}[\mathrm{i}]$, with i the imaginary unit. The units in $\mathbb{Z}[\mathrm{i}]$ are just the four elements $\{\pm 1, \pm\mathrm{i}\}$, and the algebraic norm is given by

$$a + b \cdot \mathrm{i} \;\mapsto\; a^2 + b^2 \; .$$

The unique ramified prime is $2 = \mathrm{i}(1-\mathrm{i})^2$. A prime p is inert if $p \equiv 3 \bmod 4$, and splitting if $p \equiv 1 \bmod 4$. We have already encountered the Gaussian integers in Section 1.2, there “disguised” as the square lattice $\mathbb{Z}^2$.

7.1.3. Eisenstein integers.

The Eisenstein integers are the set $\mathbb{Z}[\omega]$ with

$$\omega \;:=\; \exp(2\pi\mathrm{i}/3) \; ,$$

a primitive root of unity which satisfies $\omega^2 + \omega + 1 = 0$. The units in $\mathbb{Z}[\omega]$ are the six elements

$$\{\pm 1, \pm\omega, \pm\omega^2\} \; .$$

If we let $x := a + b \cdot \omega$, then the norm maps x to $a^2 - ab + b^2$. The unique ramified prime is $3 = (-\omega^2)(1-\omega)^2$. A prime p is inert if $p \equiv 2 \bmod 3$, and splitting if $p \equiv 1 \bmod 3$. In Section 2.8, we have seen $\mathbb{Z}[\omega]$ as the triangular tiling and applied RPM to it. The corresponding vertex set is known as the hexagonal lattice.

7.1.4. The integers $\mathbb{Z}[\tau]$.

This is another set which we have already seen in Chapter 4, in conjunction with the TT tiling. We have

$$\tau \;=\; \frac{1+\sqrt{5}}{2} \; , \quad \text{with} \quad \tau^2 - \tau - 1 = 0 \; ,$$

the golden mean, which also generates the units of $\mathbb{Z}[\tau]$, i.e.

$$\mathbb{Z}[\tau]^{\times} \;=\; \{\pm\tau^k \;:\; k \in \mathbb{Z}\} \; .$$

The algebraic norm in $\mathbb{Z}[\tau]$ is given by $a + b \cdot \tau \mapsto a^2 + ab - b^2$. The unique ramified prime is $5 = (-1 + 2\tau)^2$. A prime p is inert if $p \equiv \pm 2 \bmod 5$, and splitting if $p \equiv \pm 1 \bmod 5$.

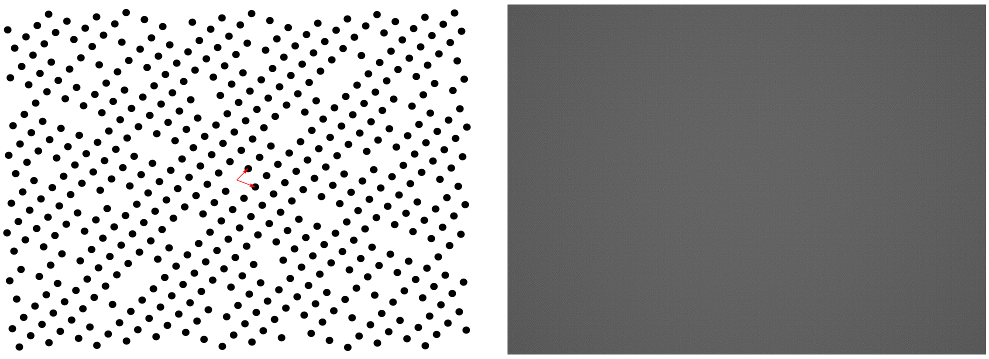

Figure 7.3. Patch of square-free integers in $\mathbb{Z}[\tau]$ (left) and $\mathbb{Z}[\mathrm{i}]$ (large downsampled patch) (right). The uniform pattern on the right is not an artifact, see the text below.

The $\mathbb{Z}[\mathrm{i}]$ plot in Fig. 7.3 was produced from an initial grid with size 8000^2, and then downsampled with a factor 4 using a Lanczos-based [13, Ch. 10.3] resampling filter. While it is known that the square-free Gaussian integers have the same property as the visible lattice points, namely the existence of arbitrary large holes, the plot clearly shows that these holes are very rare. The apparantly uniform grey distribution corresponds to the existence of the density of this set, with respect to centred discs of growing radius. Big holes occur, but are exponentially rare.

Note that simpler downsampling filters, like e.g. a bilinear filter, are not suitable here, since they produce undesirable artifacts in the form of centred halos.

7.2. Square- and cube-free integers

In addition to the prime factorisation, we also need to determine if an integer is square-free, so that we can construct the point set which serves as the input of either diffraction, see the next section, or radial projection, see Section 7.4.

If the set of integers $\mathfrak{o}$ is contained in $\mathbb{R}$, which applies to $\mathbb{Z}[\sqrt{2}]$ and $\mathbb{Z}[\tau]$ here, we consider the *Minkowski embedding* [5, Ch. 3.4] of $\mathfrak{o}$ as input set, see Eq. (7.1) and (7.1). For our cases, this gives a lattice in $\mathbb{R}^2$, and the corresponding square-free integers are then a subset. The two remaining cases are already lattices to begin with. In particular, RPM works as usual here, but depending on the "size" of the Minkowski embedding, we have to deal with the issues explained in Section 1.4. Explicitly, we use

$$\mathfrak{me} : \mathbb{Z}[\sqrt{2}] \ni a + b \cdot \sqrt{2} \mapsto (a + b \cdot \sqrt{2}, a - b \cdot \sqrt{2}) \; , \tag{7.1}$$

$$\mathfrak{me} : \mathbb{Z}[\tau] \ni a + b \cdot \tau \mapsto (a + b \cdot \tau, a + b \cdot \tau') \; . \tag{7.2}$$

For $\mathbb{Z}[\mathrm{i}]$ and $\mathbb{Z}[\omega]$, we define the embedding through $\mathfrak{me}(a + b \cdot \mathrm{i}) = (a, b)$.

The computation of the diffraction also requires to determine whether a given integer is cube-free, or $(k+1)$-free if we consider the general case. Since this amount to just changing some of the exponents in the algorithms, we omit the details here and focus just on square-freeness.

```
input  : integer $x$ in $\mathfrak{o}$
output : boolean
// use coordinatisation property of o
$(a, b) \leftarrow x$;
foreach ramified $p$ in $\mathfrak{o}$ do
    if $p \mid a \;\wedge\; p \mid b$ then
        return false;
end
$\mathfrak{P} \leftarrow$ factorise $\mathrm{N}(x)$ in $\mathbb{Z}$;
foreach $p \in \mathfrak{P}$ do
    if $p$ is inert then
        if $p^2 \mid_c x$ then
            return false;
    if $p$ is splitting then
        $y \leftarrow \mathrm{split}(p)$;
        if $p^2 \mid_c y^2$ or $p^2 \mid_c (y')^2$ then
            return false;
end
return true;
```

Algorithm 6: Generic square-free check for integers in a quadratic field.

In Algorithm 6, we first check for squared factors coming from the ramified primes, which is unique in our cases. We then proceed analogous to Algorithm 4 and gather potential candidates for other square factors by looking at the factorisation of $\mathrm{N}(x)$. Let us explain the details for $\mathbb{Z}[\sqrt{2}]$.

For $a \in \mathbb{Z}$ and $x \in \mathfrak{o}$, we understand $a \mid_c x$ as divisibility in both component, i.e. if $x = x_1 + x_2 \cdot \sqrt{2}$ then we require both $a \mid x_1$ and $a \mid x_2$. In general, if we want to check for k-freeness, we also need a generic division test for the ramified primes, e.g. we need to compute if $\sqrt{2}^k$ divides x in $\mathfrak{o} = \mathbb{Z}[\sqrt{2}]$. We just refer to the procedure described in Remark 4.38 here, since the required test is implemented analogously.

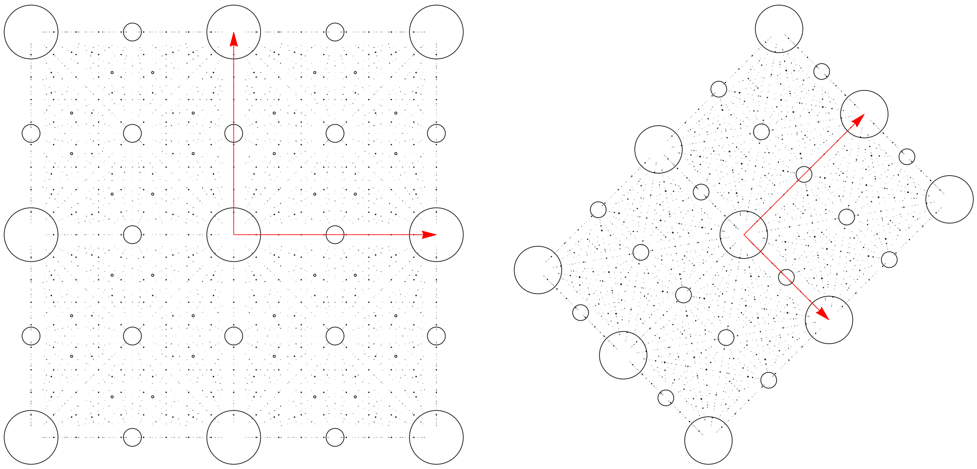

Figure 7.4. Diffraction of square-free integers in $\mathbb{Z}[\mathrm{i}]$ (left) and $\mathbb{Z}[\sqrt{2}]$ (right). Basis of dual lattice indicated in red.

Note that we have applied a non-linear rescaling of the intensities in Fig. 7.4 to improve the image contrast, i.e. to better differentiate between small intensities of different size.

Table 7.1. Sampling parameters for diffraction plots.

ring	rescaling	N	D
$\mathbb{Z}[\mathrm{i}]$	$x \mapsto 0.2 \cdot \sqrt{x}$	30	17
$\mathbb{Z}[\sqrt{2}]$	$x \mapsto 0.4 \cdot \sqrt{x}$	20	16

For the sampling ranges N, D see Eq. (7.3) below. We always crop the diffraction plots to the four fundamental domains around the origin.

7.3. Diffraction pattern

We employ the standard notation $\widehat{\gamma}$ for the diffraction measure. To produce a good approximation of $\widehat{\gamma}$, we first need to consider the set on which the measure is supported. Let $y \in \Bbbk$. Then, we can write

$$y = \frac{y_0}{d}, \quad \text{where} \quad y_0 \in \mathfrak{o},\ d \in \mathbb{Z}\,.$$

The *denominator* of y is now computed as

$$\operatorname{den}(y) := \frac{d}{\gcd_{\mathfrak{o}}(y_0, d)}\,,$$

see [6] for a more general definition. The choice of GCD above does not matter, as we are going to see shortly. We take the dual module [14, Sec. 2] $\mathfrak{o}^*$ of $\mathfrak{o}$ and consider the $\mathbb{Q}$-span of $\mathfrak{o}^*$, which is a subset of $\Bbbk$. The support is then given by the set

$$\Lambda^* \; := \; \operatorname{supp}(\widehat{\gamma}) \; = \; \{\mathfrak{me}(y) \; : \; y \in \mathbb{Q}\mathfrak{o}^*, \; \operatorname{den}(y) \text{ is cube-free}\} \; ,$$

or using the condition den(y) (k+1)-free in the general case. With this, the diffraction can be written as

$$\widehat{\gamma} \; = \; \sum_{y \in \Lambda^*} I(y) \delta_y \; ,$$

where $I(y)$ is the intensity at the position y. We focus on Λ^* first, before computing the intensities.

For our purpose, we chose to work directly on the level of lattices. We start by creating a region in $\Bbbk$ and then apply a transformation to sample $\mathbb{Q}\mathfrak{o}^*$. First, we need to understand what dualisation does on the lattice level. Consider the Eisenstein integers $\mathfrak{o} = \mathbb{Z}[\omega]$ for now.

Let $a + b \cdot \omega \in \mathfrak{o}$ and identify this element via $\mathfrak{me}$ with

$$a \cdot \mathfrak{b}_1 + b \cdot \mathfrak{b}_2, \quad \mathfrak{b}_1 := \begin{pmatrix} 1 \\ 0 \end{pmatrix}, \; \mathfrak{b}_2 := \begin{pmatrix} -1/2 \\ \sqrt{3}/2 \end{pmatrix} \; ,$$

which is a point in the complex plane. The corresponding lattice basis vectors are $\mathfrak{b}_1, \mathfrak{b}_2$, so we compute the basis for the dual lattice via

$$\mathfrak{B} := \begin{pmatrix} 1 & -1/2 \\ 0 & \sqrt{3}/2 \end{pmatrix}, \quad \mathfrak{B}^* := (\mathfrak{B}^{-1})^T = \begin{pmatrix} 1 & 0 \\ 1/\sqrt{3} & 2/\sqrt{3} \end{pmatrix} \; ,$$

hence we have $\mathfrak{b}_1^* = (1, 1/\sqrt{3})^T$ and $\mathfrak{b}_2^* = (0, 2/\sqrt{3})^T$. Now, construct λ_i, μ_i such that

$$\lambda_i \cdot \mathfrak{b}_1 + \mu_i \cdot \mathfrak{b}_2 = \mathfrak{b}_i^* \; ,$$

i.e. we write our dual basis in terms of the original one. If we let

$$A \; := \; \begin{pmatrix} \lambda_1 & \lambda_2 \\ \mu_1 & \mu_2 \end{pmatrix} \; ,$$

then $A = \mathfrak{B}^{-1} \cdot (\mathfrak{B}^{-1})^T$ which then corresponds to the following map for our original element,

$$a + b \cdot \omega \; \longmapsto \; \frac{2}{3} \left[(2a + b) + (a + 2b) \cdot \omega \right] \; .$$

In fact, we need the inverse of this map extended from $\mathfrak{o}$ to $\Bbbk$, which is then given by

$$\mathfrak{s}_{\mathbb{Z}[\omega]} : \frac{a + b \cdot \omega}{c} \; \longmapsto \; \frac{(2a - b) + (-a + 2b) \cdot \omega}{2c} \; .$$

This approach works the same way for the other cases. In particular, for the Gaussian integers, the map is the identity because $\mathbb{Z}[\mathrm{i}] \simeq \mathbb{Z}^2$ is self-dual. The map for $\mathbb{Z}[\sqrt{2}]$ reads

$$\mathfrak{s}_{\mathbb{Z}[\sqrt{2}]} : \frac{a + b \cdot \sqrt{2}}{c} \; \longmapsto \; \frac{2a + 4b \cdot \sqrt{2}}{c}$$

and the one for $\mathbb{Z}[\tau]$ is

$$\mathfrak{s}_{\mathbb{Z}[\tau]} : \frac{a+b\cdot\tau}{c} \longmapsto \frac{(2a+b)+(a+3b)\cdot\tau}{c} .$$

Let $N, D \in \mathbb{N}_1$ and define the untransformed sampling region

$$\mathfrak{S} := \{\frac{a+b\cdot\varphi}{c} : |a|, |b| \leqslant N,\ 1 \leqslant c \leqslant D\} , \tag{7.3}$$

where $\varphi \in \{\sqrt{2}, \mathrm{i}, \omega, \tau\}$ depending on which case we consider. We then use

$$\mathfrak{S}^* := \{y \in \mathfrak{S} : \operatorname{den}(\mathfrak{s}(y)) \text{ cube-free}\}$$

as the our sampling region, $\mathfrak{s}$ being the corresponding map.
We are now well prepared for the final step, which consists in computing the intensities,

$$I(y) = \left(\frac{1}{c_0}\frac{1}{\zeta_{\Bbbk}(k)}\prod_{p\in\mathfrak{P}}\frac{1}{\mathrm{N}(p)^k-1}\right)^2 . \tag{7.4}$$

The constant c_0 is the volume of the fundamental domain of our lattice $\mathfrak{me}(\mathfrak{o})$, $\zeta_{\Bbbk}$ the Dedekind zeta function of the corresponding algebraic number field $\Bbbk$ and $\mathfrak{P}$ the prime factorisation of $\operatorname{den}(y)$ in $\mathfrak{o}$ as explained in Section 7.1. For the square-free case, we let $k = 2$. Note that Eq. 7.4 only holds for y with $\operatorname{den}(y)$ cube-free, otherwise the intensity vanishes.

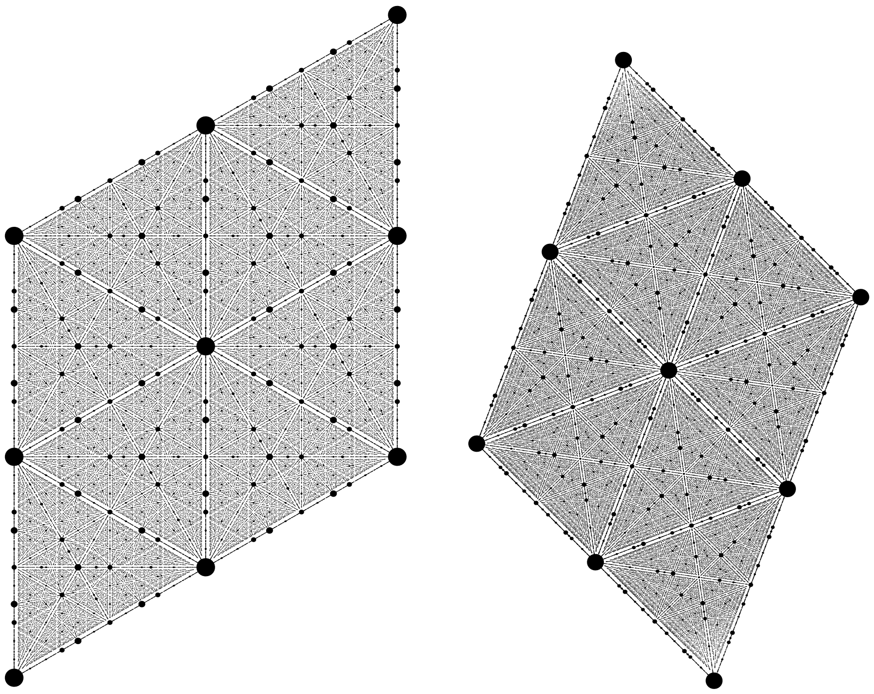

Figure 7.5. High-resolution diffraction of $\mathbb{Z}[\omega]$ (left) and $\mathbb{Z}[\tau]$ (right).

As explained previously, the diffraction computed in Fig. 7.5 is in terms of the corresponding Minkowski embedding. Also note, that the intensities in are once again rescaled, here with the functions from Table 7.2. Even without highlighting the basis of the dual lattice, a fundamental domain is clearly visible. This is not surprising, since the diffraction is known to be periodic with respect to the dual lattice; see [5, Ch. 10.3] for details.

Table 7.2. Sampling parameters for high-resolution diffraction plots.

ring	rescaling	N	D
$\mathbb{Z}[\omega]$	$x \mapsto 0.05 \cdot \sqrt[4]{x}$	51	47
$\mathbb{Z}[\tau]$	$x \mapsto 0.05 \cdot \sqrt[4]{x}$	75	47

The zeta function and the volume c_0 can be computed as follows. The volume is just $|\det A|$, where the matrix A contains our lattice basis. For the evaluation of $\zeta_{\mathbb{k}}(2)$, we use the fact that we can factorise a Dedekind zeta function into a Dirichlet L-series and the common zeta function over $\mathbb{Q}$ (see Theorem 1 and the corresponding Corollary in [50, Ch. 11]),

$$\zeta_{\mathbb{k}}(s) \;=\; \zeta_{\mathbb{Q}}(s) \cdot \mathrm{L}(s, \chi) \; .$$

Here, χ is the fundamental Dirichlet character for $\mathbb{k}$. This works for all quadratic extensions of $\mathbb{Q}$. Once we know χ, we can approximate $\mathrm{L}(2, \chi)$ with arbitrary precision. In fact, we do know χ already, since we have described how to identify the different prime types in Section 7.1.1 to 7.1.4. The special value of the common zeta function is $\zeta(2) = \frac{\pi^2}{6}$.

Table 7.3. Parameters and values of the Dirichlet character.

ring	modulus	index	$\mathrm{L}(2, \chi)$	volume c_0
$\mathbb{Z}[\sqrt{2}]$	8	2	$\frac{\pi^2}{8\sqrt{2}} \approx 0.872358$	$2\sqrt{2}$
$\mathbb{Z}[\mathrm{i}]$	4	2	$\beta(2) = C \approx 0.915966$	1
$\mathbb{Z}[\omega]$	3	2	$l_\omega \approx 0.781302$	$\frac{\sqrt{3}}{2}$
$\mathbb{Z}[\tau]$	5	3	$\frac{4\pi^2}{25\sqrt{5}} \approx 0.706211$	$1 - 2\tau$

Since the index parameter is not used consistently in the literature, we provide the values $\chi(k)$ (for one period) of the characters from Table 7.3. We used the indexing convention from the `Mathematica` computer algebra system here.

Table 7.4. Values $\chi(k)$ of the Dirichlet characters from Table 7.3 for $1 \leqslant k < m$ (m the modulus). We always have $\chi(0) = 0$.

ring	$\chi(1)$	$\chi(2)$	$\chi(3)$	$\chi(4)$	$\chi(5)$	$\chi(6)$	$\chi(7)$
$\mathbb{Z}[\sqrt{2}]$	1	0	-1	0	-1	0	1
$\mathbb{Z}[\mathrm{i}]$	1	0	-1				
$\mathbb{Z}[\omega]$	1	-1					
$\mathbb{Z}[\tau]$	1	-1	-1	1			

The value C in Table 7.3 is also known as the *Catalan* constant [21], and is just the special value at 2 of the Dirichlet beta-function [42]. Whenever possible we have also included the exact value of $\mathrm{L}(2,\chi)$ by means of the well-known functional equation [32, 50]

$$\Gamma(s) \cos\left(\frac{\pi(s-\delta)}{2}\right) \mathrm{L}(s,\chi) \;=\; \frac{\tau(\chi)}{2i^{\delta}} \left(\frac{2\pi}{f}\right)^{s} \mathrm{L}(1-s,\overline{\chi})\ . \tag{7.5}$$

Here, f is the conductor of χ and $\delta = 0$ if $\chi(-1) = 1$, and $\delta = 1$ else. $\tau(\chi)$ is the Gaussian sum

$$\tau(\chi) \;=\; \sum_{k=1}^{f} \chi(k) \exp(2\pi \mathrm{i} k/f)\ .$$

We can see that, in case $\delta = 1$ holds, we have $\cos(\pi(s-\delta)/2) = 0$ and hence both sides of Eq. 7.5 vanish. In this situation, $\mathbb{Z}[\mathrm{i}]$ and $\mathbb{Z}[\tau]$ here, we cannot establish a connection to the L-series with negative arguments, for which the generalised Bernoulli numbers would then provide us with an exact solution. In this sense we are cheating a bit when writing $\beta(2)$ for $\mathbb{Z}[\mathrm{i}]$, since β is another special function.

However in our situation an approximate value suffices for the computations.

7.4. Radial projection

In addition to computing the diffraction pattern, we can again determine the radial projection of the four sets. As pointed out before, we may need to consider the Minkowski embedding to work with a planar point set.

Since square-freeness does not imply geometric visibility, we still need to remove some more vertices from out input set. However, we can take advantage of the fact that we always have a lattice in $\mathbb{R}^2$ here. In fact, we can adapt the algorithms from Section 4.3; see Remark 4.46 about lattice subsets.

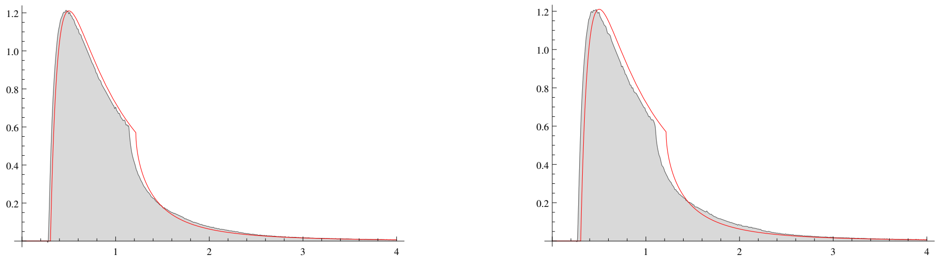

Figure 7.6. Radial projection for the $\mathbb{Z}[\sqrt{2}]$ (left) and $\mathbb{Z}[\mathrm{i}]$ case (right). Reference $\mathbb{Z}^2$ is overlayed in red.

We can see that, while there is a difference of the radial projection compared to our reference, the $\mathbb{Z}^2$ lattice, this difference is fairly small.

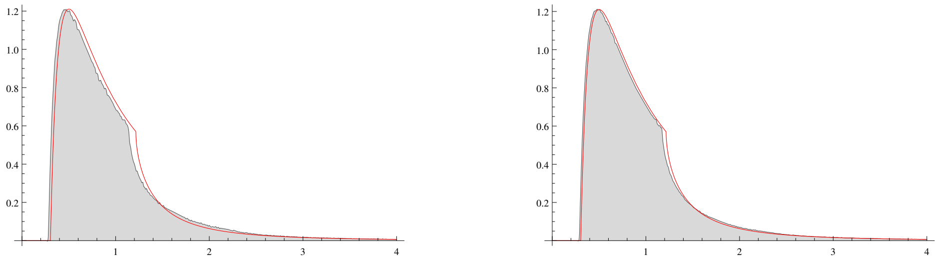

Figure 7.7. Radial projection for $\mathbb{Z}[\omega]$ (left) and $\mathbb{Z}[\tau]$ (right).

We take a brief look at the vertex counts which arise during the computation of the radial projection, namely number of vertices of the initial patch, number of square-free vertices, number of visible square-free vertices and number of data points inside the binning area (here the interval $[0, 4)$).

Table 7.5. Vertex counts (in units of 10^7) during radial projection.

set	patch	square-free	visible	binning
$\mathbb{Z}[\sqrt{2}]$	5.55	3.87	3.19	3.15
$\mathbb{Z}[\mathrm{i}]$	7.85	5.21	4.34	4.28
$\mathbb{Z}[\omega]$	6.8	5.29	3.89	3.84
$\mathbb{Z}[\tau]$	5.85	5.03	3.45	3.41

While the histograms computed for the radial projection only differ in the details, we can see in Table 7.5 that the ratio between square-free and visible square-free changes quite a bit, ranging from 68.5% for $\mathbb{Z}[\tau]$ and 73.5% for $\mathbb{Z}[\omega]$, up to 82.6% and 83.2% for $\mathbb{Z}[\sqrt{2}]$ and $\mathbb{Z}[\mathrm{i}]$, respectively.

Still, it appears that, on the level of the radial projection, lattice subsets in $\mathbb{R}^2$ produced from selecting square-free integers are virtually indistinguishable from the visible lattice points in $\mathbb{Z}^2$. The primitivity condition of the vertex coordinates seems to "dominate" the visibility property for these subsets.

Conclusion 7.2
The main observation in this section is that, for all the cases, the diffraction images differ considerably, but the RPM results do not. So far such a behaviour is the exception, even though we have encountered a case of RPM-invariance in Section 2.8 for the triangular tiling. So, while we know that both methods detect order, each seems sensitive to different aspects of the point set. If one already knows the diffraction, we are confident that RPM can provide some additional insight.

A natural way of proceeding here, would be to consider homemetric point sets, i.e. sets which feature the same diffraction, and distinguish these via RPM. Of course the other direction (same RPM, different diffraction) is also worth to be investigated.

CHAPTER 8

Outlook

We hope that this thesis has provided a first insight into the realm of the RPM and how it could function as an additional indicator of order alongside the classical tools, such as diffraction analysis.

We have focused our attention on planar tilings which admit an easy and exact encoding on a computer system, in particular to facilitate the numerical evaluation. If one continues this investigation of planar tilings, the more complex candidates like the pinwheel or the square triangle [5, Sec. 6.3.1] tiling need to be considered as well.
Most of our examples behaved similar to the $\mathbb{Z}^2$ lattice. But even among the easy cases, we have encountered the LB tiling as a candidate which shows some unusual behaviour. From [24, Sec. 3], we know some properties of the (asymptotically unbounded) window, when the LB tiling is considered as a projection set. We think that a deeper understanding of the influence of the window on the RPM is necessary here to make further progress. In this specific case, it would require some efficient description of a vertex test for a window of fractal type. Also, access to more tilings would help us to further understand to which properties of the point set the RPM is sensitive to. More open questions are the extension of the procedure to higher dimensions, and the dichotomy observed for the second-order spacings.

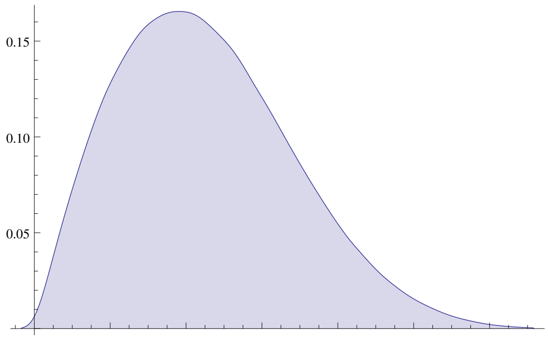

Figure 8.1. Distribution of the norm of the vertices of the LB tiling, when lifting them into internal space. A circular patch with $1.3 \cdot 10^6$ vertices was used here, hence the coding set is finite.

So far, we only looked at a simple randomisation approach. It should be considered to replace the Bernoulli thinning by a procedure taking the radial and angular component of a vertex into account, by e.g. removing more vertices the further away one is from the origin. But then again, also with our simple setup, many results, like the convexity of the gap position for the ω-thn approach, remain unclear.
As pointed out in the introduction, the conception of the RPM is still largely unfinished. In a dynamical system context, it would probably make more sense to establish an RPM for the hull. This would require independence of the limit distribution from the reference point. We have seen that averaging might be one possible solution to this problem.
A promising approach to establish more rigorous analytic descriptions of our limit distribution seems to be the recent work by Athreya et al. [3]. The similar results, with respect to the limit distributions found, suggest that there is a relation between some of our planar tiling systems and the saddle connections on translation surfaces [29] studied in [3]. If such a relation could be established, it would enable us access to the powerful machinery of ergodic theory.

In any case, we hope that our analysis has sparked some interest in the topic, leading to further research in this area.

APPENDIX A

Source code

The entirety of the source code written during this thesis can be be found in my GitHub repository [34]. The programming language is `C++`, where we have tried to avoid all language features, like e.g. inheritance, which might potentially affect performance in a negative way. A small number of external libraries are used, but most of the core code just uses the standard template library. The bulk of the implementation is found in src, while the headers are found in include. A simple Makefile is included to ease compilation of the project.

We now give a brief overview of the functionality implemented in each source code file. Experimental code, which was written but ultimately not used in the thesis, is marked as `WIP`.

- alignment_allocator: Allocator for aligned system memory. Useful when working with `SSE` intrinsics, which only operate on aligned data. (`WIP`)
- arith_visibility: Algorithms used in Chapter 7 to compute arithmetic visibility (square-free, cube-free) and the corresponding diffraction patterns. Also contains code to export the computed patterns to `EPS` and `SVG` files.
- chiral_radial: Algorithms for computing the radial projection of the LB and the chair tiling.
- common: Algorithms and data structures shared across the project.
- corner_cases: Radial projection of the $\mathbb{Z}^2$ and Poisson case.
- cyclotomic_decagonal: Helper code for radial projection of the TT tiling.
- cyclotomic_dodecagonal: Helper code for GS case.
- cyclotomic_octagonal: Helper code for AB case.
- cyclotomic_radial: Main code for the radial projection of all cyclotomic model set cases. Uses the corresponding helper code.
- cyclotomic_random: Randomisation of the cyclotomic model set cases.
- cyclotomic_rhombic_penrose: Helper code for RP case.
- griddual: Tiling construction by dualisation of a grid. Useful for constructing tilings with high rotational symmetry properties. (`WIP`)
- hexagonal: Radial projection of the triangular tiling.
- higher_cyclo: Radial projection of cyclotomic model sets with higher order. (`WIP`)

- histogram: Histogram binning for first- and second-order spacings. Reads from `stdin` and writes binning result to `stdout`.
- level_manager: Generic helper code for the shell construction described in Chapter 3.
- pdf_writer: Utility functions for directly writing diffraction pattern data to a `PDF` file.
- pooled_alloc: Special memory allocator for one-time usage. Used for the brute-force visibility approach in Procedure 4.33.
- random: Randomisation of the $\mathbb{Z}^2$ case.
- threaded_transform: Template code to split data transformations into multiple threads for efficient use of multi-core systems. (`WIP`)
- tuebingen: Radial projection of TT and PR tiling. The TT is constructed via inflation here.
- visibility: Generic code for brute-force visibility computation; see Procedure 4.33.

All `Mathematica` notebooks can be found in mathematica. The bulk of the data visualisation was implemented there. Also most algorithms were first prototyped and tested there, before cleaning them up and translating them to `C++`.

A small utility to feed raw data into `Mathematica`, e.g. for visualisation, is included in mathinterface. It needs to be built against the local `Mathematica` version and can then be used with the MathLink interface. This was done to efficiently import data computed outside `Mathematica`, without resorting to formatting the numerical data into a text-based representation. In particular, this would have meant sacrificing numerical precision when importing floating-point data.

Bibliography

[1] R. Ammann, B. Grünbaum, and G. C. Shephard. "Aperiodic tiles". *Discr. Comput. Geom.* 8.1 (1992), pp. 1–25.

[2] J. S. Athreya. "Gap distributions and homogeneous dynamics". In: *Geometry, Topology, and Dynamics in Negative Curvature*. Ed. by C. S. Aravinda, F. T. Farrell, and J.-F. Lafont. London Mathematical Society Lecture Note Series. Cambridge University Press, 2016, pp. 1–31. arXiv: `1210.0816`.

[3] J. S. Athreya, J. Chaika, and S. Lelievre. "The gap distribution of slopes on the golden L". In: *Recent Trends in Ergodic Theory and Dynamical Systems*. Ed. by S. Bhattacharya, T. Das, A. Ghosh, and R. Shah. Vol. 631. American Mathematical Society, 2015, pp. 58–72. arXiv: `1308.4203`.

[4] J. S. Athreya and Y. Cheung. "A Poincaré section for horocycle flow on the space of lattices". *Int. Math. Res. Notices* 2014.10 (2014), pp. 2643–2690. arXiv: `1206.6597`.

[5] M. Baake and U. Grimm. *Aperiodic Order. Vol. I: A Mathematical Invitation.* Cambridge University Press, 2013.

[6] M. Baake and C. Huck. "Ergodic properties of visible lattice points". *Proc. Steklov Inst. Math* 288.1 (2015), pp. 165–188. arXiv: `1501.01198`.

[7] M. Baake, P. Kramer, M. Schlottmann, and D. Zeidler. "Planar patterns with fivefold symmetry as sections of periodic structures in 4-space". *J. Mod. Phys. B* 4.15-16 (1990), pp. 2217–2268.

[8] M. Baake, P. Kramer, M. Schlottmann, and D. Zeidler. "The triangle pattern – a new quasiperiodic tiling with fivefold symmetry". *Mod. Phys. Lett. B* 4.4 (1990), pp. 249–258.

[9] M. Baake, R. V. Moody, and P. A. B. Pleasants. "Diffraction from visible lattice points and k-th power free integers". *Discrete Math.* 221.1-3 (2000), pp. 3–42. arXiv: `math/9906132`.

[10] F. P. Boca, C. Cobeli, and A. Zaharescu. "Distribution of lattice points visible from the origin". *Commun. Math. Phys.* 213.2 (2000), pp. 433–470.

[11] Z. I. Borevich and I. R. Shafarevich. *Number Theory.* Pure and Applied Mathematics. New York: Academic Press, 1966.

[12] N. G. de Bruijn. "Algebraic theory of Penrose's nonperiodic tilings of the plane. I, II". *Nederl. Akad. Wetensch. Indag. Math.* 43.1 (1981), pp. 39–52, 53–66.

[13] W. Burger and M. J. Burge. *Principles of Digital Image Processing. Core Algorithms.* Undergraduate Topics in Computer Science. London: Springer-Verlag, 2009.

[14] L. Chen, R. V. Moody, and J. Patera. "Non-Crystallographic Root Systems". In: *Quasicrystals and Discrete Geometry.* Vol. 10. Ed. J. Patera. Providence, RI: Amer. Math. Soc., 1998, pp. 135–178.

[15] S. N. Chiu, D. Stoyan, W. S. Kendall, and J. Mecke, eds. *Stochastic Geometry and its Applications.* 3rd. Wiley series in probability and statistics. Chichester: Wiley, 2013.

[16] C. Cobeli and A. Zaharescu. "The Haros–Farey sequence at two hundred years". *Acta Univ. Apulensis. Math. - Inform.* 5 (2003), pp. 1–38.

[17] P. M. Cohn. "Bezout rings and their subrings". *Math. Proc. Cambridge Philos. Soc.* 64.2 (1968), pp. 251–264.

[18] T. H. Cormen, C. E. Leiserson, R. L. Rivest, and C. Stein. *Introduction to Algorithms.* 3rd. Cambridge, Massachusetts: The MIT Press, 2009.

[19] J. M. Cowley. *Diffraction Physics.* 3rd. North-Holland. Amsterdam: Elsevier, 1995.

[20] U. Drepper. *What Every Programmer Should Know About Memory.* 2007. URL: `https://people.freebsd.org/~lstewart/articles/cpumemory.pdf`.

[21] S. R. Finch. *Mathematical constants.* Encyclopedia of Mathematics and its Applications. Cambridge University Press, 2003.

[22] A. Fog. *Software optimization resources.* 2017. URL: `http://www.agner.org/optimize/`.

[23] F. Gähler. "Quasicrystal Structures from the Crystallograhic Viewpoint". PhD thesis no. 8414. ETH Zürich, 1988.

[24] C. Godrèche and F. Lançon. "A simple example of a non-Pisot tiling with five-fold symmetry". *J. Phys. I France* 2.2 (1992), pp. 207–220.

[25] T. Granlund and the GMP development team. *GNU MP: The GNU Multiple Precision Arithmetic Library.* 6.1.1. 2016. URL: `https://gmplib.org/gmp-man-6.1.1.pdf`.

[26] B. Grünbaum and G. C. Shephard. *Tilings and Patterns.* New York: Freeman, 1987.

[27] G. H. Hardy and E. M. Wright. *An introduction to the theory of numbers.* Ed. by D. R. Heath-Brown. 6th. Oxford University Press, 2008.

[28] A. Hof. "On diffraction by aperiodic structures". *Commun. Math. Phys.* 169.1 (1995), pp. 25–43.

[29] P. Hubert and T. A. Schmidt. "An Introduction to Veech Surfaces". In: *Handbook of Dynamical Systems.* Vol. 1. B. Amsterdam: Elsevier, 2006, pp. 501–526.

[30] C. Huck and M. Spiess. "Solution of a uniqueness problem in the discrete tomography of algebraic Delone sets". *J. reine angew. Math. (Crelle)* 677 (2013), pp. 199–224. arXiv: `1101.4149`.

[31] *IEEE Standard for Floating-Point Arithmetic.* Institute of Electrical and Electronics Engineers. New York, 2008.

[32] K. Iwasawa. *Lectures on p-Adic L-Functions.* Annals of Mathematics Studies. Princeton University Press, 1972.

[33] T. Jakobi. *Radial projection statistics: Online appendix (of this thesis).* 2017. URL: `https://www.math.uni-bielefeld.de/~tjakobi/thesis/appendix.html`.

[34] T. Jakobi. *Radial projection statistics: Thesis source code.* 2017. URL: `https://github.com/tobiasjakobi/radialprojection`.

[35] D. Kerr and H. Li. “Independence in topological and C*-dynamics”. *Math. Annal.* 338.4 (2007), pp. 869–926. arXiv: `math/0603585`.

[36] F. Lançon and L. Billard. “Two-dimensional system with a quasi-crystalline ground state”. *J. Phys. France* 49.2 (1988), pp. 249–256.

[37] E. Landau and J. Franel. “Les suites de Farey et le problème des nombres premiers”. *Gött. Nachr.* (1924), pp. 198–201.

[38] J. Marklof and A. Strömbergsson. “Free path lengths in quasicrystals”. *Commun. Math. Phys.* 330.2 (2014), pp. 723–755. arXiv: `1304.2044`.

[39] J. Marklof and A. Strömbergsson. “The distribution of free path lengths in the periodic Lorentz gas and related lattice point problems”. *Ann. of Math. (2)* 172.3 (2010), pp. 1949–2033.

[40] J. Marklof and A. Strömbergsson. “Visibility and directions in quasicrystals”. *Int. Math. Res. Not.* 2015.15 (2015), p. 6588. arXiv: `1404.1564`.

[41] D. Meagher. “Geometric modeling using Octree encoding”. *Computer Graphics and Image Processing* 19.2 (1982), pp. 129–147.

[42] K. B. Oldham, J. Myland, and J. Spanier. *An Atlas of Functions.* 2nd. New York: Springer-Verlag, 2009.

[43] P. A. B. Pleasants. “Lines and Planes in 2- and 3-Dimensional Quasicrystals”. In: *Coverings of Discrete Quasiperiodic Sets.* Ed. by P. Kramer and Z. Papadopolos. Vol. 180. Springer Tracts Modern Phys. Springer Berlin, 2003, pp. 185–225.

[44] P. A. B. Pleasants and C. Huck. “Entropy and diffraction of the k-free points in n-dimensional lattices”. *Discrete Comput. Geom.* 50.1 (2013), pp. 39–68. arXiv: `1112.1629`.

[45] W. H. Press, S. A. Teukolsky, W. T. Vetterling, and B. P. Flannery. *Numerical Recipes in C: The Art of Scientific Computing.* 2nd. New York: Cambridge University Press, 1992.

[46] C. Radin. “The pinwheel tilings of the plane”. *Ann. of Math. (2)* 139.3 (1994), pp. 661–702.

[47] M. Schlottmann. “Cut-and-project sets in locally compact Abelian groups”. In: *Quasicrystals and Discrete Geometry.* Vol. 10. Ed. J. Patera. Providence, RI: Amer. Math. Soc., 1998, pp. 247–264.

[48] B. Sing. *Visible Ammann–Beenker Points.* Presentation at the Mathematical Physics Seminar (24.10.08.) University of Bristol, 2008. URL: `http://www.bb-math.com/bernd/pub.html`.

[49] L. C. Washington. *Introduction to Cyclotomic Fields.* 2nd. New York: Springer, 1997.

[50] D. B. Zagier. *Zetafunktionen und quadratische Körper. Eine Einführung in die höhere Zahlentheorie.* Hochschultext. Springer Berlin, 1981.

List of Figures

Index